SAPIENZA
UNIVERSITÀ DI ROMA

Dept. of Biochemical Sciences 'A. Rossi-Fanelli'

Ph.D. in Biophysics

STRUCTURAL DYNAMICS OF NEUROGLOBIN: PHOTOREDUCTION AND PHOTODISSOCIATION INTERMEDIATES

Ph.D. student
Chiara Ardiccioni

Supervisor
Prof. Beatrice Vallone

Coordinator
Prof. Alfredo Colosimo

Rome, December 2010

Contents

1 Introduction **5**

1.1 Neuroglobin and the vertebrates globin family 5

1.1.1 Gene evolution and structure 7

1.2 Functional parameters 10

1.2.1 Spectroscopic and kinetic characterization 10

1.2.2 Oxygen binding 13

1.2.3 Catalytic activity 16

1.2.4 Involvement of Ngb in a signal transduction pathway 20

1.3 Structural features 23

1.3.1 Crystallographic study of Ngb cavities . 31

1.3.2 Comparison of Ngb cavities with Mb and Cygb 33

1.3.3 Cavities and photolytic intermediates in Myoglobin and Neuroglobin 35

1.4 *In vivo* characterisation: localization and hypoxic-induced expression 38
1.5 Physiological role: is Ngb a neuroprotectant? . . 40

2 Materials and methods 45
2.1 Gene synthesis and cloning 45
2.2 Neuroglobin expression and purification 46
2.3 Crystallization and crystal handling 48
2.3.1 Neuroglobin 48
2.3.2 Horse skeletal muscle Myoglobin 48
2.3.3 Sperm whale Myoglobin 49
2.3.4 EryK P450 49
2.4 Experimental techniques 51
2.4.1 UV-Vis absorption microspectrophotometry 51
2.4.1.1 Off-line microspectrophotometer at low temperature 51
2.4.1.2 On-line microspectrophotometer 55
2.4.2 Crystal structure determination by X-Ray Diffraction (XRD) 57
2.4.2.1 XRD at low temperature 58
2.4.2.2 XRD at room temperature . . . 59
2.4.3 X-ray Absorption Spectroscopy (XAS) . . 61
2.4.3.1 XAS aims 61
2.4.3.2 XAS basics 61
2.4.3.3 XANES measurements on NgbCO in solution 67
2.4.3.4 Polarized XANES measurements on NgbCO crystals 68

3 Results and discussion **73**
3.1 Heme environment determination of NgbCO: XANES spectra 73
3.2 Redox state determination: UV-Vis microspectrophotometry (on-line) on crystal 77
3.3 Characterization of Ngb matrix 82
3.3.1 Characterization of NgbCO photolytic intermediates 83
3.3.1.1 UV-Vis microspectrophotometry on NgbCO crystal (off-line) 84
3.3.1.2 Structure of photolytic intermediate Ngb*CO at low temperature 87
3.3.1.3 XANES spectra on NgbCO in solution 90
3.3.2 Structure of Ngb at room temperature under different gaseous pressures 93
3.3.2.1 XRD at room temperature: different pressures of Xe 94
3.3.2.2 XRD at room temperature: different pressures of O_2 99
3.3.2.3 XRD at room temperature: different pressures of CO 102

4 Conclusions and perspectives **105**
4.1 General aims of the work 105
4.2 X-ray Absorption Spectroscopy and the Ngb heme environment 107
4.3 Redox state of hemeprotein crystals 107

4.4 The Ngb internal 'tunnel': partial conservation and potential role 108

5 Aknowledgements **113**

Bibliography **117**

Appendix **139**

Chapter 1

Introduction

1.1 Neuroglobin and the vertebrates globin family

Hemoglobins (Hbs) are small globular proteins able to bind gaseous ligands by means of a Fe-containing porphyrin ring. These hemeproteins are endowed with the 'globin fold' consisting of eight α-helices (A-H), which are arranged in the so called 3/3 α-helical sandwich typical of sperm whale Myoglobin. Some variants of this fold have been described, *e.g.* the 2-on-2 sandwich characterizing the 'truncated globins'. Independently to the fold adopted, all globins share an invariant histidine at position F8 providing the proximal ligand to the heme iron [1]. Hbs are widely present in all the three domains of Life (*Bacteria*,

Archea and *Eukaryota* [1, 2, 3]).
Evolutionary considerations on the environment experienced in the early stages of the life on earth have suggested that the O_2 transport function of vertebrate globins was a relatively recent adaptation, acquired by Hbs when aerobic metabolism became predominant. According to such considerations, the variety of globins identified in bacteria, displaying a wide range of catalytic activities, makes it clear that the early globin function must have been enzymatic and O_2-sensing [1]. Although Myoglobin (Mb) and Haemoglobin (Hb) are the most extensively studied vertebrate globins, several other globins have been discovered during the last decade. Therefore the vertebrates globin superfamily is so far represented by six members: Hb, Mb, Neuroglobin (Ngb), Cytoglobin (Cygb), Globin E (GbE) and Globin X (GbX) [4, 5]. Among these, both Ngb and Cygb are expressed in human, where their precise function and mechanism of action is still elusive.
In the case of Ngb, its localization in neurons [6] elicited particular interest, and several hypothesis were proposed for its role in the brain [7]. Among others, very interesting experiments *in vitro* and *in vivo* published by Greenberg and colleagues showed that Ngb may play a role in neuroprotection, since they observed that recovery from stroke in experimental animals was ameliorated by Ngb over-expression [8, 9].
It seems unlikely, although not excluded by some authors, that Ngb is an O_2 reservoir or transporter, because of its low average concentration in neurons (~ 1 μM), and of its high autoxidation rate [10]. Some of the alternative functions that were proposed group into the following categories: (i) signaling of hypoxia; (ii)

radical scavenging (constitutive or under hypoxic conditions); (iii) apoptosis regulation under hypoxic conditions [11, 12]; (iv) a component of a signal transduction pathway [13]; (v) possible interaction with the cellular prion protein (PrPc) [14]. However, it is not possible to exclude that interaction with O_2 represents a relevant feature of the physiological Ngb role.
Phylogenetic analysis and biochemical studies support the idea that Ngb has retained some enzymatic functions endowed by ancestral globins; an alternative (or complementary) function could be the participation in a novel signalling function to trigger protective responses to hypoxia, mainly regulating the apoptotic processes [15].
Since the discovery of Ngb by Burmester and colleagues [6], its three-dimensional structure has been determined for human (deoxy) and murine (deoxy and carbonmonoxy) Ngbs. Its kinetics and reactivity towards O_2, CO and NO has been analyzed, and extensive spectroscopic investigations have been carried out. Moreover both *in vivo* and *in vitro* studies were performed to shed light on Ngb mechanism of action in the nervous tissue.

1.1.1 Gene evolution and structure

The ancestor of globins is thought to be present in organisms as far as back the Last Universal Common Ancestor (LUCA, Lane, 2002) since members of the globin family are spread among virtually all kingdoms of Life [2].
The discovery of 'protoglobins' in two *Archea* [16] suggests that this ancestral Hbs arose before oxygenic photosynthesis. Since enzymatic functions are observed in several non-vertebrate sys-

tems, where globins catalyze reactions towards O_2, NO and H_2S [17, 18], a likely function for the ancestor globin is thought to be enzymatic. A likely scenario envisages that an ancestral globin, with an original redox function, gained O_2 binding and scavenging properties. Mb and Hb would be evolved in dioxygen carriers from this ancestor. In fact, although delivery and facilitated diffusion of O_2 is the commonly acknowledged function for Hb and Mb, enzymatic properties of these (and others) Hbs have been reported and generally accepted [19, 20].
During the last decade Ngb, Cygb, globin GbE (eye-specific) and GbX (recently discovered in fish and amphibians) have been added to the vertebrate globin family, based on the results of database searches for globin-like sequences [6, 21, 22].
These novel globins, which are all expressed at low concentration, differ in sequence, tissue distribution and likely in function. Phylogenetic analysis of vertebrate globins indicates that they can be associated with two distinct branches of metazoa, which share a starting point within the taxon of archaic *Bilateria* [5]. The first branch includes Ngb and GbX and the second branch includes two clades, respectively the protostomian globins clade and the clade of vertebrates globins, which is formed by GbE, Cygb, Mb and Hb, as shown in Fig. 1.1.1.
Taking into account the early divergence of these two globin branches, some authors suggest that the last common bilaterian ancestor should possess at least two distinct globin genes: one is the predecessor of Ngb and GbX, whereas the other gives rise to the other metazoan globins [5].
Within this second group, one lineage leads to globins specialized in intracellular functions: Cygb and Mb. Haemoglobins

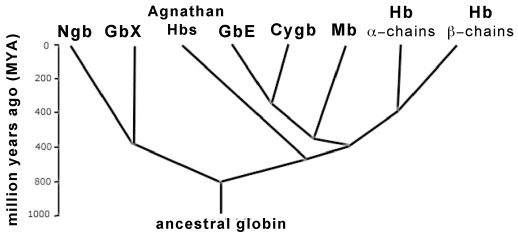

Fig. 1.1.1: **a simplified phylogenetic tree of vertebrate globins.**

instead diverged from intracellular globins and obtained their function in circulatory system. This function gain was probably correlated with an increase in body size and the evolution of an efficient circulatory system [22].

From evidences based on the number and the position of introns, the Ngb gene structure differs from that of Mb and Hb: the last two are formed by three exons and two introns, whereas Ngbs genes show four exons and three introns. In fact, Ngb and GbX are the unique vertebrate globins showing an intron in helix E, evidence that reinforces their assignment to a gene family separate from that including Mb, Hb and Cygb [5].

Reliable sequences of Ngb from 11 mammals, 1 bird and 4 teleost fish species have been determined [23]. In all species apart from the trout, Ngb seems to be present as a single-copy gene. Structural analysis showed that Ngb sequences are consistent with the globin fold template, given the conservation of amino acids involved in iron coordination (proximal and distal histidines), heme accommodation and ligand interactions (*i.e.*,

PheB10, PheCD1, TyrCD3, ValE11, LeuF4, ValFG1, ValFG3 and PheG5; [24, 25]). Comparison of Ngb with Hb and Mb shows less than 25% of conserved residues; on the other hand $\sim$ 0.4 x 10^{-9} amino acid changes/year are observed within mammalian sequences of Ngb, a frequency which corresponds to one third of that observed for Hb [5]. In fact 46.4% of all residues (corresponding to 70 positions) are conserved within Ngbs from vertebrates, suggesting that tight functional requirements induce a strong purifying selection. Insertions are observed at the C and N termini of Ngb sequences and, limited to one amino acid, at the flexible CD corner. In Ngbs from different organisms, up to three cysteines are observed but only one, in topological position D5, is conserved in all sequences.
Finally, the fact that Ngb seems to be allowed little evolutionary divergence, and very similar ligand binding parameters observed in man, mouse and zebrafish Ngb, suggest that its function has tight requirements in terms of protein sequence and structure.

1.2 Functional parameters

1.2.1 Spectroscopic and kinetic characterization

Since the discovery of Ngb, its spectroscopic properties have been investigated with different techniques; optical and resonance Raman spectra clearly show that Ngb is a hexacoordinated globin, in both the ferric and ferrous states [10, 21, 26]; crystallographic models demonstrate that, in absence of external ligands, the distal histidine (HisE7) occupies the sixth coordi-

nation position of the heme iron [24, 25]. This is an uncommon feature in vertebrates: so far, Ngb and Cygb are the only hexacoordinated globins among vertebrates. On the contrary, different kind of eukaryotic taxa display some examples of hexacoordination, since this feature has been reported for some Hbs of invertebrates, cyanobacteria and other plant globins [27, 28, 29].
Endogenous hexacoordination allows the binding of an external ligand only upon rupture of the bond with distal His(E7), which implies a competition for the heme sixth coordination position between this histidine and the exogenous ligand, that affects the overall affinity for O_2, CO and NO. Therefore, the kinetics and thermodynamics of binding to Ngb can be depicted by a minimum two-step mechanism (Eq. 1.1):

$$Ngb_H \underset{k_H}{\overset{k_{-H}}{\rightleftharpoons}} Ngb_P + L \underset{k_{-L}}{\overset{k_L}{\rightleftharpoons}} Ngb{-}L \tag{1.1}$$

where the pentacoordinate species (NgbP) is the species competent for binding a ligand (L).
Upon mixing ferrous Ngb with several ligands (O_2, CO, NO and methyl isocyanide), the formation of the adduct was found to be a slow process ($t_{1/2} \sim$ 1s) and the relative rate constant(s) was ligand independent [21, 10, 26, 30], showing that the dissociation of distal histidine (k_{-H}) is the rate-limiting step for the adduct formation.
Endogenous hexacoordination also implies that the pentacoordinated state (NgbP) is briefly populated, due to the competition between distal histidine and the ligand for the sixth coordination position. Extensive flash photolysis experiments, instantly populating NgbP, allowed to measure the rate constant for ligand

binding in competition with His(E7). NO, O_2 and especially CO show high values of association rate (k_L), which together with the low dissociation rate (k_{-L}) account for its affinity, that is higher than that of Mb and isolated Hb-chains [10, 31].
The same experiments also show a rate constant for histidine rebinding of $\sim 2000\ s^{-1}$ [21, 10, 30, 32, 33]: such a value implies that the equilibrium constant for the hexa-to-pentacoordinated states (k_{-H}/k_H) is around 10^{-3} (in agreement with rapid mixing experiments); in other words, the hexa-to-penta equilibrium favours the hexacoordinated state by a ratio of $\sim$ 1000:1. Therefore, in spite of the significant k_L, the competition with the His(E7) determines in Ngb an oxygen P_{50} lower than that of Mb, although in the same order of magnitude (see Par. 1.2.2 for a more detailed discussion on Ngb oxygen P_{50}).
Rapid mixing experiments of ferrous Ngb with CO and methyl isocyanyde indicate that the kinetics of the rupture of the distal His(E7) is heterogeneous [32]. These experiments showed the presence of two phases, with relative amplitude of ($\sim$ 7:3). This heterogeneity has been explained invoking a pronounced structural heterogeneity of distal heme pocket, shown by IR and NMR spectroscopy and also by complementary mutational data [26, 34]. In this respect, it is relevant to recall that solid evidence exists [35, 25, 36] for heme orientational disorder in metNgb (see Par. 1.3). It is not clear, however, if the heme orientational disorder is an artefact of heterologous Ngb synthesis or is an intrinsic property of the native protein.
Geminate rebinding is a common feature of globins, and consists in the rapid rebinding of a heme-photodissociated molecule from internal docking sites to the iron. Rebinding of photolyzed ligands to Ngb has been analyzed using UV-Vis and IR spectroscopy. These analyses point out that the geminate rebinding

is an extremely fast process, suggesting a very small enthalpy barrier at the heme Fe [34].
This fact represents an interesting feature, which partially sheds light on the role of the internal matrix in regulating the reactivity of Ngb towards several gaseous ligands.

1.2.2 Oxygen binding

The canonical role of globins in vertebrates is the delivery of O_2 for aerobic metabolism, from Hb to Mb and finally to cytochrome *c* oxidase. The transfer is achieved by proper modulation of the affinity for this ligand. The discovery that Ngb binds O_2 reversibly led initially to the assumption that also this novel protein was primarily involved in O_2 transport in neurons.
Several groups have measured the O_2 affinity, reporting the oxygen half saturation pressure (oxygen P_{50}); nevertheless, the use of different techniques, the wide range of conditions explored and the concomitant usage of both murine and human Ngb (respectively mNgb and hNgb), account for the presence in the literature of contrasting values of the oxygen P_{50}. Moreover, determination of the O_2 affinity of Ngb is particularly difficult due to its tendency to autooxidize with a half time, in air, that varies from $\sim$ 20 to $\sim$ 3 minutes, depending on pH values [21, 10, 37]. Burmester and colleagues reported an oxygen P_{50} of about 1.9 - 2.3 torr for mouse Ngb at 20 °C [6]. Nevertheless, these measurements were carried out at equilibrium on an *Escherichia coli* (*E. coli*) extract expressing mNgb. Under these conditions, Ngb is expected to be kept in the reduced state by a bacterial reductase [38], whose activity could interfere with the affinity mea-

surements. Fago and co-workers referred a different value (10 torr) for the oxygen P_{50} in mNgb, also demonstrating that this parameter is pH dependent in both the human and murine forms (a Bohr effect; [37]). Mutational studies demonstrate that this effect is mainly due to the protonation of His(E7) and Lys(E10) [33].
The determination of a univocal value of oxygen P_{50} for hNgb has been also challenged by the dependence on the temperature. For hNgb, oxygen P_{50} was estimated from kinetics [10] to be 2.0 torr at 37 °C, somewhat similar to that reported for Mb at 20 °C (1.0 torr). Further measurements, carried out by means of O_2 equilibria at physiological pH under conditions that would minimize autooxidation, indicated that at 25 °C $P_{50} = 5.0$ torr, while at 37 °C $P_{50} = 7.5$ torr [37], the last being almost 4 times greater than that observed previously at the same temperature. The relatively low O_2 affinity under physiological conditions, together with the low average concentration of Ngb in the Central Nervous System (CNS) (~ 1 μM) and its tendency to autooxidation, may suggest a peculiar primary role different from O_2 storage and/or facilitated diffusion. Since in Ngb the overall affinity constant for O_2 (or other exogenous ligands) results from a competition with His(E7) rebinding, as illustrated in Eq. 1.1, ligand affinity is not modulated exclusively by the *on* and *off* rate constants to the pentacoordinate state as in the case of Mb. This was clearly shown by mutational studies on Ngb [10, 37, 30]. Upon changing the distal His(E7) to Leu, Val or Gln, the overall affinity for O_2 of mNgb and hNgb increased with respect to the wild type (by a factor that ranges from 3 to 100 in different mutants), in spite of the variations of k_L and of k_{-L} that would

imply a decrease in affinity [10, 37]. The absence of competition for the endogenous His(E7) ligand is most likely the cause of the increase in the apparent affinity for O_2. Another remarkable effect of the mutations His(E7)Gln and His(E7)Leu/Lys(E10)Leu is the drastic reduction of the autooxidation rate in air [37], indicating that His(E7) enhances the reactivity of oxygenated Ngb. For human Ngb, Hamdane *et al.* [30] reported a ten-times decrease in O_2 affinity (P_{50} from 0.9 to 8.4 torr) upon reduction of an intramolecular disulfide bridge between Cys(CD7) and Cys(D5); moreover, a consistent effect of this disulfide bond was observed also by kinetics [39]. The general physiological relevance of the disulphide bridge is questionable and still under debate. Some authors consider this evidence as the proof of a mechanism for the 'fine regulation' of oxygen affinity: under low oxygen supply the disulfide bridge in Ngb would be in the reduced state; the ensuing lower O_2 affinity would result in a net release of O_2 to the cell. Under higher oxygen concentrations the CD7-D5 disulfide will form, increasing the Ngb affinity for O_2 and reloading the protein [30, 37, 40].
Moreover, recent Molecular Dynamics (MD) simulations suggested a mechanical explanation for such a behaviour of cysteine-oxidated hNgb: the disulfide bridge would force the CD-D region of the hexacoordinated state in a conformation similar to that of NgbP, promoting therefore the achievement of the latter species; once pentacoordinate, human Ngb would be ready to bind the incoming ligand with higher affinity. Obviously, such a lowering in enthalpy barriers between the two states is lost upon reduction of the two cysteines [40].
Nevertheless, this scenario is prone to some objections. First of

all, within living cells oxidized thiols are intrinsically unstable [41]. Moreover, the relevance of Cys(CD7)-Cys(D5) disulphide bridge may be limited to *H. sapiens* species, since in other vertebrates Cys(CD7) is not conserved.

1.2.3 Catalytic activity

The reactions of Hbs with NO are among the most relevant globin functions. Several globins, in spite of their phylogenetic distance, share reactivity toward NO, indicating that these reactions might reflect an ancestral globin function. In vertebrates, reactivity of Mb toward NO has been well characterized as a protective mechanism for the respiration chain. The Mb ability to both scavenge NO under physiological conditions and to switch to NO generation under hypoxia, makes Mb a kind of O_2 sensor which slacks off the terminal oxidase activity when, due to limited oxygen concentration, the cell cannot sustain an elevate metabolism [1].
Ngb catalyzes several *in vitro* redox processes, mainly but not only directed towards NO and related radicals. These reactions imply that ferrous Ngb can react with a radical substrate, yielding a non-toxic product and ferric Ngb (metNgb). Thus, assuming that Ngb is involved in redox reactions in the cell, a suitable intracellular reductase is expected to exist to allow re-cycling from the ferric to the ferrous state, as required by a catalytic cycle. So far, identification of a specific metNgb reductase is missing [11]. Anyway, preliminary experiments have recently shown that liver and brain cells contain such an enzyme, which could be orthologous to a NAD(P)H dependent Ngb reductase

detected in *E. coli* extracts [38].
In order to shed light on the *in vivo* redox functions of Ngb, we may recall that characterization of the reduction kinetics in hexacoordinated Hbs (hxHbs), including human Ngb [42], showed that in these proteins electron transfer is much faster than in pentacoordinated hemeproteins. This behaviour has been explained on the basis of the more favourable reorganization energy term involved in the reduction of the hexacoordinated hemeproteins, supporting the hypothesis that hxHbs may be tuned for redox cycling rather than binding. As an example, it was shown that oxygenated Ngb reacts very rapidly with NO (complete in the dead time of the stopped-flow, ~ 3 ms) to yield a peroxynitrite intermediate that decays to nitrate and metNgb [43] with first order rate constants of 90 s^{-1}(at 5 °C) and 300 s^{-1}(at 20 °C). This behaviour seems compatible with NO scavenging under partially hypoxic conditions in the nervous system where, at the same time, NO synthesis would be enhanced by induced expression of Nitrous Oxide Systems (NOS) [44]. On the contrary, since unligated ferrous Ngb does not show any direct NO reductase activity, binding of NO to Ngb(FeII) would yield essentially a dead-end adduct, given that its thermal dissociation is very slow ($t_{1/2} > 30$ min; [39]).
It is possible to hypothesize another role for the Ngb(FeII)-NO adduct, since this species reacts rapidly with peroxynitrite *in vitro* (second-order rate constant $\sim 1.3 \times 10^5$ $M^{-1}s^{-1}$, almost 100 times faster than Hb) to yield NO and metNgb [45].
In vivo, Ngb(FeII) may sequester NO by forming Ngb(FeII)-NO and consequently act as a scavenger towards peroxynitrite [45]. Such a scenario is compatible with the behaviour of NO within

hypoxic cells, where it increases from nM to μM range. At such concentration, NO easily reacts with superoxide to form harmful peroxynitrite [46]. Peroxynitrite is not only toxic by itself, but *in vivo* it rapidly reacts with mM CO_2 (3×10^4 $M^{-1}s^{-1}$ at 24 °C [47]), generating even stronger nitrating agents than peroxynitrite. Therefore the reactions of both oxy-Ngb with NO and Ngb(FeII)-NO with $ONOO^-$, counteract the generation of NO radicals and may provide an explanation of the neuroprotective effect of Ngb [48]. In fact some papers show that *in vivo* Ngb overexpression protects the cell from oxidative stress, especially if oxidative stress has been induced by NO and peroxynitrite donors [49]. It has been demonstrated that, under anaerobic conditions, Ngb(FeII) is able to reduce NO_2^- to NO, by formation of Ngb(FeIII) and NO (Eq. 1.2); moreover, the latter binds the remaining Ngb(FeII) forming the Ngb(FeII)-NO adduct with low yield (< 20 %, Eq. 1.3). The reaction follows this scheme [12]:

$$Ngb(FeII) + NO_2^- + H^+ \leftrightarrows [Ngb(FeIII)\text{-}NO] + OH^- \leftrightarrows Ngb(FeIII) + NO + OH^- \quad (1.2)$$

$$Ngb(FeII) + NO \leftrightarrows Ngb(FeII)\text{-}NO \quad (1.3)$$

The overall process terminates slowly given the rebinding of NO to available ferrous heme (Eq. 1.3) that causes a slow decay of the nytrosil complex ($t_{1/2}$ = 1500 s^{-1}) a rate in the same order of magnitude than in Mb. Interestingly, spectroscopic analysis demonstrates [Ngb(FeIII)-NO] being the same short-living intermediate that characterizes the reaction of Ngb(FeII)-NO with peroxinitrite; during the reduction of nitrite, this intermediate is slowly populated, accounting for a second-order rate constant

of 5.1 x $M^{-1}s^{-1}$.
In Hb, a role for the β-chain C^{93} as reactive centre for NO has been documented: the evidence of its *S*-nitrosylation induced some authors to suggest a role for Hb as NO carrier and peripheral deliver [1]. Moreover, it has been shown that Mb-nitrite reductase activity in the heart allows to regulate, by soft NO-mediated inhibition, the muscle cells metabolism under hypoxic conditions. It is important to note that very little NO (n-molar levels) is needed to activate soluble guanylate cyclase or to inhibit cytochrome *c* oxidase, the two main physiological targets of the biological activity of NO in mammals.
In analogy to Mb, it is possible to speculate that Ngb would regulate cellular activities by means of similar mechanisms, involving controlled NO release. Also in Ngb nitrite reduction leads to the formation of *S*-nitrosylated species [12]. Taking into account the lower intracellular amounts of Ngb with respect to Mb, the relevance of nitrosylation and nitrite reduction for Ngb has yet to be confirmed by means of *in vivo* studies.
It has to be reminded that other enzymatic functions may, in theory, represent a cellular defence toward radical stress, such as O_2 reductase, superoxide dismutase, catalase and peroxidase. Ngb does not display any of these activities [38]. Ngb can reduce cytochrome *c* (Cyt-c) *in vitro* [15]. Cyt-c is a redox protein essential for oxidative phosphorylation, located in the internal mitochondrial membrane space. Moreover, Cyt-c is also involved in apoptosis, since its release into the cytosol is a step of the pro-apoptotic cascade, leading to the formation of the 'Apoptosome', an oligomeric ATP-dependent complex also formed by Apaf-1 and procapase-9, that regulates caspase (casp-9, casp-3)

activation. This complex is one of the most relevant check-point during the pro-apoptotic cascade, hence it is fine-regulated by the redox state of Cyt-c: only the oxidized form is competent for the formation of an active complex.
MetNgb binds ferric Cyt-c with a K_D in the order of 100 μM, strongly affected by salt concentration. Nevertheless, the reaction catalyzed by ferrous Ngb proceeds with a second-order rate constant of 2 x 10^7 $M^{-1}s^{-1}$, a value close to the fastest known inter-protein redox reaction rate constant, for example the one between Cyt-c and cytochrome *c* oxidase [50]. This reaction may represent a physiological step in the regulation of apoptosis, useful to avoid unnecessary initiation of apoptotic processes [15].

1.2.4 Involvement of Ngb in a signal transduction pathway

It is possible that Ngb regulates the signal transduction pathway mediated by Heterotrimeric G proteins (G proteins). These proteins consist of a regulatory subunit (the α-subunit, G_α) and a βγ-dimer ($G_{\beta\gamma}$; [51, 52]). When a molecule of GDP is bound to the regulatory G_α subunit, it is associated to $G_{\beta\gamma}$. The trimeric state corresponds to the inactive form of G protein. The G_α subunit easily releases GDP and binds GTP, leading to the dissociation of the trimer and the consequent activation of signal transduction. In fact the GTP-bound G_α and $G_{\beta\gamma}$ regulate the activity of different systems, such as adenyl cyclase, phospholipase C_β, and ion channels. Signal transduction is turned off by the intrinsic GTPase activity of the G_α protein, which hy-

drolyzes GTP to GDP and a phosphate, inducing the reassociation of GDP-bound G_α with $G_{\beta\gamma}$.
Ligand or signal-activated G protein-coupled receptors (GPCRs) induce GDP release from a G_α-subunit. Moreover the *on/off* G protein state can be regulated by three groups of protein modulators: guanine nucleotide exchange factors (GEFs), which stimulate GDP dissociation and subsequent GTP binding (GPCRs fall in this cathegory); guanine nucleotide dissociation inhibitors (GDIs), which inhibit GDP dissociation; and GTPase-activating proteins (GAPs), which enhance GTP hydrolysis [51, 52].
Wakasugi and co-workers [13] proposed that Ngb is a component of a signal transduction pathway, based on the observation that metNgb binds to the α-component of the $G_{\beta\gamma}$ protein, acting as a guanine dissociation inhibitor (GDI). More recently they reported evidence for a complex between metNgb and G_α, and identified the protein-protein interface of the putative complex [53]. Based on this information, a scheme relating the redox-ligation state of Ngb and the control of signal transduction was proposed (see Fig. 1.2.1). It was shown that metNgb is endowed with GDI function, whereas reduced CO bound Ngb is not, suggesting that Ngb might play a role in signal transduction depending on its ligation and redox state. In fact, by means of Surface Plasmon Resonance (SPR) analysis, a relevant affinity of metNgb for G_α was measured, with a K_D of 6 x 10^2 nM, while the K_D observed with the ferrous-CO form falls into the mM range; subsequent GST pull-down experiments have confirmed the capability of metNgb to compete with $G_{\beta\gamma}$ for interaction with α-subunit [53].
Based on crosslinking and mass spectrometry experiments [53],

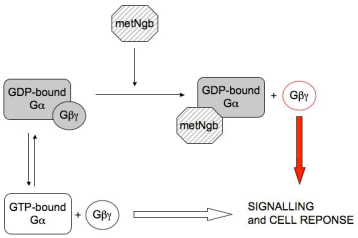

Fig. 1.2.1: **schematic representation of the GDI function of metNgb (modified from** [13]).
Upon binding of met Ngb to the GDP-bound G_{α}- subunit, $G_{\beta\gamma}$ is kept released in an active form, with beneficial cellular effects.

Wakasugi and colleagues concluded that the CD-D region is crucial for the binding of Ngb to G_{α}. They also suggested that the conformational motions of Ngb CD-D region, due to the ligation state, trigger the binding of Ngb to G_{α}. The same experiments shows that the Ngb could bind G_{α} near to the GDP/GTP binding site, providing a structural explanation to the metNgb effect as inhibitor.
Finally, recent *in vivo* investigations suggest that the GDI activity of human Ngb is correlated with its neuroprotective activity. More in detail, these results show that residues responsible for the GDI activity are also crucial for neuroprotection. Because all these residues are charged and exposed to the solvent, these

results suggest that specific protein–protein interactions of Ngb are indispensable for its neuroprotective function [54].

1.3 Structural features

The structures of human Ngb in the met (Fe^{3+}) state, and of mouse Ngb in the met (Fe^{3+}) and CO (Fe^{2+}) bound states have been determined by crystallography [24, 25, 55]. In spite of low sequence homology (less than 25%, [24]), Ngb displays the canonical 3/3 α-helical fold, thus strictly resembling Mb with an average rmsd for C_α atoms of 2.0 and 1.85 Å for met and NgbCO, respectively (Fig. 1.3.1 a). Structural superposition with hexacoordinated rice nonsymbiotic hemoglobin (nsHb, pdb code 1D8U) yielded a comparable result (average rmsd = 2.24 Å) upon exclusion of the short N-terminal extension of nsHb (Fig. 1.3.1 b). The Ngb 3D structure differs from tipical globin for four remarkable peculiarities: (i) the ferric and ferrous heme iron are both hexacoordinate, with the distal His(E7)64 and the proximal His(F8)96 directly bound to the metal ion, (ii) the heme display a significant rotational disorder (iii) the binding of CO to ferrous Ngb is associated to a large conformational change involving a sliding motion of the heme and a moderate shift in the position of helix F and loops CD and EF, (iv) the presence of a huge internal cavity (~ 290 Å^3). Among the vertebrates Hbs, Cygb shares with Ngb both the hexacoordination and the presence of a large internal cavity.
As predicted by spectroscopy, metNgb, in the absence of an exogenous ligand, is hexacoordinated with His96(F8) bound to the

iron on the proximal heme side and His64(E7) on the distal one. In order to bind the iron, the position of the distal His64(E7) in mNgb is closer to the heme by 2.38 Å with respect to sperm whale Mb, and the whole helix E is somewhat repositioned, with a rotation around Leu70(E13) leading to a displacement of the N-term and C-term of the helix of 3.79 and 2.92 Å, respectively. Also in hNgb the position of helix E is shifted of about 3 Å towards the heme. Inspection of metNgb and comparison with the structure of nsHb suggests that the region joining helices C and D (CD turn) may play a role in the structural rearrangement that follows exogenous ligand binding, due to its high mobility and the position it occupies in the globin fold, where it acts like a hinge to allow helix E displacement (Fig. 1.3.1). Significant heme rotational isomerism was observed [24, 25] in both human (hNgb) and murine (mNgb) metNgb structures, with a ratio of 7:3 in mNgb (Fig. 1.3.2), in agreement with earlier NMR data [36]. The two conformers differ by a 180° rotation of the heme moiety along the α-γ meso axis. In the main (A) conformer the metal lies within the heme plane, whereas in the minor (B) conformer it is 0.2 Å out of the heme plane; the propionate groups have identical conformations in both isomers. This difference, which is also reflected in the positions of the distal and proximal His, may account for the heterogeneity observed in the dynamics of ligand binding, as mentioned before. Moreover it is not clear if the heme orientational disorder is an artifact of heterologous Ngb synthesis in *E. coli* or an intrinsic property of the protein, as expressed in the neurons. Both hNgb and mNgb in the met hexacoordinate state possess a large cavity (120 and 290

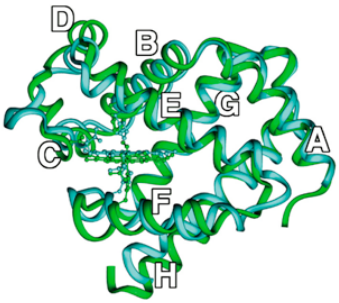

(a)

(b)

Fig. 1.3.1: **structural superposition of Ngb, Mb and nsHb based on the C_α atoms.**
The letters indicate globin helices A to H, according to standard nomenclature. **(a)** Best-fit superposition of murine Ngb (cyan) and sperm whale Mb (green). **(b)** Best-fit superposition of murine Ngb (cyan) and non-symbiontic Hb (purple).

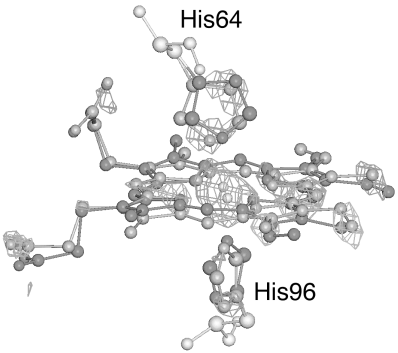

Fig. 1.3.2: **the two conformers of the heme in metNgb.**
The heme conformers A (dark gray) and B (light gray) from mice Ngb are shown (population ratio 7:3). Fo-Fc positive electron density map was calculated (contour: 3σ) omitting the heme B conformer and the distal and proximal His of the B conformer.

$Å^3$, respectively) localized among the helices E, F, G and H, endowed with a distal branch, corresponding to the distal moiety of the heme pocket; in mNgb a proximal branch, reaching the proximal heme side, is also present, including the so-called Xe1 and Xe2 binding sites identified in sperm whale Mb [56]. Such a branched cavity forms a tunnel which connects the two heme sides with the exterior and provides a potential passageway for ligands; structural rearrangements and heme sliding, following the binding of CO in mNgb, affect the topology of these cavities (see Par. 1.3.2, [55]), but not its size.
Heme orientational disorder may be related to the presence of this huge internal packing defects that leaves some empty space between the heme ring and the protein moiety; heme isomers were first identified by La Mar and co-workers to a much lesser extent (4 %) [57] in sperm whale Mb, which contains several internal packing defects [56] but lacks the huge tunnel typical of Ngb. The functional relevance of the large cavity in Ngb and Cygb is still waiting to be assessed.
In order to allow binding to the sixth heme coordination site, not only must the bond with the distal His64(E7) break, but a conformational transition has to take place in order to create space to accommodate the external ligand. In analogy with the gating role played by His64(E7) in Mb and Hb, it was initially expected that in Ngb a swinging motion of the distal His would allow, at the same time, availability of the sixth coordination position and formation of an empty niche for an external ligand to bind. Unexpectedly, determination of the structure of mNgbCO [55] showed that this protein adopts a 'heme-sliding mechanism' to remove the blockage of the binding site. In fact, CO binding

is associated to a major heme displacement within the frame of the globin fold (Fig. 1.3.3, panel a), which may imply a new mechanism for ligand affinity modulation in the globin family. Repositioning of the heme upon CO binding leaves the position of the distal His64(E7) almost unchanged (0.5 - 0.7 Å) while being associated to a displacement of the proximal His96(F8). The heme in this new position seems to reside in a pre-formed docking site and, consistently, only Phe106(G3) is drastically repositioned (by 3.8 Å). The regions that experience the largest movement upon binding are the EF-F-FG module and the CD loop that moves to a slightly more open conformation, but altogether the total rmsd displacement of the C_α is comparable to that observed in sperm whale Mb upon ligation (0.49 Å vs 0.54 Å). The 1H NMR data from met mNgb in the absence and in presence of cyanide presented by Du *et al.* [36] were analyzed by Walker [58], leading to the indication that the solution structure, the orientation of the proximal and distal histidines, could be different from the one determined in the crystal state. On the other hand EPR spectroscopy seems to indicate good agreement of solution and crystallographic parameters in met mNgb [59]. The reshaping of the large internal cavity is observed upon CO binding, with the disappearance of its proximal branch (Fig. 1.3.3, panel b) and the expansion of the distal region; moreover a new, small (13.3 $Å^3$) niche is created in the proximity of topological position D5, which is a Cys in the wild type and a Ser in the mutant used for crystallization.
MD simulations of mNgb indicate that the huge cavity likely allows the structure reshaping coupled to CO binding; it can

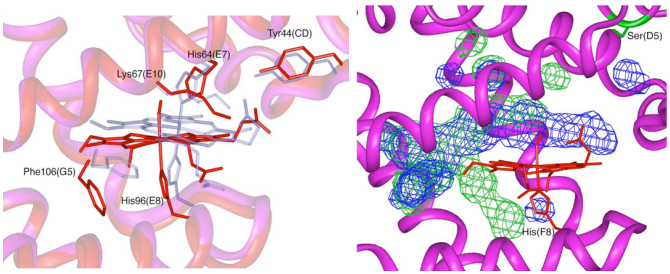

(a) (b)

Fig. 1.3.3: **heme sliding and cavity reshaping in NgbCO.**
(a) Close-up view of the active site of murine NgbCO (red) and metNgb (violet-blue). The sliding motion of heme, as well as the proximal and distal histidines and the amino acids (notably Phe106(G5) and Tyr44 in the CD turn) that undergo the largest displacements are highlighted. **(b)** The major cavity observed in NgbCO (blue) and metNgb (green) are shown. The heme displacement associated with CO binding induces a reshaping of this cavity, with the disappearance of its branch in the region proximal to the heme.

provide, at the same time, the space for the rapid (ca. 90 ns) heme sliding motion and for an easy repositioning of the EF-F-FG module and CD loop, which are coupled to CO binding, thus accounting for the similar thermodynamic stability of the protein in both the ligated and unligated state [60]. Another relevant feature of mNgbCO with respect to the internally hexacoordinate structure, is the decrease of the thermal B-factors of the EF region, that contributes the residues surrounding the access of the large tunnel to the bulk (Leu70(E13), Val71(E14),

Ala74(E17), Leu85(EF), Tyr88(EF)). The increased rigidity of the EF region might restrict external accessibility and trap small molecules inside the protein tunnel. These data are in good agreement with recent MD-XANES combined approach that clearly demonstrate the higher rigidity of the mNgb adduct with respect to the mNgbCO one [61].
In the absence of an external ligand, access to the heme distal binding side is restricted by the presence of a salt bridge between one of the heme propionates (distance of 2.7 Å) and Lys67(E10), which is reinforced by a close contact with the hydroxyl group of Tyr44(CD3) and a water molecule. This network is weakened in mNgbCO, where the minor displacement of His64(E7) induces a movement of Tyr44(CD3) that is communicated to the CD loop (Fig. 1.3.3, panel b). This is consistent with data obtained from spectroscopy and mutagenesis experiments indicating that upon ligation and mutagenesis of Lys67(E10), the accessibility of the distal site is increased [33].
In summary, the structure of NgbCO reveals the likely mechanism whereby the iron hexa-coordination, expected to considerably lower ligand affinity, is made labile enough to allow binding of exogenous ligands.
The heme sliding counterbalances the presence of internal coordination, which *a priori* should be fairly strong, leading to a different protein conformation and promoting the availability of the heme for O_2 and other external ligands. What can we infer on the mechanism of action of Ngb, in the light of the structures of its liganded and unliganded derivatives? Ngb is most likely reduced and (partly or largely) ligated by O_2 under physiological conditions (normoxia); upon deoxygenation Ngb is expected

to adopt the hexacoordinate structure.
The thermal B-factors indicate that exogenous ligand release will induce a marked change in the mobility of the EF loop and a reorganization of the CD loop. It was suggested that this conformational change may be the signal to transmit the information 'low oxygen', to allow interaction of metNgb with GDP-bound G_α to liberate $G_{\beta\gamma}$ and thus protect the cell against neuronal death [13]. Enhanced Ngb expression, as observed under conditions of hypoxia [8] would enhance this signaling pathway. Moreover, hypoxia is known to reduce the pH of a neuronal cell [46]; acidity decreases the rate of exogenous ligand binding and favors hexacoordination [33] and the coupled conformational changes involving the EF loop.

1.3.1 Crystallographic study of Ngb cavities

As discussed in Par. 1.3, Ngb shows at least two structural peculiarities: endogenous hexacoordination and the presence of a wide internal cavity. These are two uncommon features for a vertebrate globin, only Cygb and Ngb share these characteristics. While the relevance of hexacoordination for Ngb reactions has been investigated, the functional role of the huge cavity is still elusive. This cavity occupies the internal structure from the heme pocket to the EF corner, with a volume of around 300 $Å^3$, and connects the iron with the solvent (see Fig. 1.3.3 and [25]). The cavity displays two branches, which extend around the heme and connect the distal and the proximal moieties of the heme pocket. The heme sliding coupled to CO binding affects the cavity topology, drastically reducing the proximal branch

and enlarging the distal one. This ligand-induced motion also determines the repositioning of the F helix, the CD loop and the EF corner. Both crystallographic studies and MD simulations indicate that the wide cavity is necessary to accommodate the heme during the sliding motion and to allow the rearrangements of the overall structure [55, 60].
During the last decades, Mb has been a paradigmatic model to unveil the role of cavities in the diffusion dynamics of gaseous ligands (*i.e.,* O_2, CO, and NO) into the protein matrix. In 1984 Tilton and co-workers showed that Mb displays four protein matrix cavities, which can bind Xe [56]. Therefore xenon can be used to identify internal pockets in globins, since this noble gas remains trapped into cavities due to Van der Waals interactions with hydrophobic side chains.
Kinetic and crystallographic studies of photodissociated intermediates of wild type and mutant Mbs [62, 63] have shown that the Xe binding sites of Mb play a role as transient docking sites for ligands, providing a structural interpretation for the kinetics of ligand binding. These results convey the general picture that internal cavities are involved in controlling the dynamics of Mb reactions [64, 65].
In order to explore the potential role of the Ngb cavity in its reaction with ligands, Moschetti and co-workers [66] have determined the crystal structure of Ngb under pressure of xenon and krypton at 100 K. In this paper they show the presence of four xenon atoms, called XeI, XeII, XeIII and XeIV (Fig. 1.3.4 a), and two krypton binding sites, KrII and KrI (equivalent to XeII, XeIII in Fig. 1.3.4 a), both in the met form and in the CO bound derivative; the XeI atom is on the external Ngb surface,

at the interface between two symmetry-related molecules; the XeII and KrII are both placed near the interface with a symmetry related monomer, in a little breach accessible to the solvent (Fig. 1.3.4 a); the XeIII (and KrI) pocket is located above the heme plane and it consists of a hydrophobic pocket close to the EF corner, at the entrance to the tunnel connecting the heme iron with the bulk; XeIV is adjacent to XeIII and it is the atom closest to the iron and is located in the distal branch of the large cavity, between the XeIII and the heme. Inspection of the structure allows to notice that XeIII and XeIV are both located in the large cavity found in murine Ngb (Fig. 1.3.4); as shown in Fig. 1.3.4 (a), they seem to map a tunnel towards the heme, which connects the protein surface to the heme distal site.

1.3.2 Comparison of Ngb cavities with Mb and Cygb

Mb from sperm whale displays four Xe docking sites [56]. Two of these (the Xe1 and the Xe4) are closer to the heme pocket. Only MbXe4 is located distally with respect to the heme, while the other sites are on the proximal heme side. In human Cygb there are four Xe binding sites per molecule [68] that are not in the proximal site of the protein.
In Fig. 1.3.5 Moschetti *et al.* report the structural superimposition of mNgbXe with swMbXe and hCygbXe: (i) in analogy with Cygb [68] Xe atoms dock into pockets located within the large Ngb inner cavity, which is therefore able to host non-ionic gaseous ligands; (ii) one of these pockets, the NgbXeIII, displays a clear similarity with the Xe3 sites in Cygb and Mb; (iii)

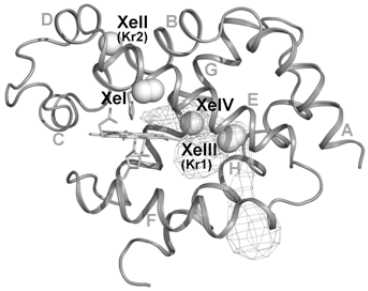

(a)

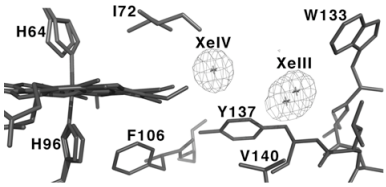

(b)

Fig. 1.3.4: **xenon and krypton binding to Ngb.**
(a) view of the Ngb protein backbone, showing the location of the four Xe atoms and the two K_r atoms (see text) represented as spheres. α-Helices have been labeled according to the globin fold topology rules. The pathway of the main tunnel and its distal branch has been calculated by using CAVER [67]. Note that the calculated tunnel starts on the proximity of the distal histidine and leads to several way of escape to the solvent. **(b)** The XeIII and XeIV atoms in the main cavity, surrounded by the heme and neighbour side chains. The electron density map for XeIII and XeIV atoms is depicted (contours: 2Fo-Fc 1.8 σ and Fo-Fc 3.36 σ).

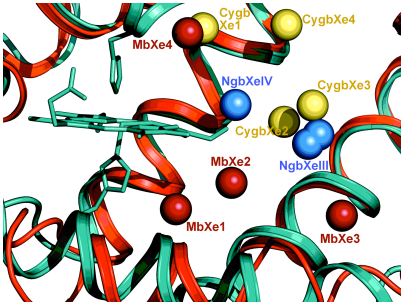

Fig. 1.3.5: **structural superimposition of mNgbXe with swMbXe and hCygbXe.**
Zoom picture of the structural superimposition in the main Ngb cavity; only the mNgb heme is depicted, as a single conformer. The overall CygbXe is not displayed, but only the relative xenon atoms.

the XeIV niche in Ngb shares similar residues with MbXe4 and CygbXe1, but its topological location is peculiar; (iv) both Ngb and Cygb lack the proximal Xe binding sites seen on Mb [56].

1.3.3 Cavities and photolytic intermediates in Myoglobin and Neuroglobin

In Myoglobin the presence of internal cavities and packing defects seems to play a role in controlling function by defining pathways for the diffusion of the ligand to the active site. These cavities are an integral part of the protein matrix and are coated by hydrophobic residues and therefore do not contain water molecules. The structure of Mb shows that the heme is deeply

Reaction:	Mb-CO ↔	Mb*CO ↔	Mb**CO ↔	Mb + CO
State:	A	B	C	S
Name:	(Bound)	(Photolyzed)	(Photorelaxed)	(Deoxy)
Ligand at:	Heme Fe	Primary docking site	Secondary docking site	Solvent

Table 1.1: **MbCO reactions under visible illumination.**

buried in the protein. Ligand binding to Mb (MbCO) has been described by a four-state scheme, as shown in Tab. 1.1. The heme-iron-CO (state A) can be photolyzed with unity quantum yield by visible light allowing synchronous initiation of the rebinding reaction. If the photodissociated ligand diffuses into the solvent (state S), rebinding to Mb will follow bimolecular kinetics. However, a fraction of the photodissociated ligand remains momentarily 'trapped' within the protein matrix; this quota may recombine by intramolecular diffusion and collision with the iron, in a process called geminate rebinding.
The migration of the photodissociated ligand can be exploited to probe the internal structure of the protein and its fluctuations on a time-scale ranging from picoseconds to microseconds. In Tab. 1.1 are shown two geminate states (B and C) because geminate rebinding can be biphasic or multiphasic.
The binding of xenon to Mb suggests that there may be a link between internal cavities and dynamic states, as shown in Fig. 1.3.6. The crystallographic data show that photolyzed CO can be seen at more than one docking site inside the protein. As shown in Fig. 1.3.6, the primary docking site is close to the Fe^{2+} in the distal pocket, the CO lying parallel to the heme plane, ~ 3.6 Å from the metal. This position, which is occupied

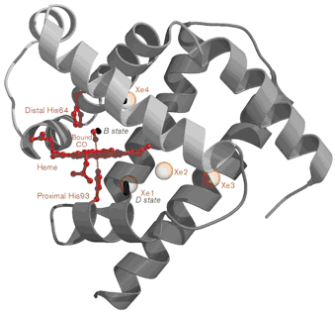

Fig. 1.3.6: **structure of the MbCO complex.**
The heme, the bound CO and the distal and proximal histidines are shown in red ball-and-stick representation. The docking positions of CO (B and D states) in wildtype Mb are shown in black. The D-state position coincides with a xenon-binding site (Xe1). Xenon is depicted by orange spheres.

a few picoseconds after photodissociation [69], is presumed to be associated with the faster geminate rebinding phase (state B). Photodissociated CO has also been observed at two secondary docking sites at greater distance from the Fe^{2+}. These overlap with two of the xenon binding sites (Xe1 and Xe4). Nienhaus and co-workers [34, 70] have investigated Neuroglobin matrix by FTIR spectroscopy in the infrared stretching bands of CO and flash photolysis at cryogenic temperature. They have observed ligand migration to the primary docking site (according to Mb's results). They also have observed CO migration to a secondary docking site, from which CO binding involves somewhat higher barriers.

1.4 *In vivo* characterisation: localization and hypoxic-induced expression

The name 'Neuroglobin' refers to the localization in the Central Nervous System (CNS). Since Ngb discovery, several groups analyzed its expression pattern in nervous tissues, also wondering whether it is continuously expressed or only in response to some *stimuli*. These data are clearly relevant for understanding the *in vivo* function of Ngb, although there are still some significant discrepancies among them.

The analysis of the RNA expression profiles shows a predominant expression in the CNS, where Ngb mRNA synthesis is observed in neuronal cells and is qualitatively absent in the vascular tissue, with major amounts localized, as referred by Burmester and co-workers [6], in the frontal lobe (the pyramidal cell layer near to the Ammon's Horn), the subthalamic nucleus and the thalamus of the adult mouse.

In several papers Greenberg and co-workers indicate that Ngb is present in the cortical region, and its expression is regulated by stress conditions, mainly hypoxic stress. Their studies reveal transient overexpression of Ngb in cultured cortical neurons exposed to acute anoxic conditions ($\sim$ 24 hr, 95% N_2 5% CO_2; [8]). In addition, neurons survival under hypoxia is reduced after Ngb-gene silencing and enhanced by Ngb overexpression [8]. Finally, using an *in vivo* rodent model of focal cerebral ischemia–reperfusion injury, Sun *et al.* [9] observed that Ngb overexpression reduces the extent of ischemic damage. They

conclude that Ngb favours neuron survival in response to acute hypoxia, protecting the brain against the ischemic damage.
Evidences exist in disagreement with experiments cited above: using ISH and quantitative RT-PCR, some authors do not detect any significant change of Ngb mRNA levels in the rat brain after transient global ischemia [71]. Some vertebrates, for instance zebrafish and turtle, live in an environment where the oxygen concentrations easily and frequently change. In these animals hypoxia dramatically increases Ngb expression in the brain. Moreover, hypoxia-tolerant vertebrates (*i.e.*, the mole rat Spalax and goldfish) express more Ngb in their brains than their related species, which are not adapted to oxygen deprivation. [6]. Based on these results, it seems that the general amount of Ngb in neurons is related to hypoxia adaptation. Only hypoxia-adapted vertebrates would be able to regulate Ngb levels in response to it; this category would then exclude mouse, rat, *H. sapiens*, and most of mammals. Finally, in seal it has been noticed a strict association of Ngb with mitochondria. Therefore, these authors conclude that the Ngb activity is probably linked to oxidative metabolism, suggesting a role as O_2 supplier or radical scavenger.
However a recent paper supports the idea that Ngb is involved in response to hypoxic stress, also in those vertebrates that are not clearly adapted to hypoxia. These experiments, carried out in mice, demonstrate that retinal cells, and in a minor extent brain cells, express higher Ngb levels upon hypoxia. In these experiments, Ngb expression follows a trend that correlates with the increase of reactive oxygen species (ROS) intracellular concentration after prolonged hypoxia (24 - 48h) and reperfusion

[72]. These results link the Ngb scavenging activity with the enhancement of cell survival, at least in retina.

1.5 Physiological role: is Ngb a neuroprotectant?

In the light of literature examined, the role of Ngb and its biochemical activity within the cell remain unclear. Here we summarize the main hypotheses under debate. One possibility is that Ngb activity is linked to oxidative metabolism [73]. Being clearly a globin, Ngb was initially thought to be an intracellular O_2 carrier, like Mb. Ngb binds O_2 reversibly with high affinity (about 2 torr at 20 °C), but the stability of the oxygenated complex *in vitro* is low and the protein undergoes a fairly rapid autoxidation [10, 37]; moreover, Ngb is expressed in the brain at low concentration (in the µM range). Therefore it seems unlikely that it may act either as an O_2 reservoir or as an intracellular carrier in facilitated diffusion.
At least in those vertebrates adapted to hypoxic environment, Ngb expression seems to be more abundant and overregulated by hypoxic *stimuli*, and the protein colocalizes with mitochondria.
Therefore one may hypothesize that Ngb could sustain phosphorilative respiration and protect terminal oxidase from the effect of toxic molecules, such as NO and related radicals.
The alternative hypothesis implies that Ngb directly protects from ischemia the cells belonging to *penumbra area*. During

the stroke, the necrotic area corresponds to the infarct localization. The *penumbra area* is composed by cells neighbouring the necrotic area: although in this region the anoxic stress can, at the end, induce apoptosis, at the beginning the cells in the penumbra are vital and able to survive. The *penumbra* is presently the principal target of therapy during the stroke. The hypothesis that Ngb protects the neurons localized in the penumbra area against hypoxia [8], promoting their survival, implies that the response to hypoxia is also a general property of mammals, including human. This scenario is prone to some objections: Burmester and colleagues proposed, based on comparative anatomy and histology of vertebrates, that most of the mammals are unadapted to hypoxia.
Another point of debate is the presence of Ngb in the cortex and its up-regulation upon hypoxia [6], since related evidences seem to suffer for very low reproducibility. But it has to be reminded that several evidences support the reliability of the scenario proposed by Greenberg and co-workers: (i) it is possible to detect Ngb mRNA and protein in the cortical region [74] (ii) Ngb expression in cortical cultured neurons is up-regulated under conditions of hypoxia [8] (iii) its overexpression reduces the extent of ischemic damage after experimental stroke in rats and mice [9] (iv) the general extent of Ngb concentration depends of hypoxic conditions and seems to counteract the ROS production, at least in retinal cells [72]. Wakasugi and colleagues [13] proposed that Ngb is a component of a signal transduction pathway, and sense the level of intracellular O_2 concentration. The main result suggesting this hypothesis was the observation that metNgb binds to the α-component of the $G_{\alpha\beta\gamma}$ protein, acting

as a guanine dissociation inhibitor (GDI), also suggesting that there is a linkage between the oxidoreduction and ligation state of Ngb and its role in signal transduction. Accordingly, Ngb would protect neurons from cell death, though it remains to be assessed whether the redox state of Ngb has any relevance in the latter mechanism.

The hypothesis that Ngb is a signal transducer is intriguing and possibly relevant to account for the neuroprotective role of this protein, expressed at such a low concentration in the brain. In a series of parallel *in vitro* studies consistent evidence was reported. Vallone *et al.* [25, 55] showed by crystallography that the conformation of Ngb is dependent on the oxidation and ligation state of the heme iron. When reduced Ngb binds CO (and presumably also O_2 and NO), a structural change was observed; thus upon CO binding to reduced Ngb, a substantial sliding motion of the heme was observed. This conformational change of the active site is associated to protein fluctuations which extend to the surface, involving in particular the EF and the CD loops. By molecular dynamics simulations it was observed [60, 40] that the CD loop populates two different conformational states. Interestingly, the CD loop is part of the contact interface between Ngb and G_α [53]. Thus it appears reasonable to correlate the ligand linked conformational change of Ngb and the formation of a complex with G_α.

A parallel finding which bears significance for the sensor function is the demonstration that oxy-Ngb reacts rapidly with NO, with formation of metNgb and harmless nitrate. Brunori *et al.* [43, 11] proposed that this is a significant property of a signal transducer, which is sensing the relative concentration of O_2 and

NO in the hypoxic nervous tissue. Given that in the *penumbral area* of the stroke, the concentration of O_2 is reduced and that of NO is increased, this mechanism may fulfill a signalling role. The scavenger properties of Ngb (see Par. 1.2.3) have been pointed out by a series of papers, and are in good agreement with both the scenarii above illustrated. During hypoxia, the increasing NO concentration (up to micromolar) determines a chain reaction leading to the formation of peroxinitrite and others related radicals in micromolar amounts (at least), which are seriously toxic for the cellular environment. Moreover, NO by itself is involved in the pro-apoptotic signalling cascade, in other words, in cell death. Interestingly, the NO and NO-radical propagation can impair the mitochondrial activity and determine Cyt-c release into the cytosol, in its oxidized form. Also this process represents a crucial regulative step in the pro-apoptotic cascade. The reaction of oxy-Ngb(FeII) with NO and the reaction of Ngb(FeII)-NO with $ONOO^-$ [48] may quench the propagation of radicals, and moreover the unligated (under low oxygen pressure) ferrous Ngb may reduce the oxidized cytosolic Cyt-c; taken together, these three processes can represent a regulative step of the incoming apoptosis, which is temporarily paused by Ngb in order to allow the survival of those cells that are rescuing a normometabolic oxygen level.

Chapter 2

Materials and methods

2.1 Gene synthesis and cloning

The synthetic gene coding for murine Ngb was supplied by GeneArt, based on the protein sequence reported in dbEST database [6], applying codon frequencies observed in *E. coli*. With respect to the wilde type sequence, we introduced the double mutation C55S/C120S in order to allow crystallization. From now on, the double mutant C55S/C120S will be referred as wt protein. The synthetic gene was assembled from synthetic oligonucleotides. The fragment was cloned into pPCR-Script using KpnI and SacI restriction sites. The plasmid DNA was purified (Pure

Yield™ Plasmid Midiprep, Promega) from transformed bacteria and concentration determined by UV spectroscopy. The final construct was verified by sequencing. Then Ngb(C55S/C120S) was cloned in the pET 3-a vector (Invitrogen), and also in the pET14-b (Invitrogen) vector which allows the expression of an N-terminal His_6-tagged protein, where the tag is removable by means of thrombin specific cleavage.

2.2 Neuroglobin expression and purification

We expressed and purified both the NGB pET 3-a and pET14-b constructs. Since only the pET14-b construct yielded crystals, we used for all our experiments this protein, and accordingly we report below only its purification protocol. All the genetic constructs, including mutants, were transformed in *E. coli* strain BL21(DE3)pLysS. Transformed cells were grown at 37 °C in Terrific Broth (TB) medium up to 0.6 OD, and then induced with 1mM IPTG in the presence of 1mM 5-deoxyaminolevulinic acid as a heme precursor; 1 hour after induction, CO was bubbled into the medium and expression was continued for 23 hours at 25 °C.
Harvested cells were resuspended in 20 mM Hepes/Na buffer pH 7.4, 300 mM NaCl and 30 mM imidazole ('lysis buffer'); RNase and DNase were added, together with Lysozime (20 mg/L of culture) and then the cells were incubated at 4 °C for 30 minutes under stirring. Subsequently cell lysis was achieved by sonica-

tion (pulse 3 s., pause 7 s., total time 10 min., amplitude 65 %). After sonication the sample was clarified by centrifugation (12.000 rpm for 20 minutes at 4 °C), and the filtered supernatant was applied to a Ni-NTA affinity column, washed to zero absorbance with lysis buffer and the protein was eluted with an imidazole gradient: the elution peak was at a 250 mM imidazole.
In order to remove imidazole, the eluted sample was exchanged with 20 mM Hepes/Na pH 7.4 using Amicon Ultra Centrifugal Filter Devices (Mw cutoff 10.000 Da), and then the Histidine-tag was removed by treatment with Bovine Thrombin (Sigma), 5 U/mg protein for 16 hours at RT. After reaction with thrombin, the sample was exchanged with 20 mM Bis-Tris pH 6.0 using Amicon Ultra Centrifugal Filter Devices (Mw cutoff 10.000 Da), and was applied to a monoQ-FF column in order to remove thrombin, histidine tags and unprocessed Ngb. Finally, the processed Ngb was eluted with an NaCl gradient up to 100 mM, concentrated with Amicon Ultra Centrifugal Filter Devices (Mw cutoff 10.000 Da), and stored at -80 °C. Concentration of wt Ngb in the deoxy state was assessed spectrophotometrically using the extintion coefficients $\varepsilon_1 = 16.2$ mM^{-1} cm^{-1} for $\lambda_{528\ nm}$ and $\varepsilon_2 = 28.9$ mM^{-1} cm^{-1} for $\lambda_{558\ nm}$ [37].

2.3 Crystallization and crystal handling

2.3.1 Neuroglobin

Ferric Ngb crystals grew in a 1:1 mixture of protein (10 mg/ml) and reservoir solution (1.6 M ammonium sulphate, 0.1 M MES pH 6.5, 10% v/v dioxane), at 20 °C in the hanging-drop setup, and their size was, in the best case, about 100 x 100 x 150 μm. To obtain ferrous derivative, ferric crystals were transferred into a suitable glass slide filled with mother liquor that contained 25% glycerol as cryoprotectant and 4 mM sodium dithionite, this solution had been previously deoxygenated by purging with N_2. A change in colour, from intense red-brownish to cherry-red, indicates a successful reduction. To obtain the ferrous Ngb(FeII)CO derivative (NgbCO), ferrous crystals were transferred from the reducing mother liquor to the same solution containing, in addition, 1mM CO. The crystals used for diffraction and UV-Vis microspectrophotometer data collection at Synchrotron radiation sources, at low temperature, were frozen in liquid nitrogen (see Fig. 2.3.1 a).

2.3.2 Horse skeletal muscle Myoglobin

Ferric crystals of horse skeletal muscle Myoglobin (HMb) grew in a 1:1 mixture of protein (9 mg/ml) and reservoir solution (2.7 M ammonium sulfate, 0.1 M Tris, HCl pH 8.0), at 20 °C in the hanging-drop method, and their size was 300 x 200 x 1.5 μm. Crystals were transferred into a cryoprotectant solution containing 25% glycerol, 0.1 M Tris, HCl pH 8.0 and 2.7 M

ammonium sulfate. After a 30 s soak, the crystals were flash-cooled in liquid nitrogen (see Fig. 2.3.1 b).

2.3.3 Sperm whale Myoglobin

Ferric crystals of sperm whale Myoglobin (SWMb) grew in a 1:1 mixture of protein (10 mg/ml) and reservoir solution (2.4 M ammonium sulfate, 0.05 M potassium phosphate buffer, pH 6.5), at 20 °C in the hanging-drop method, and their size was 38 x 38 x 12 μm. Crystals were transferred into a cryoprotectant solution containing 25% glycerol, 0.05 M potassium phosphate buffer, pH 6.5 and 2.5 M ammonium sulfate. After a 30 s soak, the crystals were flash-cooled in liquid nitrogen (see Fig. 2.3.1 c).

2.3.4 EryK P450

Ferric crystals of EryK P450 grew in a 1:1 mixture of protein (10 mg/ml) and reservoir solution (48% ammonium sulfate, 0.1 M Bis Tris buffer, pH 6.0), at 20 °C in the hanging-drop method, and their size was 38 x 38 x 12 μm. Crystals were transferred into a cryoprotectant solution containing 25% glycerol, 0.1 M Bis Tris buffer, pH 6.0 and 48% ammonium sulfate. After a 30 s soak, the crystals were flash-cooled in liquid nitrogen (see Fig. 2.3.1 d).

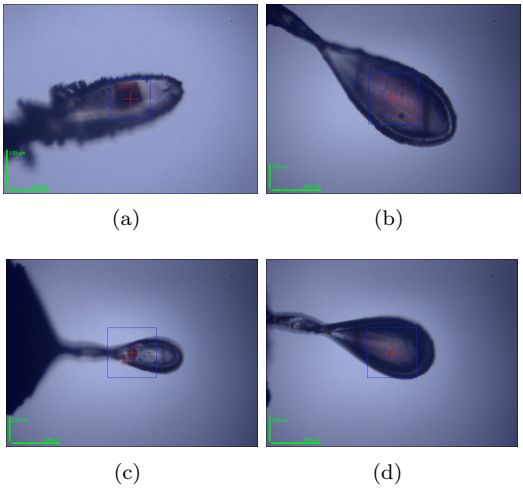

(a) (b)

(c) (d)

Fig. 2.3.1: **protein crystals, mounted in a cryo-loop.**
(a) Neuroglobin crystal. **(b)** Horse skeletal muscle Myoglobin crystal. **(c)** Sperm whale Myoglobin crystal**. (d)** EryK P450 crystal.

2.4 Experimental techniques

2.4.1 UV-Vis absorption microspectrophotometry

The UV-Vis absorption microspectrophotometry can be applied to metallo-enzymes, photosensitive proteins or whenever co-factors, substrates or products are coloured. It allows to perform low-temperature absorption on crystals mounted in cryo-loops.
The technique may be used for simple controls such as checking the presence, absence or redox state of a substrate/co-factor. UV-Vis spectroscopy has been also used in designing protocols for efficient triggering of turnover in the crystal and successful trapping of short-lifetime intermediate states [75, 76]. Although spectroscopic changes do not always accompany structural changes, it often allows to identify the presence of intermediates, especially when crystallographic data with only low resolution are available. Finally, microspectrophotometry can reveal radiation damage.

2.4.1.1 Off-line microspectrophotometer at low temperature

The off-line microspectrophotometer is available at the Cryobench of European Synchrotron Radiation Facility (ESRF, Grenoble, France). The setup includes a detector that can perform both absorption and fluorescence measurements and a detailed description has been published [77].
A schematic view of the spectrometer is shown in Fig. 2.4.1 (a),

and a picture of the apparatus in Fig. 2.4.1 (b). Samples are usually mounted in nylon cryo-loops and kept at cryo or room temperature.
A stiff mechanical support holds (i) a simple one-circle goniometer (Nonius, ref. 1511900) mounted on a horizontal axis, (ii) an observation stereo-microscope (Olympus, ref. SZ6045 TR) that allows to observe the sample from above and centre it, and (iii) a rotating arm that maintains two or optionally three identical confocal mirror objectives focusing/collecting UV-Vis light to/from the sample. A numerical camera (Olympus, ref. Camedia C3030) is connected to the observation microscope and allows to observe the sample on a video monitor or to record high resolution pictures.
The objectives are based on reflecting mirrors (Coherent, ref. 250506) to avoid spherical aberration at the sample position as well as the necessity of quartz optics to access the UV range. The focus size was measured to be 48 µm with a typical input fibre of 100 µm diameter.
Three light sources are available for absorption measurements: a cw 75 W xenon lamp used in the wavelength range 400 - 850 nm (Oriel ref. 6263, power supply ref. 68806), a cw 30 W deuterium lamp used in the wavelength range 250 - 450 nm (Oriel ref. 63163, power supply ref. 68840), and a pulsed 0.325 mJ/1.6 µs xenon lamp (repetition rate 100 Hz) used in the wavelength range 400 - 850 nm (Oriel ref. 6426, power supply ref. 68825).
Light is guided from the light source to the emitting reflecting objective through a narrow optical fibre (Spectraline, ref. FCUV100-2, typically 100 µm core diameter, NA = 0.22) and from the receiving objective to the spectrometer through a wider

optical fibre (Spectraline ref. FC-UV600-2, typically 600 µm core diameter, NA = 0.22).
The spectrometer (plug-in PC-2000, Ocean Optics Inc.) consists of a 50 µm entrance slit, a 600 lines mm^{-1} grating and a one-dimensional 2048 pixels CCD chip. It covers the wavelength range 200 - 850 nm with 2.3 nm resolution. The signal is digitized over 12 bits and the signal to noise ratio exceeds 500 at saturation level.
In conjunction with this configuration we used an open-flow Helium cryostat, called Helijet device (Oxford diffraction, shown in Fig. 2.4.3), capable of reaching 15 K, instead of the Nitrogen cryo-stream that is available and easily attain cooling down to 100 K.
The cold-helium nozzle is only 2 mm in diameter, accurate alignment is critical to keep the sample in the center of the cold stream; hence it is vital that the clamp be both stable and rigid with precise translational adjustments. The cryostat temperature controller is only used to monitor the temperature of the cryogen in the cryostat; the current design does not measure the real temperature at the sample, that it is likely to be slightly higher than temperature reported by the controller.
Crystals of Ngb were prepared in different oxidation and ligation states: ferric (Fe^{3+}), ferrous (Fe^{2+}) and ferrous CO-bound, frozen and mounted in cryo-loops under liquid N_2. The crystal orientation was optimized respect to the UV-Vis source, to maximize the signal from the metal centre with minimal baseline absorbance.
First we recorded spectra of Ngb in the ferric and ferrous form at 15 K. Next we mounted NgbCO crystals and we collected

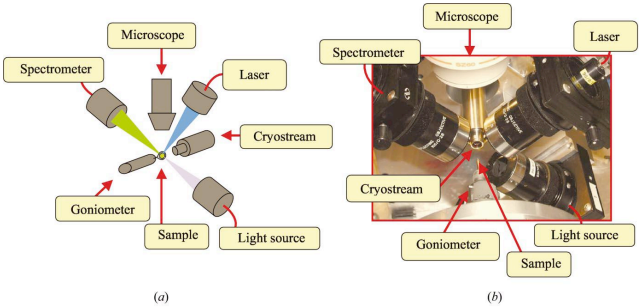

Fig. 2.4.1: **UV-Vis microspectrophotometer off line**.
(a) Schematic view of the absorption spectrophotometer. **(b)** Corresponding picture of the device.

spectra both at 15 K. We observed a spectral evolution under visible light at 15 K, that we assigned to photolysis induced by the probe lamp. We cycled the temperature from 15 K to 30 K and vice-versa, in order to confirm the reversibility of the rebinding process observed.
The temperature was varied manually, rotating the 'needle valve' of the Helijet because the computerized controller was not available during this experiment. This posed a problem, because the change of temperature is connected with a sudden change of helium flux, enhancing the formation of ice on the crystals. Crystal icing and mechanical microfluctuation due to gas flux led to a variation of the focus and optic length, thus affecting the quality of the spectra.

2.4.1.2 On-line microspectrophotometer

A compact and portable microspectrophotometer was designed specifically as a module for the standard ESRF MX diffractometers. Two identical catadioptric objectives were mounted on a solid bracket that was in turn bolted to a high-precision XYZ translation stage. The objectives are mounted at 45° with respect to the φ axis to allow access for the cryostream, the X-ray fluorescence detector and the sample changer. In Fig. 2.4.2 are visible the Nitrogen cryostrem (Oxford Cryosystems Cryostream) (1), the on-line microspectrophotometer (2) and the goniometer with the loop mounted crystal (3).
The on-line microspectrophotometer is equipped with a combine deuterium-halogen lamp (DH-2000, Oceans Optics) and a HR4000 spectrophotometer (Oceans Optics). It allows recording absorption spectra from 250 to 850 nm. The focus of the spectrophotometer (nominal spot diameter of 25 μm) is smaller than that the X-ray beam, ensuring that only X-ray irradiated material contributes to the recorded spectra.

The microspectrophotometer was mounted at the diffractometer of beamline ID14-2 at ESRF. UV-Vis absorption spectra of crystals of sperm whale Myoglobin (SWMb), horse skeletal muscle Myoglobin (HMb), murine Neuroglobin (Ngb) and EryK P450 (EryK) were kept at 100 K in a gaseous nitrogen stream and were recorded before, during and after X-rays exposure. To irradiate all the crystal we needed to change beam size for each crystal, depending on its dimension: SWMb was invested with a flux of 1.52 x 10^{11} photons/s and the beam size was fixed at (0.2 x 0.2) mm; HMb has was invested with a flux of 1.51 x

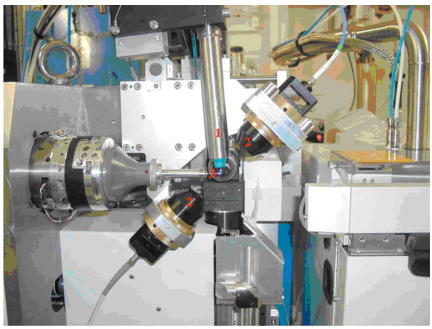

Figure 2.4.2: **UV-Vis microspectrophotometer on-line.**
Device in which are visible the nitrogen cryostrem (1), the on-line microspectrophotometer (2) and the goniometer with loop mounted crystal (3).

10^{11}photons/s and the beam size was (0.2 x 0.2) mm; Ngb was invested with a flux of 3.37 x 10^{10} photons/s and the beam size was fixed at (0.1 x 0.1) mm; EryK was invested with a flux of 1.15 x 10^{11} photons/s and the beam size was fixed at (0.2 x 0.2) mm.
The orientation of the crystal with respect to the UV-Vis source was optimized to maximize the signal from the iron with minimal baseline absorbance. The crystal was kept fixed in this position with respect to the UV-Vis and X-ray beams during irradiation. All the crystal were irradiated at 13.3 KeV.
For the acquisition of spectra of Myoglobins and Neuroglobin we used the halogen lamp of the microspectrophotometer that gives the possibility to visualize a range of wavelength between

400 and 850 nm, while for the acquisition of EryK spectra the halogen lamp plus the deuterium lamp to have a wider range of wavelength (250 – 850) nm and to analyzed also Soret peak.

2.4.2 Crystal structure determination by X-Ray Diffraction (XRD)

Here we describe the data collection conditions, and the procedures followed for data reduction and structure determination, including the program packages utilized.
All the crystals were isomorphous with the Ngb crystals measured previously [55, 25]. Data were indexed and processed by using the programs DENZO and SCALEPACK [78], or MOSFLM and SCALA [79]. The CCP4 program suite [80] was used for subsequent structure refinement. Initial phases were derived from the deposited structures of Ngb and NgbCO [55, 25]. The models were subjected to iterative rounds of refinement and model building. Refinement was carried out with Refmac5 in CCP4 [81, 82], followed by model adjustment and water addition with COOT [83]. The quality of the final model was analyzed by using PROCHECK [84].
We performed XRD data collection both at room and low temperature, to investigate the migration of a small ligand in the Ngb matrix. At low temperature there is the possibility to trap an intermediate, while measurements at room temperature give the possibility to study the sample at physiological conditions, exploring its dynamics, compatibly with crystal packing.

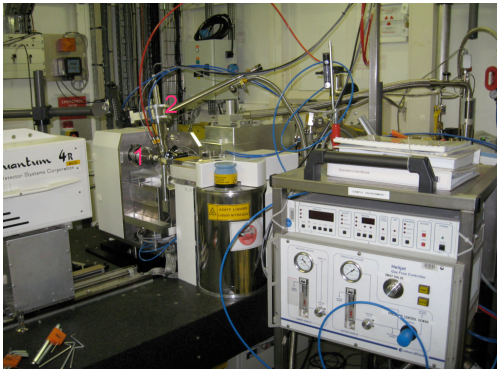

Fig. 2.4.3: **protein crystallography line.**
Frozen crystals were mounted in the goniometer with a cryo-loop. To achieve a low temperature, the Helium-jet device (2) was mounted on the line.

2.4.2.1 XRD at low temperature

X-ray data collections at low temperature were carried out at ESRF, ID14-2 beamline, at a wavelength of 0.933 Å and using a ADSC Q4 CCD detector. The temperature was set in a range between 15 and 30 K, using the Helijet device connected with a temperature controller, shown in Fig. 2.4.3, instead of the Nitrogen cryostream.
Frozen NgbCO crystals were mounted in a cryo-loop and for each sample we collected diffraction data sets at 40 K ('dark' state) and at 15 K under illumination ('light' state). During the experiment, icing problems hampered diffraction data qual-

ity and we could not collected highly redundant data sets. To conduct this experiment we attempted two strategies to achieve photolysis, by an optical fiber microscope lamp, and by using a laser focused and centered using the microspectrophotometer optics. We could not record spectra or utilize the laser to achieve photolysis, since it was incompatible with Helijet flow stability and it caused severe icing.

2.4.2.2 XRD at room temperature

X-ray data collections at room temperature (about 300 K) were carried out at the BM16 beamline (ESRF) at a wavelength of 0.979 Å and using a ADSC Q210r CCD detector. Crystals were mounted in a quartz capillary fitted to a specially designed pressurized stainless steel cell, as shown in Fig. 2.4.4 [85, 86]. The device was supplemented (see Fig. 2.4.4 b) by a metering valve, a bleeder valve, and a 'quick' connector, which allowed one to disconnect (and reconnect) the pressure cell from the 'gas-line' without loss of pressure inside the cell. The pressure cell was connected to the gas tank and a few pressurization-depressurization cycles (by alternatively opening and closing the metering valve and the bleeder valve) were made to purge the residual air out of the system. Data collection were carried out on ferric Ngb crystals, under constant pressure of gas (CO, Xe, O_2) maintained during all data acquirement. We kept data of Ngb in the native form (without gas pressure), under Xe (at 17 bar), O_2 (at 10 and 20 bar) and CO (at 5, 20, 30 and 40 bar). We usually waited for a short equilibrium time ($\sim$ 10 min.), before data recording under gas pressure.

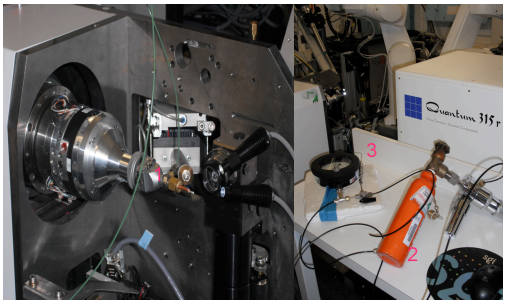

(a)

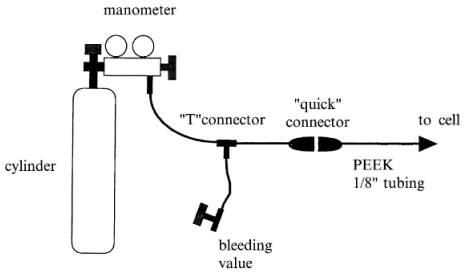

(b)

Fig. 2.4.4: **XRD at room temperature set-up.**
(a) Crystals were mounted in a quartz capillary fitted to a specially designed pressurized cell (1) and were kept under costant gas pressure (2), maintained during all data collections and controlled by manometer (3).**(b)** Schematic view of 'gas-line'.

2.4.3 X-ray Absorption Spectroscopy (XAS)

In this section a brief description of the aim of XAS experiments and of the theory underlying XAS ones. For a more extensive discussion on the XAS technique, we refer to the literature [87, 88].

2.4.3.1 XAS aims

XAS allows to determine the local structure of metal sites, revealing structural parameters with a very high precision, since the accuracy of this technique is about 0.02 Å.
As discussed in the next paragraph (2.4.3.2), XAS theory focuses either on the Extended X-ray Absorption Fine Structure (EXAFS) [89] or the X-ray Absorption Near Edge Structure (XANES) [90, 91]. EXAFS analysis is a method to extract structural data from metal sites from the high energy range of the spectrum [92], and allows to determine: radial distance, coordination numbers and types of ligand. XANES analysis is able to assess the metal oxidation state, site symmetry and coordination state and, by means of appropriate modelling and fitting [93], can be also used to determine structural parameters.

2.4.3.2 XAS basics

XAS makes use of photons in the X-ray region of the spectrum; these photons carry an energy of about 104 eV, corresponding to a wavelength of about 1 Å, and are therefore able to excite the energetic levels of core electrons, easily leading to photodissociation of an electron from its core energy level (this is the reason

for X-rays to be referred to as 'ionizing' radiation). Based on these effects, XAS spectra provide a description of the absorption coefficient of an element in the gaseous, liquid or solid state, as a function of the X-ray energy. In general, the useful elements for XAS studies range from S through the remainder of the periodic table.
In the biological application of this technique, a sample of a metal-bound biological macromolecule is probed with X-rays in order to access information (both electronic and structural) around the metal site. Probing atomic and molecular structure is possible since the X-rays are in the Angstrom-scale, the same range of the interatomic distances. XRD makes use of this property of X-rays and can provide detailed atom-by-atom structural information.
At variance of XRD, XAS provides more limited local structural information but does not require samples with long-range order (the crystalline state). In order to collect XAS spectra, it is necessary to scan the absorption spectra of an element through a range of wavelengths. Moreover, the energy content of the radiation has to be very high since the useful signal is about 1:1000 of the total energy provided. Due to these two requirements, XAS experiments can be carried out only at synchrotron radiation sources, which provide wavelength-tunable radiations displaying high brilliance (energy content) within a large energy range. During the spectroscopic scan no absorption occurs until the photon has an energy equal to the ionization energy of core electrons. At significantly higher X-ray energies, photoionization of a 1s electron gives rise to the K X-ray absorption edge. In fact, the X-ray photon absorbed ($h\nu$) results in transitions

Element	Energies (keV) at the K-edge
S	2.5
Mn	6.6
Fe	7.1
Ni	8.3
Cu	9.0
Mb	20.0

Table 2.1: **energies at the K-edge of different elements.**

within the atomic energy levels of the absorbing atom. The absorbed photon is also able to eject a core photoelectron from the absorbing atom, leaving behind a core hole. The atom with the core hole is now excited. The ejected photoelectron's energy will be equal to that of the absorbed photon minus the binding energy of the initial core state (see Eq. 2.1).
Then the ejected photoelectron will interact with electrons in the surrounding non-excited atoms, determining the features typical of both the XANES and the EXAFS spectral region (see below for the description of EXAFS and XANES regions).
The photon energies required for the edges of some selected elements are summarized in Tab. 2.1.

For a given element, K edge energies depend slightly (± a few eV) on the chemical environment of the element. For example, higher oxidation state metals have higher positive charge, making it slightly more difficult to photodissociate a 1s electron, shifting the K edge to higher energy. Shifts of 1 - 2 eV per oxidation state are typical for first-row transition metals.

Also, spectroscopic transitions from the 1s orbital to orbitals such as 3d, 4s, 4p, etc., can provide information about molecular symmetry. X-ray absorption spectra show a steep rise at the core-level binding energy of X-ray absorbing atoms and attenuates gradually with the X-ray energy.
The XAS spectra are usually divided in three energy regions (see Fig. 2.4.5):

1. the edge region
2. the X-ray Absorption Near Edge Structure (XANES)
3. the Extended X-ray Absorption Fine Structure (EXAFS)

and each of these accounts for a different phenomenon contributing to several features of the spectra.
The absorption peaks at the absorption edges in a range of about 5 eV are due to electronic transitions to first unoccupied molecular levels above the chemical potential.
The energy region extending over the edge for a range of about 100 eV is assigned to multiple scattering resonances, and is called XANES. The oscillatory structure extending for hundreds of electron volts past the edges is assigned to the single scattering of the excited photoelectron by neighbouring atoms, and corresponds to the EXAFS region.
The absorption peaks of XANES spectra are determined by multiple scattering resonances of the photoelectron excited at the atomic absorption site and scattered by neighbour atoms. The local character of the final states is determined by the short photoelectron mean free path, that is strongly reduced (down

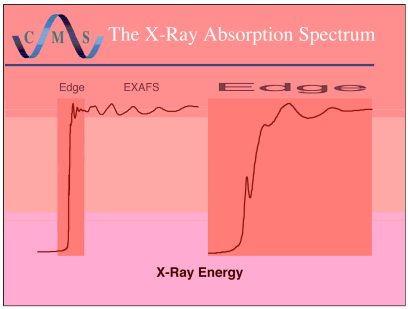

Fig. 2.4.5: **XAS spectra.**
Left panel shows the typical feature of X-Ray absorption spectra as a function of the X-ray energy. Right panel is an enlargement of the peak/XANES region (from 'X-ray absorption spectroscopy of metallobiomolecules', R. A. Scott, University of Georgia, Athens USA).

to about 0.3 nm at 50 eV) in this energy range because of inelastic scattering of the photoelectron by the surroundings valence electrons.

The EXAFS spectrum in the high energy range extending from about 150 eV beyond the ionization potential. The final state of the excited photoelectron in the high kinetic energy range (150 - 2000 eV) is determined by single backscattering events due to the low amplitude photoelectron scattering. In fact, if the ejected photoelectron is taken to have a wave-like nature and the surrounding atoms are described as point scatterers, it is possible to imagine the backscattered electron waves interfering with the forward-propagating waves. The resulting interference

pattern shows up as a modulation of the measured absorption coefficient, thereby causing the oscillation in the EXAFS spectra.
A simplified plane-wave single-scattering theory has been used for interpretation of EXAFS spectra for many years, although modern methods (like GNXAS [94, 92]) have shown that curved-wave corrections and multiple-scattering effects can not be neglected. The photoelectron scattering amplitude in the low energy range (5 - 200 eV) of the photoelectron kinetic energy become much larger so that multiple scattering events become dominant in the XANES spectra.
The different energy range between XANES and EXAFS can be also explained in a very simple manner by the comparison between the photoelectron wavelength λ and the interatomic distance of the photoabsorber-backscatterer pair. The photoelectron kinetic energy is connected with the wavelength λ by the following relation (2.1):

$$E_{kinetic} = h\nu - E_{binding} = \frac{\eta^2 k^2}{2m} = \frac{(2\pi)^2 \eta^2}{2m\lambda^2} \qquad (2.1)$$

that means that for high energy the wavelength is shorter than interatomic distances and hence the EXAFS region corresponds to a single scattering regime; while for lower E, λ is larger than interatomic distances and the XANES region is associated with a multiple scattering regime.

2.4.3.3 XANES measurements on NgbCO in solution

Fe-K-edge XAS spectra of NgbCO were collected in Fluorescence mode at the BM30B FAME beamline at ESRF. All spectra were collected at 15 K or at higher temperature as explained below.
The storage ring was running in the two-third filling mode with a typical current of 170 mA. The monochromator was equipped with a Si(111) double crystal, in which the second crystal was elastically bent to a cylindrical cross section. The energy resolution range at the Fe-K-edge is 0.5 eV. The X-ray photon beam was vertically focused by Ni-Pt mirror, and dynamically sagitally focused in the horizontal size. An array detector made by 30 Ge elements of very high purity was used. The spectra were calibrated by assigning the first inflection point of the Fe foil spectrum to 7111.2 eV. We collected each XANES spectrum in 20 minutes and each EXAFS spectrum in 45 minutes. For the CO derivative we observed a clear spectral evolution when the beam spot was kept fixed at 15 K. This process was interpreted as Fe-CO bond rupture by X-ray at low temperature [87].
Recently, the whole process has been characterized for the sperm whale MbCO derivative, to demonstrate that the X-ray induced photoproduct at low temperature is the same that the light induced one and is a common feature of CO bound hemeproteins [95]. Moreover even the reversibility has been assessed, so that by means of this novel experimental setup we were able to acquire for Neuroglobin, the spectrum of a largely photolyzed species at low temperature after prolonged X-ray exposure (Ngb*CO). This spectrum was compared with a spectrum

collected at 100 K, where rebinding process was much faster than the acquisition time and the species was considered completely CO-bound (NgbCO). Finally, by fitting using MXAN package [93] the difference spectrum Ngb*CO - NgbCO, according to the method previously described [96], we were able to determine the local structure around the iron metal site for the X-ray induced photoproduct.

2.4.3.4 Polarized XANES measurements on NgbCO crystals

XANES fingerprints are usually interpreted to elucidate the oxidation state and the overall symmetry of the metal site by direct comparison with model standards [97]. Furthermore, in the case of hemeproteins, in many cases the XANES dichroism of the heme can be exploited.
In the general case, assuming that the incident beam is linearly polarized along a direction denoted by the vector ε, each spectrum j (*i.e.*, each crystal orientation) samples a particular direction ε_j. The fluorescence intensity emitted as a function of the energy E from a small crystal is proportional, within the dipole approximation of the photoelectron absorption cross section, to the quadratic form σ_j (see Eq. 2.2)

$$\sigma_j(E) = \varepsilon_j^T \sigma_j(E) \varepsilon_j \tag{2.2}$$

where σ(E) denotes the absorption tensor, the superscript T indicates the transpose, and σ_j(E) denotes the effective scalar linear absorption coefficient along the direction ε_j. According to

the crystal symmetry, the absorption tensor is provided by a certain number of orientation-dependent spectra, and the 'solution equivalent spectrum', comparable with the solution spectrum, is obtained by the trace of the tensor, divided by three [98].
When the local structure around a metal center has a C4 symmetry (approximately the one of the Fe-heme site), a simplified approach can be adopted. First, it is advantageous to consider the XAS components linearly polarized along its symmetry axis (the heme normal), I_{normal}, and along a direction in the C4 plane (the heme plane), I_{heme}.
Assuming perfect C4 symmetry, for a certain angle ϑ between the polarization vector ε and the heme normal, the polarized spectrum is given, as a function of I_{heme} and I_{normal}, simply by Eq. 2.3

$$I_\vartheta = I_{normal} \cos^2 \vartheta + I_{heme} \sin^2 \vartheta \tag{2.3}$$

that means that the X-ray absorption cross section of the heme is approximately dichroic; in the presence of m symmetry related hemes in the unit cell of the crystal it is possible to write Eq. 2.4:

$$\begin{aligned} I_\vartheta &= \frac{1}{m} \sum_1^m \left(I_{normal} \cos^2 n_i\vartheta + I_{heme} \sin^2 n_i\vartheta \right) \\ &= \frac{1}{m} \left[I_{normal} \sum_1^m \left(\cos^2 n_i\vartheta \right) + I_{heme} \sum_1^m \left(1 - \cos^2 n_i\vartheta \right) \right] \\ &= a_\vartheta I_{normal} + b_\vartheta I_{heme} \end{aligned} \tag{2.4}$$

where $a_\vartheta = (1/m) \sum_1^m \left(\cos^2 n_i\vartheta \right)$ and $b_\vartheta = 1 - a_\vartheta$; ϑ is now a rotational angle of an oriented crystal in the laboratory system,

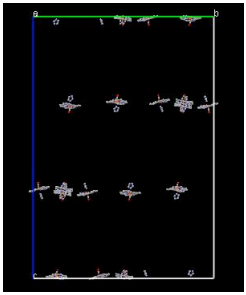

Fig. 2.4.6: **Sketch of the 18 hemes of murine NgbCO (R32 space group) in its crystal unit cell.**

and $n_i\vartheta$ are the angles between each heme normal n_i and the X-ray polarization vector ε, that correspond to ϑ.
The more the m symmetry-related heme planes are oriented parallel (or antiparallel) in the unit cell, the more the XAS dichroism is maintained in the single crystal; in this case the XAS angular dependence can provide an enhanced resolution of the heme site with respect to both X-ray crystallography and solution XAS.
The murine Neuroglobin, that is a monomeric protein arranged in the orthorhombic R32 space group, has the unit cell that contains 18 protein monomers, and the corresponding heme groups are shown in Fig. 2.4.6, in the case of the carbonmonoxy-derivative (PDB code 1W92). The molecules of the prosthetic group are still oriented approximately parallel or antiparallel to each other, and the heme normals are very close to the c-axis:

$a_{\vartheta=c} = 0.95$ along this direction.
By rotating the crystal around the a-axis or the b-axis it corresponds to a variation of a_ϑ between 0.024 and 0.95, so that the extraction of the pure I_{normal} component is favorable in a beamline equipped for orienting the crystal along a specific crystal axis.
Polarized XANES on single crystals have been proved to be a valuable tool to elucidate at atomic resolution the local structure of the metal site under investigation [99]. Polarized spectra can directly provide the axial ligand coordination by suppressing the I_{heme} contribution, whose major intensity is predominant in solution [100, 101].
The polarized XANES spectra (in fluorescence mode) of NgbCO single crystals, collected at 100 K, were measured at Daresbury, CCLRC 10.1 beamline. The crystal, in a loop, was mounted on a goniometric head. The b-axis of the rombohedric cell was oriented parallel to the axis of the goniometric head and each angular position around b-axis was reached by a step of motor having a formal accurancy of 0.01°. However, the real error depends on the accuracy by which the initial direction of the a-axis was marked, evaluated as ± 2°. The same single crystals were used when acquiring XANES spectra at different orientations.
We analyzed XAS data by means of the MXAN software package [93] for the low energy range (XANES regime). We systematically applied two methods and we compared for the calculation of the Muffin Tin (MT) potential (namely, 'SCF-fixed' and 'optim.') showing the effect on the choice of potential parameters with respect to the final results. In fact, in spite to the occasional differences found in the final values of the structural

parameters, we did not find relevant differences in the residual square function of the best fits, justifying a choice between them. Therefore, we considered these procedures as two independent methods whose accuracy is affected by its own systematic errors.
We averaged values of distances and angles as last step, and their respective error was obtained from uncertainty propagation theory. Both the procedure for the MT potential calculation were described in previous works: 'SCF-fixed' procedure in [102, 99] and the 'optim' procedure in [101].
We also calculated the real part of the exchange term using the Hedin-Lundqvist energy-dependent potential [103], while all of the inelastic losses were taken into account by convolution with a phenomenological broadening function $\Gamma = \Gamma_c + \Gamma(E)$. The constant part Γ_c includes contributions from the core-hole lifetime, while the energy-dependent term $\Gamma(E)$ represents the inelastic process.
The experimental resolution was taken into account by a Gaussian convolution (0.6 - 0.8 eV) of the theoretical spectrum. The method introduces two free parameters linked to the potential, and two parameters linked to $\Gamma(E)$, that are derive during the fit [101]. The Fe-porphirine macrocycle, and the ligand molecules, were included in the atomic cluster used for XANES analysis; we choose the cluster size and the I_{max}value (*i.e.*, the maximum l value of spherical harmonic expansion of the scattering path operators) on the basis of a convergence criterion.

Chapter 3

Results and discussion

3.1 Heme environment determination of NgbCO: XANES spectra

According to MD simulation, the heme sliding distributions along its first essential engivector in the crystal and in solution [60, 104] are different at room temperature for NgbCO. In solution, the conformational distribution is peaked around a position close to the crystallographic structure of deoxy-Ngb (*i.e.*, with no heme-sliding and a 'flip-flop' motion of the CD corner upon CO binding). In the crystal the MD simulation at room temperature shows a double-peaked distribution. A first, higher maximum is around a position close to the crystallographic structure of NgbCO, with sliding of the heme and

the CD corner almost 'frozen' in the position observed in the crystal. A second, lower one, is located near that of deoxy-Ngb. However, in the cryo-trapped crystal, only the first conformation is observed by XRD as significantly populated. Accordingly, in our XAS experiments in solution, at cryogenic temperature, the entire conformational ensemble, centered around the deoxy-like one (with no heme sliding), should be probed. Conversely in the crystal, only the more populated conformation, visualized by XRD (with heme sliding) should contribute to the measured XAS spectra.

The XAS measurements were carried out on NgbCO, both in a single crystal opportunely oriented and in solution. In Fig. 3.1.1, the Fe-K-edge XAS analysis of murine NgbCO are displayed.

The crystal of NgbCO with a space-group R32 shows a very strong XAS angular dichroism, allowing to extract the I_{heme} and the I_{normal} components form the experimental XANES spectra collected at various angles. The two components are depicted in panel A and B of Fig. 3.1.1 (panel A is a blow-up of the pre-edge region). The 2:1 weighted average of the two components and the solution XANES spectrum are also displayed for visual comparison. In panel C and D, the I_{heme} the I_{normal} XANES spectra collected onto R32 crystal of NgbCO are reported (open circles), together with the best fitted spectra (solid line) found using MXAN package. In panel E we report the Fourier transform of the EXAFS solution spectrum of NgbCO (dots) and the best fit obtained via the GNXAS package (solid line).

The relevant structural parameters obtained by the combination of all of these measurements are displayed in Tab. 3.1 and compared with results from 1.7 Å resolution XRD. Only the Fe-N_p

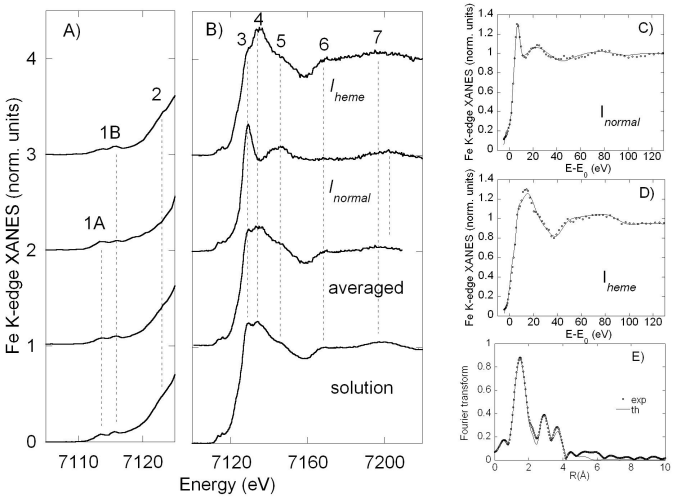

Fig. 3.1.1: **NgbCO XAS spectra.**
Panels **(A)** and **(B)** shows the pre-edge and Fe K-edge XANES spectra of NgbCO. From top to bottom: $I_{heme}$and I_{normal} , their weighted average giving the 'solution equivalent' spectrum and the experimental solution XANES spectrum. Eight labeled features (1A, 1B, 2-7) are discernible in all spectra. Panel **(C)** and **(D)**: MXAN best fits (solid lines) of I_{normal} and I_{heme} (open circles). Panel **(E)**: Fourier transform of the EXAFS spectrum in solution (dots) and best fit obtained by the GNXAS procedure (solid line).

distance is obtained from the analysis of I_{heme}, whereas the axial parameters are derived from I_{normal}. As the experimental I_{heme} spectrum of NgbCO is available only up to 120 eV beyond the edge, the MXAN analysis of this spectrum is carried out on a shorter energy range as compared to all the other experimental spectra, that are analyzed up to about 200 eV beyond the edge. As a consequence, a lower accuracy on the Fe-Np distance is obtained: 2.05 (7) Å by using the 'SCF-fixed' method, and 1.97 (2) Å by using the 'optim' one. The average of the results from the two methods ('SCF-fixed' and 'optim', see Par. 2.4.3.4) gives a better agreement with the independent determination by XRD and EXAFS in solution.
The high similarity between the two experimental XANES spectra (crystal and solution) gives the best direct evidence that the crystal preparation protocol does not induce relevant constraints, at least at the level of the Fe-heme structure of NgbCO. In spite of the large rearrangement of the protein environment and of the heme location predicted by MD, the local structure around the Fe ion in NgbCO determined by XAS seems unaltered between crystal and the solution sample. This result reinforces the model proposed to explain the functional transition of the protein when an exogenous ligand replaces the distal histidine in the sixth position. The residual energy involved in the protein relaxation responsible of cracking the crystal does not reside in the heme pocket, but it is rapidly transferred at peripheral sites of the protein (more likely the CD corner) so that the final tertiary rearrangement of the protein in solution can be reached.

experiment	Fe-Np (Å)	Fe-His (Å)	Fe-CO (Å)	tilt (deg)	bend (deg)	C-O (Å)
XRD 1.7 (Å)[b] [55]	2.00 (15)	2.11 (18)	1.81 (14)	-	22	1.03 (15)
XANES (SCF-fixed)	2.05 (7)	2.07 (3)	1.85 (3)	14 (17)	10 (10)	1.12 (3)
XANES (optim)	1.97 (2)	2.06 (2)	1.86 (3)	10 (3)	19 (5)	1.23 (2)
average	2.01(3)	2.06 (2)	1.85 (2)	12 (9)	15 (6)	1.17 (6)
EXAFS (solution)	1.99 (1)	2.10 (4)	1.81 (2)	-	7 (7)	1.08 (2)
XANES (solution)	2.02 (2)	1.96 (7)	1.86 (5)	-	8 (8)	1.10

Table 3.1: **NgbCO structural determination by XAS.**
[a]Numbers in parentheses represent the statistical error of the last digits. [b]Estimated standard uncertainties are calculated by using DPI_{Rfree} [105]. Standard uncertainty on the Fe–C–O angle is not quoted as it has been refined automatically based on the restraint listed in the CCP4 library.

3.2 Redox state determination: UV-Vis microspectrophotometry (on-line) on crystal

It has been shown that metalloproteins are partly reduced during X-ray irradiation [106, 107, 108] because metal co-factors can absorb free electrons thereby changing their oxidation states; this phenomenon can affect their conformation and coordination, respectively, and thereby the three-dimensional structures of the ligating proteins. Therefore X-rays serve not only as a probe but are in fact also a pump. For many metallo- and particularly hemeproteins determining the redox state of the metal centres is relatively straightforward because they have unique UV-Vis absorption spectra [109] that are sensitive towards changes of the heme group and its surroundings. Their spectra can be monitored in crystals by microspectrophotometry as shown in a variety of publications [110, 111, 112, 113].

The unequivocal characterization of defined redox states is not a trivial task because electrons liberated in the sample by X-ray during crystallographic data collection can alter the redox state of the active site.
From XAS measurements made on Ngb solution at 15 K [87], there is the evidence that Ngb is subjected to a fast photoreduction, upon X-ray exposure; initially we thought that this was a peculiar feature of Ngb, that is an hexacoordinate system, connected with its redox function, so we have performed a comparative study of four different hemeproteins (one is an hexacoordinated system and the others are pentacoordinated systems), in order to understand if the are differences in the rate of photoreduction in these four systems. We analyzed crystal of sperm whale Myoglobin (SWMb), horse skeletal muscle Myoglobin (HMb), murine Neuroglobin (Ngb) and EryK P450 (EryK).
We followed the $Fe^{3+} \rightarrow Fe^{2+}$ reduction of the heme iron in all samples, induced by X-ray flux and Fig. 3.2.1 represents absorption spectra of photoreduction of met-SWMb (a), met-HMb (b), met-Ngb (c) and met-EryK (d) that we acquired with the online UV-Vis microspectrophotometer (see Par. 2.4.1.2).
In Fig. 3.2.1 (a) SWMb photoreduction is shown; the black line corresponds to SWMb sample before illumination and it has the typical aspect of Myoglobin at pH = 6.5 [114]. During X-ray exposure heme photoreduction in the crystal has occurred: two new double peaks at 530/537 nm and 557/567 nm arise; the violet line (n17) represents the spectrum of the ferrous form of sperm whale Myoglobin which has a water molecule at the sixth ligand position of the heme iron, given the crystal tem-

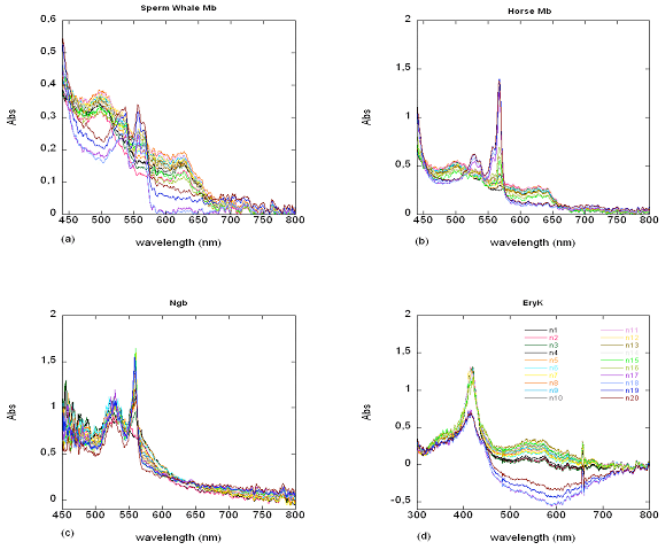

Fig. 3.2.1: **absorption spectra of four samples analyzed.**
They were acquired before, during and after irradiation at 13 keV: SWMb **(a)**, HMb **(b)**, Ngb **(c)** and EryK **(d)**.

perature at 100 K. This is a thermally trapped non-equilibrium state where a water molecule is still bound to the iron after the $Fe^{3+} \rightarrow Fe^{2+}$ transition. The brown line (n20) represents the mean of all spectra after X-ray illumination; it has the same form of the last spectrum (blue line, n19) during X-ray illumination, so we can observe that there is no change in the spectrum after turning off X-ray illumination. Fig. 3.2.1 (b) shows HMb photoreduction; the black line corresponds to HMb sample before illumination and it has the typical aspect of Myoglobin at pH = 8.0. The change in the UV-Vis absorption spectrum of ferric horse Myoglobin upon X-ray irradiation is evident: during irradiation two new double peaks at 528/537 nm and 557/567 nm arise, according to Schlichting *et al.* [114, 108]. Fig. 3.2.1 (c) shows absorption spectra of met-Ngb crystals kept at 100 K, before, during and after X-ray exposure. The black line corresponds to the sample before illumination and it has the typical aspect of met-Ngb. During irradiation two new peaks at 528 nm and 558 nm arise, corresponding, as reported in the literature, to the Fe^{2+} redox state [37]. EryK photoreduction is shown in Fig. 3.2.1 (d) and the black line corresponds to met-EryK sample before illumination [115].
The influence of background on absorbance measurements is very strong and we therefore proceeded to subtracting the contribution of cryoprotectant solution to the absorption spectra of protein crystals. Fig. 3.2.1 (a, b, d) represents absorption spectra of SWMb, HMb and EryK, after the subtraction of background contribution; Ngb absorption spectra have been not corrected because background contribution appears negligible. In Fig. 3.2.2 we report the time course of photoreduction for each

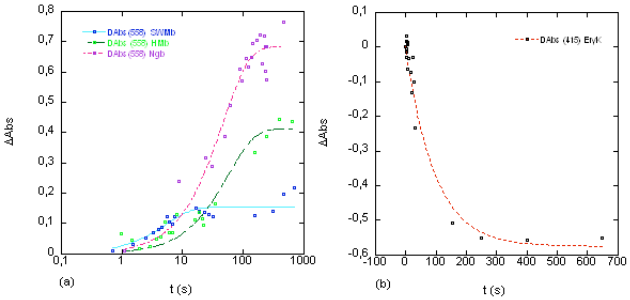

Fig. 3.2.2: **time course of four hemeproteins.**
(a) Time course of the 558 nm peak of sperm whale Myoglobin (blue circle) and its relative exponential fit (marine line), horse Myoglobin (green circle) and its relative exponential fit (green dashes), and Neuroglobin (violet circle) and its relative exponential fit (pink dashes); **(b)**: time course of the 415 nm peak of EryK and its relative exponential fit (red dashes).

sample. Fig. 3.2.2 (a) represents time course of the 558 nm peak of sperm whale and horse Myoglobin and Neuroglobin; Fig. 3.2.2 (b) represents time course of the 415 nm peak of EryK.
Each spectrum has been fitted with an exponential function, as described by eq. 3.1:

$$y = a\left(1 - e^{-kt}\right) \tag{3.1}$$

In Tab. 3.2 we report exponential fit results for different samples; the parameter k represents the rate constant of photore-

Sample	a (u.a.)	k (s^{-1})
SWMb	0.154 ± 0.009	0.18 ± 0.03
HMb	0.41 ± 0.02	0.018 ± 0.003
Ngb	0.68 ± 0.02	0.022 ± 0.003
EryK	-0.57 ± 0.03	0.011 ± 0.002

Table 3.2: **parameters that have been obtained by exponential fit of time course for different samples.**

duction process.
From the observation of the rate constant k (Tab. 3.2) we observe that the photoreduction of Neuroglobin (that is an hexacoordinate system) is comparable with horse Myoglobin and EryK photoreduction (within the error) and only photoreduction speed of sperm whale Myoglobin seems to be ten time faster than the other hemeproteins analyzed.
Therefore the conclusion is that the speed of photoreduction is not connected with the redox function of the protein, but it is only caused by the radiation produced by third-generation synchrotron sources that produces high magnitude X-ray intensities that can cause radiation damage of crystalline biological samples.

3.3 Characterization of Ngb matrix

The role of Mb cavities in ligand dynamics has been extensively investigated (see Par. 1.3.2); since Ngb has a wide hydrophobic cavity and it also presents catalytic activity (Par. 1.2.3),

our interest has been focused in the investigation of the Ngb huge cavity, in order to describe the migration of small ligands (CO, O_2 and Xe) in the protein matrix, trying to shed light to the gaseous ligand scavenging, using different techniques: UV-Vis microspectrophotometry (off-line) to investigate absorption spectra of NgbCO crystals; XRD and XANES at low temperature to determine the structure of NgbCO and Ngb*CO, this last species obtained under illumination and long X-ray exposure respectively. Finally we determined at room temperature the structure of metNgb, under different gaseous pressures.

3.3.1 Characterization of NgbCO photolytic intermediates

Nienhaus and co-workers, by using infrared spectroscopy and nanosecond time-resolved visible spectroscopy, have investigated ligand-binding reaction over a wide temperature range (3 - 353 K) in NgbCO [34]. They have observed that photolysis at cryogenic temperature creates a five-coordinate deoxy species (Ngb*CO) with very low geminate-rebinding barriers; this state can be trapped only at temperatures lower than 40 K, since at higher temperatures geminate rebinding does not allow it to be populated. Therefore, we have characterized NgbCO crystals with the off-line microspectrophotometer (Par. 2.4.1.1) at low temperature, then we have determined the structure of NgbCO at 15 K, under visible illumination; finally, we have characterized the heme environment of NgbCO with XANES measurements in solution at T = 15 K, under long X-rays exposure.

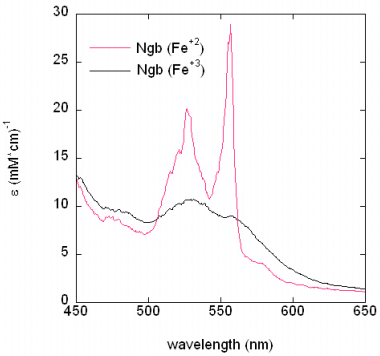

Fig. 3.3.1: **absorption spectra of Neuroglobin crystals at 15 K**. The black line corresponds to the ferric form and the purple line to the ferrous form of Ngb, that was obtained soaking crystals with the reducing agent Na dithionite.

3.3.1.1 UV-Vis microspectrophotometry on NgbCO crystal (off-line)

The first samples analyzed were Ngb crystals in the ferric and ferrous (reduced with Na dithionite) form and their absorption spectra are reported in Fig. 3.3.1. The absorption spectra of these two crystal forms have the typical aspect of met-Ngb and ferrous Ngb, observed in solution, respectively [10].
Fig. 3.3.2 shows absorption spectra of NgbCO crystals at two different values of temperature, 15 K and 30 K. As far as spec-

trophotometric measurements are concerned, the Ngb*CO should correspond to a deoxy pentacoordinated species (black line), which is very different from the deoxy hexacoordinated species shown in Fig. 3.3.1. Indeed Fig. 3.3.2 (a) shows a spectrum (black line) at 15 K that corresponds to a deoxy pentacoordinated state, which so far has never been observed for Ngb, indicating that even the lamp probe of the microspectrophotometer is sufficient to achieve full photolysis and consequently we were able to trap the Ngb*CO species at 15 K. Consistently, at temperatures higher than 30 K, geminate rebinding becomes dominant, leading to a spectrum (purple line) that corresponds to the NgbCO spectrum as reported in the literature [10]. In order to confirm that the spectrum reported in Fig. 3.3.2 (a) corresponds to Ngb*CO, we tested its reversibility, by cycling the temperature from 15 K to 30 K and vice-versa. The transition from photolytic intermediate Ngb*CO at 15 K to Ngb CO-bound at 30 K was clearly followed, with full reversibility, after several cycles (Fig. 3.3.2 b).
This experimental session has been very successful, since we have obtained the data we were aiming to: spectra of different species of Ngb in crystals (Fig. 3.3.1, 3.3.2) and isolation and characterization of the temperature stability of the Ngb*CO photolytic intermediate (Fig. 3.3.2). The optical spectra of Ngb, always correspond to an hexacoordinated form, since in the absence of a gaseous ligand such as CO, O_2 or NO the proximal histidine occupies the sixth coordination position. For the first time a pentacoordinated state of Ngb has been trapped in the crystal (the Ngb*CO species). This result is interesting *per se* and demonstrates the feasibility of the determination of the 3D

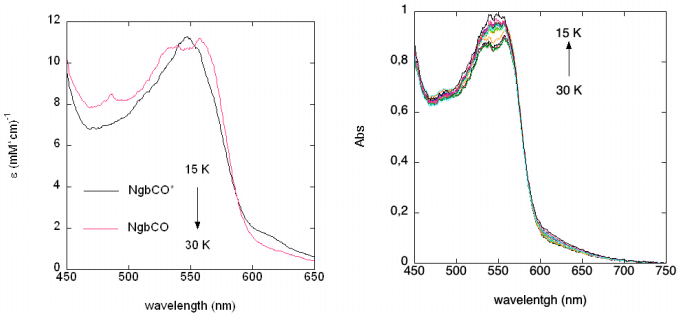

(a) (b)

Fig. 3.3.2: **absorption spectra of NgbCO crystals**.
(a) At low temperature (15 K) is possible to trap photolytic intermediate Ngb*CO (black line) under illumination of the probing lamp of the microspectrophotometer. Increasing the temperature to 30 K is sufficient to obtain the CO bound species (purple line). **(b)** NgbCO absorption spectra collected lowering the temperature from 30 K to 15 K. There is a transition from Ngb CO-bound species to the photolytic intermediate Ngb*CO. The process is completely reversible.

structure of this photolytic intermediate.

3.3.1.2 Structure of photolytic intermediate Ngb*CO at low temperature

From UV-Vis microspectophotometry on NgbCO crystals (see Par.
3.3.1.1) we have the proof that, at a temperature about 15 K, it is possible to trap the photolytic intermediate Ngb*CO, breaking the Fe-iron bond by visible illumination, so we carried out XRD data collection at low temperature, under illumination. The diffraction and refinement data sets are reported in Tab. 3.3. The refinements of the electron density maps of one of the data set collected, are shown in Fig. 3.3.3. In the 'dark' structure (Fig. 3.3.3 a) the occupancy of CO is 90 %, while in the 'light on' structure (Fig. 3.3.3 b) it is 40 %, as estimated by model refinement. The most interesting feature we have obtained is the absence of electron density between CO and the heme iron further refinement confirmed that CO is positioned at distance longer than bond length distance, indicating that this ligand, at 15 K, had been photodissociated and docked, in the vicinity of the heme iron, in the heme distal pocket (relevant distances are reported in Tab. 3.4). In Fig. 3.3.4 the conformer of the heme in Ngb*CO is shown; the photodissociated CO lies on top of the heme pyrrol ring C, in the 'primary docking site' and the distance of Fe-*CO is about 2.7 Å, while in the NgbCO form, the distance between iron-heme and CO is 1.9 Å. This result is in agreement with Nienhaus and co-workers who have investigated the Ngb matrix by FTIR spectroscopy in the infrared stretching

Carbonmonoxy Neuroglobin	dark (40 K)	light (15 K)
Diffraction data		
Wavelength Å	0.93	0.93
Space group	R32	R32
a b, Å	88.06	88.04
c, Å	110.16	110.16
Resolution range, Å	44.63-2.0 (2.1-2.0)	44.63-1.9 (2.0-1.9)
I/Sigma	27.2 (7.5)	16.9 (3.0)
Unique reflections	11287 (1614)	12847 (1878)
Completeness, %	99.9 (100.0)	98.5 (99.9)
Redundancy	7.1 (7.2)	3.7 (3.6)
Rmerge	0.053 (0.236)	0.055 (0.373)
Refinement		
Resolution range, Å	36.04 -2.0	36.03-1.90
Rcryst	0.17	0.17
Rfree	0.22	0.21
No. of protein atoms	1661	1689
No. of Heme/ligands atom	41/13	41/13
No. of water molecules	117	110
rms deviation from ideality		
Bonds, Å	0.14	0.011
Angles, °	1.42	1.27
Average B value, Å	24.82	26.84

Table 3.3: **crystallographic data collection and refinement statistics of NgbCO crystal**.
The data were acquired without illumination at 40 K (dark) and under continuous illumination with a optical fiber microscope lamp at 15 K (light).

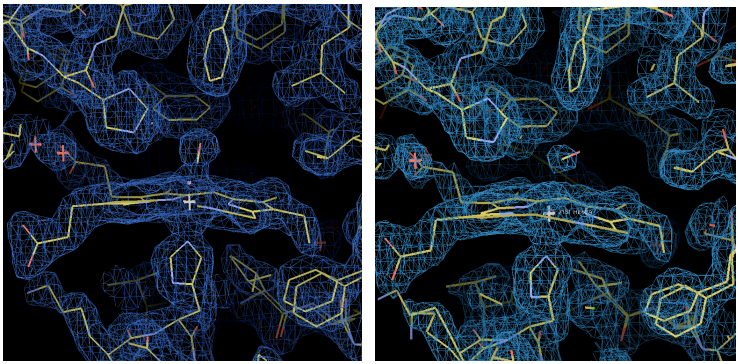

(a) (b)

Fig. 3.3.3: **electron density map of NgbCO.**
(a) Electron density map of NgbCO crystal at 40 K without illumination. The CO occupancy is 90 % (contour: 1 σ). **(b)** Electron density map of NgbCO crystal under illumination at 15 K. The CO occupancy is 40 % (contour: 1 σ).

neighbor amino acid	CO-distance (Å) C/O	*CO-distance (Å) C/O
V68-Cγ2	3.65/3.78	3.34/4.40
H64-Cε1	3.69/3.12	3.91/3.45
F28-Cζ	4.11/3.20	3.34/3.20
F42-Cζ	4.94/4.10	4.79/4.20

Table 3.4: **distances between CO atoms and protein atoms.**
In the second column we report the distance between CO and its neighbor protein atoms of the 'dark' form, while in the third column the distance between the photolyzed CO and its neighbor protein atoms. We list only distances < 5.0 Å.

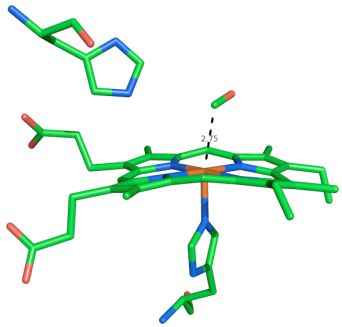

Fig. 3.3.4: **conformer of the heme in Ngb*CO.**
Ngb*CO: the distance of Fe-*CO is about 2.7 Å.

bands of CO and flash photolysis at cryogenic temperature and have observed ligand migration to the 'primary docking site' [70].

3.3.1.3 XANES spectra on NgbCO in solution

XANES spectra on NgbCO in solution under long X-ray exposure were also collected to investigate the photolytic intermediate with an independent technique in solution.
XANES spectra at the Fe K-edge were measured and a comparison between solution samples of NgbCO and its photoproduct has been carried out. Fig. 3.3.5 (a) shows the spectral evolution observed for NgbCO under prolonged X-ray irradiation of the sample at 15 K. This process is slow enough to be follow in the time window (minutes to hours) of the XANES experiment.

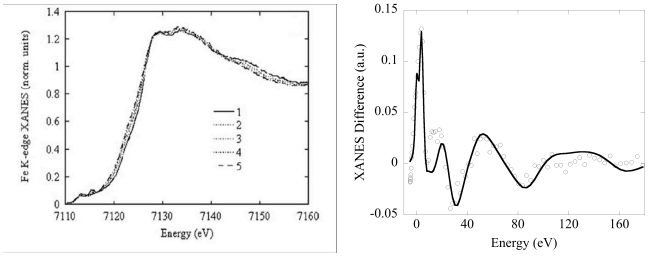

(a) (b)

Fig. 3.3.5: **XANES of NgbCO in solution.**
(a) Evolution with time of the XANES spectrum of NgbCO under prolonged X-ray exposure. Examining the spectra in the region peaked around 7145 eV, from top (solid line) to bottom (dashed line), the starting time acquisition are: 0 min, 45 min, 3h :16 min, 4 h:04 min, 4 h:45 min. **(b)** Theoretical XANES fit (solid line) of the experimental difference spectrum obtained by subtracting the first from the last spectrum (open circles).

The existence of at least three isosbestic points (at 7117, 7128 and 7142 eV) indicates that this process corresponds to a two state transition. Fig. 3.3.5 (b) shows the difference spectrum (open circles) obtained by subtracting the first spectrum from the last one and theoretical XANES fit (solid line) obtained with MXAN package [93]. The data show that for NgbCO the final state is a five-coordinate Fe-heme, providing evidence that the Fe-CO bond was broken. CO rebinding was observed by increasing temperature at T > 70 K, demonstrating that this process is reversible (as seen in Par. 3.3.1.1).

The structural parameters extracted by the quantitative anal-

experiment	Fe-heme Disp. (Å)	Fe-Np (Å)	Fe-His (Å)	Fe-CO (Å)
XRD 2.0 Å$^{a}_{\text{NgbCO}}$	-	2.04 (15)	1.92 (15)	1.90 (26)
XANES (solution)$^{b,c}_{\text{NgbCO}}$	0.04 (fixed)	2.02 (2)	1.96 (7)	1.86 (5)
XRD 1.9 Å$^{a}_{\text{Ngb*CO}}$	-	2.06 (30)	2.09 (32)	2.75 (26)
XANES (solution)$^{b}_{\text{Ngb*CO}}$	0.3 (2)	2.05 (1)	1.97 (1)	3.44 (8)
XRD 1.5 Å$^{a}_{\text{Mb*CO}}$ [116]	0.2	1.97	2.25	3.60
XANES (solution)$^{b}_{\text{Mb*CO}}$[96]	0.40 (5)	2.04 (2)	2.07 (3)	3.23 (10)

Table 3.5: **Ngb*CO structural determination by XAS.** [a]Estimated standard uncertainties are calculated by using $\text{DPI}_{\text{Rfree}}$.[105][b]Numbers in parentheses represent the statistical error of the last digits. [c]Data discussed in Par. 3.1.

ysis are listed in Tab. 3.5, in which we report the comparison between data of MbCO and NgbCO and their photoproducts respectively obtained with two different techniques: XANES (sample in solution) and XRD (single crystal).
In summary, from XANES analysis, for Ngb*CO we have obtained: (i) a Fe-heme displacement of 0.3 (2) Å, similar to Fe-heme displacement of Mb*CO; (ii) distance between iron and N_{pyrrol} of 2.05 (1) Å, in good agreement, within statistical error, with values of the other species; (iii) distance between iron-heme and histidine 96 of 1.97 (1) Å that is always underestimated because of systematic error in the XANES analysis but it remains substantially the same with respect to the value obtained for NgbCO (1.96 Å); moreover the distance between iron-heme and photolyzed CO is 3.44 (8) Å, similar to Fe-*CO distance in Mb*CO (from both XRD and XANES measurements), not in full agreement with the Fe-*CO distance that we have observed by XRD in Ngb*CO (2.75 Å). The most likely reason of this disagreement is that by XRD at low temperature we have

achieved partial photolysis of NgbCO, so due to the complexity of the electron density map obtained, our estimate of the distance Fe-*CO is less accurate; XANES analysis is made on difference spectra, so it is possible to isolate the pentacoordinated species to obtain a more accurate determination of the Fe-*CO distance.
Therefore, by XRD at 15 K, under visible illumination, we have determined structural parameters relative to the photolytic intermediate of Ngb (see Fig. 3.3.3). We have indication, from the distance between photolyzed CO and heme iron (also in comparison with Mb values and XANES values in Ngb) and from the partial occupancy of CO itself (40%) that the extent of photolysis is about 50%. This percentage of photolysis indicates that, if the protocol is improved by accumulating the photoproduct upon illumination prior to data collection we might be able to collect a complete photolyzed, high quality data set; in fact we have have planned to repeat this experiment, following the strategy mentioned above.

3.3.2 Structure of Ngb at room temperature under different gaseous pressures

The localization of small gaseous ligands such as CO and O_2 in the protein matrix in proteins is a non trivial experimental task and it is often inferred through indirect methods such as the usage of xenon or halide anions as probes. In this study a straightforward method based on X-ray crystallography under high pressure of pure gas was applied, using CO, O_2 and Xe. Our goal was to visualize entrance and exit pathways within

the protein and the presence of docking sites for small diatomic ligands, trying to shed light on structural parameters governing affinity and reactivity in Ngb. We wish to underline that only data collection at room temperature offers the possibility to control gas pressure with accuracy and to vary this parameter during the experiment. Moreover we could obtain native and gas derivatized data from a single crystal, allowing the sample to equilibrate after increasing the gas pressure. During these experiments the protein was experiencing its dynamics which is accessible only above the glass transition temperature, allowing to observe docking sites in conditions that are more representative of the physiological environment. The main *caveat* in this experimental setup is the enhancement of radiation damage with respect to the current methodology of cryo-cooling at 100 K. We have therefore used the experimental station BM30 at ESRF, because of its attenuated intensity due to the usage of a bending magnet, and we have carefully checked data quality using the standard crystallographic evaluation parameters as shown in Tab. 3.6, 3.8 and 3.9. Indeed high quality data could be collected, indicating a remarkable resistance of Ngb crystals to radiation damage; moreover the size of the samples allowed to collect multiple data set from a single crystal by illuminating with X-rays different regions.

3.3.2.1 XRD at room temperature: different pressures of Xe

Xenon is often used as a probe for dioxygen-binding sites [117], and from a crystallographic study at 100 K, (see Par. 1.3.1), it

was observed that Ngb is endowed with four Xe binding sites. In this context we have investigated the Ngb protein matrix under Xe pressure at room temperature, as a control of this new X-ray crystallographic approach. The strategies for preparing isomorphous noble gas (Xe) derivative differ, depending on whether X-ray data are collected at room temperature or on flash-frozen crystals. At room temperature, because the process of xenon binding is completely reversible, the gas pressure must be maintained and can be controlled throughout the data collection. On the other hand, once pressurized crystals are frozen at cryogenic temperatures, the gas atoms are trapped within binding sites so that data collection can proceed in the standard way, without the need to maintain gas pressure.
We determined the crystal structure of metNgb derivatized with Xe (17 bar) at 1.8 Å resolution at room temperature, and the analysis of our data set is shown in Tab. 3.6. Electron density maps show the presence of four Xe atoms in metNgb. The XeI atom is on the external Ngb surface at the interface between two symmetry-related molecules, in a small breach accessible to the solvent; this site hosts two alternative positions for XeI, each with partial occupancy.
The distance between XeII and the heme iron is 13.59 Å. Xe atoms in positions III and IV are hosted in two adjacent hydrophobic niches located inside the large internal cavity; the XeIII docking site is an apolar pocket close to the EF corner, at the entrance to the tunnel that connects the heme iron with the bulk. The distance between XeIII and the heme vinyl of pyrrole C is 6.52 Å. This pocket displays the highest occupancy for Xe (55 %, see Tab. 3.7). XeIV is the closest to the iron and

Neuroglobin	Xe 17 bar
Diffraction data	
Wavelength Å	0.98
Space group	R32
a b, Å	89.05
c, Å	114.96
Resolution range, Å	50.00-1.80 (1.86-1.80)
Unique reflections	16496
I/Sigma	44.33 (4.86)
Completeness, %	100.0 (99.8)
Redundancy	7.3 (6.1)
Rmerge	0.034 (0.304)
Refinement	
Resolution range, Å	19.75-1.80
Rfact	0.18
Rfree	0.21
No. of protein atoms	1196
No. of Heme/sulfate ion atoms	41/5
No. of Xe atoms	5
No. of water molecules	37
rms deviation from ideality	
Bonds, Å	0.02
Angles, °	1.44
Average B value, Å	28.30

Table 3.6: **crystallographic data collection and refinement statistics.**
Ngb under 17 bar of Xe, at room temperature.

Xe site (17 bar)	occupancy (%)	neighbor amino acid	distance (Å)
XeI a/b	15/15	K67-Cε	3.70/3.78
XeII	40	T25-CO	4.66
		F28-Cβ	4.28
		F32-Cδ2	3.76
		P52-Cβ	4.10
		S55-Oγ	3.38
		L56-Cδ2	3.49
		F61-Cε2	4.34
XeIII	55	I72-Cγ1	4.24
		A75-Cβ	4.46
		L113-Cδ2	4.40
		W133-Cζ3	4.18
		Y137-Cδ1	4.11
		V140-Cγ21	4.04
XeIV	15	L27-Cδ1	4.20
		V68-Cγ1	4.13
		I72-Cδ1	3.46
		V109-Cγ1	3.71
		L113-Cδ2	4.26
		Y137-Cε1	3.91

Table 3.7: **distances between noble gas atoms and proteins atoms.** We list only distances < 5.0 Å; a/b refers to the presence of double conformations.

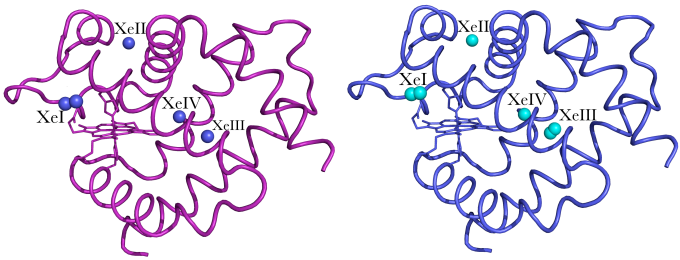

(a) (b)

Fig. 3.3.6: **structure of NgbXe.**
(a) NgbXe at 300 K, under 17 bar of Xe. **(b)** NgbXe at 100 K, under 20 bar of Xe [66].

is located in the distal branch of the large cavity, between XeIII and the heme. After refinement, the XeIV occupancy was only 15%.
In Tab. 3.7 we report distances between Xe atoms and its neighboring protein atoms, shorter than 5 Å.
From analysis of our data set we have observed the same Xe binding sites at cryogenic temperature, reported by Moschetti *et al.* [66] (see Par. 1.3.1), as shown in Fig. 3.3.6, in which we compare our NgbXe structure (Fig. 3.3.6 a) and NgbXe structure at 100 K (Fig. 3.3.6 b). The differences are only in the occupancy of Xe atoms, moreover we have observed only one conformation for XeIII, instead of two, as reported by Moschetti *et al.* [66].
Therefore we have the evidence that XRD at room temperature

is a reliable technique to investigate the structure of proteins under gaseous at physiological temperature.

3.3.2.2 XRD at room temperature: different pressures of O_2

We also collected data diffraction of Ngb in the native form and under 10 and 20 bar of oxygen pressure. The crystallographic data collection and refinement statistics are shown in Tab. 3.8.

Upon refinement of diffraction data from Ngb crystals at 10 and 20 bar of O_2, we observe the appearance of a docked dioxygen molecule in a hydrophobic niche, at 100 % and 75 % occupancy, respectively (Fig. 3.3.7). This cavity corresponds to the site XeIII and, in the absence of pressurized gases, it is empty in all Ngb structures determined so far. Moreover, a site that normally hosts a water molecule (Wat9, [25]), positioned distally to the heme, seems to contains a O_2 molecule when Ngb crystals are exposed to 10 and 20 bar of O_2 pressure (respectively 50 % and 70 % occupancy, Fig. 3.3.8).
In summary, from these measurements we found two sites for dioxygen, one, that corresponds to XeIII binding site, is unambiguous, because it is empty before exposure at different oxygen pressure; the second one, that corresponds to Wat9 site, needs a rigorous analysis in the electron peak content, especially at low oxygen occupancy.

Neuroglobin	Native	O_2 10 bar	O_2 20 bar
Diffraction data			
Wavelength Å	0.98	0.98	0.98
Space group	R32	R32	R32
a b, Å	89.02	89.07	89.06
c, Å	115.37	115.12	115.13
Resolution range, Å	50.00-1.65 (1.71-1.65)	50.00-1.66 (1.72-1.66)	50.00-1.75 (1.81-1.75)
Unique reflections	21385	20972	17952
I/Sigma	35.3 (5.4)	32.7 (3.6)	36.7 (6.5)
Completeness, %	98.3 (93.7)	98.2 (94.1)	98.2 (94.0)
Redundancy	7.4 (7.4)	7.4 (7.0)	7.5 (7.4)
Rmerge	0.050 (0.382)	0.048 (0.432)	0.051 (0.426)
Refinement			
Resolution range, Å	36.56-1.65	32.04-1.80	32.04-1.75
Rfact	0.16	0.15	0.15
Rfree	0.20	0.20	0.20
No. of protein atoms	1871	1937	1945
No. of Heme/sulfate ion atoms	84/30	84/8	84/10
No. of O_2atoms	0	4	10
No. of water molecules	86	95	104
rms deviation from ideality			
Bonds, Å	0.012	0.015	0.014
Angles, °	1.49	1.55	1.57
Average B value, Å	23.70	24.40	25.35

Table 3.8: **crystallographic data collection and refinement statistics.**
Ngb in the native state and under 10 and 20 bar of O_2, at room temperature.

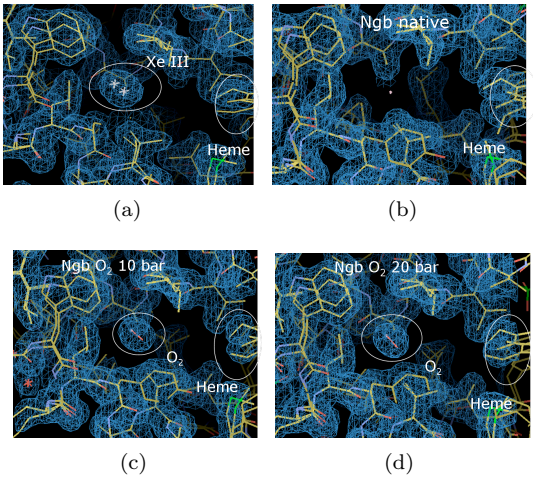

Fig. 3.3.7: **electron density maps of Ngb XeIII binding site at room temperature at different pressure of O_2.**
(a) XeIII binding site of Ngb under Xe pressure; **(b)** XeIII binding site of Ngb under 0 bar of O_2; **(c)** O_2at 100 % of occupancy, in the XeIII binding site of Ngb under 10 bar of O_2; **(d)** O_2 at 75 % of occupancy, in the XeIII binding site of Ngb under 20 bar of O_2.

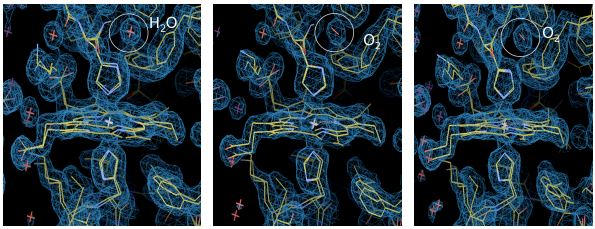

(a) (b) (c)

Fig. 3.3.8: **electron density maps of Ngb Wat9 site at room temperature at different pressure of O_2.**
(a) Wat9 site in Ngb**; (b)** Wat9 site of Ngb is occupied to an oxygen at 50 % of occupancy, under 10 bar of O_2; **(c)** Wat9 site of Ngb is occupied to an oxygen at 70 % of occupancy, under 20 bar of O_2.

3.3.2.3 XRD at room temperature: different pressures of CO

To have a complete picture of Ngb matrix ligand affinity and pathway, we also collected data diffraction under CO at different pressures: 5, 20, 30 and 40 bar. The crystallographic data collection and refinement statistics are shown in Tab. 3.9.
From refinement of all data sets at different pressures we could not detect CO molecules in the electron density maps, even at the highest pressure tested (*i.d.* 40 bar).

Neuroglobin	CO 5 bar	CO 20 bar	CO 30 bar	CO 40 bar
Diffraction data				
Wavelength Å	0.98	0.98	0.98	0.98
Space group	R32	R32	R32	R32
a b, Å	89.11	89..13	89.15	89.20
c, Å	114.36	114.28	114.35	114.32
Resolution range, Å	50.00-1.90 (1.97-1.90)	50.00-1.80 (1.86-1.80)	50.00-1.76 (1.82-1.76)	50.00-1.85 (1.92-1.85)
Unique reflections	13999	16432	17582	15180
I/Sigma	26.4 (5.1)	28.2 (4.8)	31.4 (5.3)	29.5 (3.9)
Completeness, %	99.9 (100.0)	99.9 (100.0)	99.9 (100.0)	99.9 (100.0)
Redundancy	7.3 (7.4)	7.4 (7.4)	7.3 (7.0)	7.3 (7.4)
Rmerge	0.056 (0.427)	0.056 (0.461)	0.058 (0.340)	0.052 (0.446)
Refinement				
Resolution range, Å	38.132-1.90	38.10-1.80	38.12-1.90	32.01-1.85
Rfact	0.17	0.17	0.17	0.18
Rfree	0.22	0.21	0.21	0.22
No. of protein atoms	1723	1706	1712	1683
No. of Heme	84	84	84	84
No. of CO atoms	/	/	/	/
No. of water molecules	72	70	68	63
rms deviation from ideality				
Bonds, Å	0.014	0.013	0.009	0.012
Angles, °	1.52	1.42	1.18	1.19
Average B value, Å	25.70	26.00	24.70	27.77

Table 3.9: **crystallographic data collection and refinement statistics.**
Ngb under 5, 20, 30 and 40 bar of CO at room temperature.

Chapter 4

Conclusions and perspectives

4.1 General aims of the work

Ngb, together with Cygb, is a recently discovered hemeprotein belonging to the globin family and expressed in vertebrates brain [6, 22, 21]. Since its discovery in 2000, Ngb has been extensively studied by different approaches, which range from cellular biology to biophysics. In spite of this, its *in vivo* function remains elusive.

During the last years, the debate concerning Ngb function led to different hypotheses grouped into the following categories: (i) oxygen delivery, (ii) hypoxia signalling and (iii) radical scaveng-

ing [11].
It was shown that oxy-Ngb efficiently reacts with NO yielding NO^{3-} and metNgb [43], a reaction that may represent a system for sensing the relative concentration of O_2 and NO during hypoxia and, at the same time, for NO scavenging. By studying the reaction of Ngb with nitrite and peroxynitrite [12, 45], other authors suggested that Ngb may promote cell survival under hypoxic stress. Therefore it is possible to hypothesize that the scavenging activity of Ngb, and its interaction with O_2, NO and related species, in conjunction with structural transition revealed by crystallography, could contribute to a hypoxia-signalling pathway and/or protect the cell from radical stress under hypoxic conditions.
The aim of this work was to study the structural properties that regulate the interaction of Ngb with its ligands, trying to shed light on ligand pathways and docking sites that might dictate reactivity, using different biophysical approaches.
We characterized, with high accuracy, the heme structural parameters of NgbCO in solution by XAS and compared them with those arising from the NgbCO crystal structure; we carried out a comparative study of Ngb with three different hemeproteins (SWMb, HMb and EryK P450), to determine the rate of heme-iron photoreduction and its correlation with protein function. Finally we investigated the protein matrix both at cryogenic and room temperature, in order to describe pathways of ligand from or toward the heme-iron.

4.2 X-ray Absorption Spectroscopy and the Ngb heme environment

The investigation of heme-iron environment by X-ray Absorption Spectroscopy (XAS) allowed us to demonstrate that the structure of NgbCO, as far as the close vicinity of the heme is concerned, is identical in solution and in the crystal form. This comparison was required since Ngb crystals tend to crack upon CO binding suggesting the presence of incomplete structural transition and MD simulations predict in solution a structure of the active site different from the one found in NgbCO crystals [60, 104].
The results obtained by XAS during this work, indicate that, as far as the heme and ligand geometry are concerned, data do not differ between NgbCO in solution and in the crystal and both are consistent with XRD parameters.
This finding supports the relevance of the heme sliding mechanism discovered on the NgbCO structure and the use of crystallographic data for rationalizing Ngb functional data.

4.3 Redox state of hemeprotein crystals

Characterization of the reduction kinetics in hexacoordinated Hbs (hxHbs), including human Ngb [42], showed that in these proteins electron transfer is much faster than in pentacoordinated hemeproteins. This behaviour has been explained on the

basis of the more favourable reorganization energy term involved in the reduction of hexacoordinated hemeproteins, supporting the hypothesis that hxHbs may be tuned for redox cycling rather than binding.
Given this consideration and the fact that Ngb undergoes reduction upon X-ray irradiation [87], we performed a comparative study between Ngb and other hemeproteins.
From UV-Vis absorption microspectrophotometry we have shown that, in low temperature crystallographic studies, the heme-iron photoreduction within the first few seconds upon X-ray exposure is not a peculiarity of Ngb, but it is a phenomenon observed for all systems analyzed in the present work (Ngb, SWMb, HMb and EryK). Therefore we may conclude that photoreduction by X-rays is not correlated with redox properties, but it takes place regardless of the heme protein function.
We wish to point out this event has to be taken into account in crystallographic studies carried out at third-generation synchrotron sources and could also constitute an useful tool to feed electrons within heme redox centres, in order to perform functional studies within crystals [118].

4.4 The Ngb internal 'tunnel': partial conservation and potential role

The structure of Ngb differs from that of Mb for three peculiarities, which are uncommon for a vertebrate globin: (i) the ferric and ferrous heme-iron are both hexacoordinate, with the

distal His(E7) and the proximal His(F8) directly bound to the metal; (ii) a wide branched cavity ($\sim$ 300 $\AA^3$), referred to as a 'tunnel', connecting the heme pocket with the solvent is present in the core structure; (iii) ligand binding to ferrous Ngb is associated to a conformational change involving a sliding motion of the heme and a moderate shift in the position of helix F and loops CD and EF [55].
In analogy with the internal packing defects characteristic of Mb, this 'tunnel' implies an offset in terms of thermodynamic stability. In Mb the presence of cavities plays a functional role by regulating the dynamics of ligand binding [64, 65], counterbalancing the destabilization due to imperfect packing.
It has been proposed that the Ngb 'tunnel' may represent an amplification of the set of Mb internal cavities and that it plays also a functional role. This hypothesis was supported by MD simulations showing the similarity between the Ngb 'tunnel' and the Mb Xe sites [60], since during simulations they both host ligands and constitute a preferential pathway for migration within the protein. Our data provide experimental evidence of ligand docking within the Ngb 'tunnel', as shown in Fig. 4.4.1, which shows the sites in which we observed a gas molecule hosted in the Ngb matrix. Indeed, in O_2 pressurized crystals at room temperature, we observed an oxygen molecule in the XeIII binding site and in the Wat9 site. Moreover, the experiments carried out on NgbCO at 15 K, allowed us to identify, both in solution and in the crystal, the 'primary docking site' for photolyzed CO at about 3 $\AA$ from the heme-iron. Therefore we can define a possible pathway of the ligand into the protein matrix from or

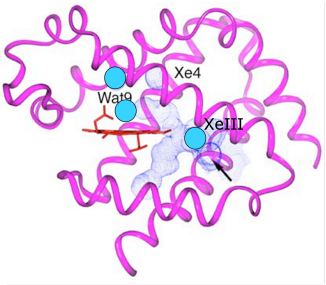

Fig. 4.4.1: **gaseous ligand sites in Ngb matrix.**
Three sites (cyan circles) of the Ngb matrix, in which we found a gas molecule. An oxygen molecule has occupied the XeIII binding site and the Wat9 site, while the CO photolyzed has occupied 'primary docking site', at about 2.7 Å distant to the heme-iron.

toward the heme-iron: the most peripheral position is the XeIII site; the Wat9 site lies buried within the protein and, at only $\sim$ 3 Å from the heme, we identified a 'primary docking site'; Fig. 4.4.1 shows, with cyan circles, these positions with respect to the Ngb 'tunnel'.

In conclusion the ligand pathway in Ngb seems confined to the distal heme site, at variance with the case of Mb where cavities proximal to the heme play a role in ligand dynamics (see Par. 1.3.2, 1.3.3).

We attribute this feature to endogenous heme hexacoordination, which requires a more efficient access to the binding site in order to compensate for the competition for the heme-iron between the ligand and the distal histidine. Therefore, although

the proximal cavity is necessary for allowing heme sliding and population of the pentacoordinated state competent for binding, it is not accessed by ligands on the pathway to the binding site. An intriguing finding is the absence of CO in docking sites such as XeIII and Wat9, that are populated by oxygen at comparable gas pressures.

We may speculate that the protein matrix favors O_2 binding by discriminating against CO. This could be an additional feature, introduced at the level of the protein matrix, to favor the physiological ligand and counterbalance the intrinsic high affinity of the heme-iron for CO.

We are currently testing this hypothesis by carrying out the identification of docking sites of CO and O_2 in sperm whale Myoglobin and other hemeproteins, such as EryK P450, Hemoglobin and Ngb mutants.

Another development of this work has been setting up the beamline instrumentation in collaboration with ESRF, that allowed the determination of Ngb*CO photoproduct structure at 15 K. This is a unique instrumentation which we are currently utilizing for cryotrapping of EryK P450 reaction intermediates, as well as for studies on Ngb mutants.

Chapter 5

Aknowledgements

The experimental work presented in this thesis was carried on at the Department of Biochemical Sciences 'A. Rossi-Fanelli' of University of Rome 'Sapienza'. I am particularly grateful to Prof. Maurizio Brunori who gave me the possibility to work in his group and to benefit of his invaluable suggestions.
I am very grateful to Prof. Beatrice Vallone, for helping and advising me in all my experimental activities, for the daily supervision of my work, for the continuous fundamental support she gave me every day in many ways.
I wish to express my gratitude and my affection to Dr. Linda Savino, who introduced me in the fascinating world of X-ray crystallography, transmitting me her passion about that; I really thank her for teaching me basics of XRD and for her patience during map refinements.

Many thanks go also to the members of my lab: Tommaso Moschetti (now working at the Biochemistry Department, Cambridge University) who introduced me in this group and more in general to structural biology, Giovanna Avella and Linda Celeste Montemiglio who supported me during some experiments and also shared with me bad and good moments at the synchrotron facilities.
Thanks to the other members of the Protein Crystallography Group of Rome who helped me during my first crystallographic experiments and gave me important suggestions and tricks.
XAS experiments were carried out in collaboration with Prof. Alessandro Arcovito (Institute for Biochemistry and Clinical Biochemistry, Università Cattolica del Sacro Cuore, Rome) and Dr. Stefano Della Longa (Department of Experimental Medicine, University of L'Aquila). I would like to thank them who helped me and gave me several suggestions during these years.
UV-Vis microspectrophotometry experiments were done at European Synchrotron Radiation Facility (ESRF), in collaboration with Dominique Bourgeois and Martin Weik; I will be always obliged to them for the fulfilling experience they offered to me. Moreover, I would really like to thank Dr. Peter Van Der Linden for his fundamental technical support.
XRD at room temperature were carried out at ESRF in collaboration with Prof. Thierry Prangé (Department of Pharmacy, Université Paris Descartes-CNRS), Dr. Nathalie Colloc'h and Dr. Guillaume Marrassio (Centre CYCERON, Université de Caen-CNRS); I really thank them for these interesting experiments.
More in general, I would like to express all my affection and my

gratitude to each of my colleagues in the Department of Biochemical Sciences, who always kindly collaborated and showed to me great friendship.
Finally, I need to express my sincere gratitude to Fabio for his basic LaTeX advices, allowing the drawing up of this work.

Bibliography

[1] S.N. Vinogradov and L. Moens. Diversity of globin function: enzymatic, transport, storage, and sensing. *J. Biol. Chem.*, 283:8773–8777, 2008.

[2] R.C. Hardison. A brief history of hemoglobins: plant, animal, protist and bacteria. *Proc. Natl. Acad. Sci. USA*, 93:5675–5679, 1996.

[3] R.C. Hardison. Hemoglobins from bacteria to man: evolution of different patterns of gene expression. *J. Exp. Biol.*, 201, 1998.

[4] D. Kugelstadt, M. Haberkamp, T. Hankeln, and T. Burmester. Neuroglobin, cytoglobin, and a novel, eye-specific globin from chicken. *Biochem. Biophys. Res. Commun.*, 325:719–725, 2004.

[5] A. Roesner, C. Fuchs, T. Hankeln, and T. Burmester. A globin gene of ancient evolutionary origin in lower verte-

brates: evidence for two distinct globin families in animals. *Mol. Biol. Evol.*, 22:12–20, 2005.

[6] T. Burmester, B. Weich, S. Reinhardt, and T. Hankeln. A vertebrate globin expressed in the brain. *Nature*, 407:520–523, 2000.

[7] T. Burmester and T. Hankeln. Neuroglobin: a respiratory protein of the nervous system. *News Physiol. Sci.*, 19:110–113, 2004.

[8] Y. Sun, K. Jin, X.O. Mao, Y. Zhu, and D.A. Greenberg. Neuroglobin is up-regulated by and protects neurons from hypoxic-ischemic injury. *Proc. Natl. Acad. Sci. USA*, 98:15306–15311, 2001.

[9] Y. Sun, K. Jin, A. Peel, X.O. Mao, and D.A. Greenberg. Neuroglobin protects the brain from experimental stroke in vivo. *Proc. Natl. Acad. Sci. USA*, 100:3497–3500, 2003.

[10] S. Dewilde, L. Kiger, T. Burmester, T. Hankeln, V. Baudin-Creuza, T. Aerts, M. C. Marden, R. Caubergs, and L. Moens. Biochemical characterization and ligand binding properties of neuroglobin, a novel member of the globin family. *J. Biol. Chem.*, 276:38949–38955, 2001.

[11] M. Brunori and B. Vallone. Neuroglobin, seven years after. *Cell. Mol. Life Sci.*, 64:1259–1268, 2007.

[12] M.G. Petersen, S. Dewilde, and A. Fago. Reactions of ferrous neuroglobin and cytoglobin with nitrite under anaerobic conditions. *J. Inorg. Biochem.*, 102:1777–1782, 2008.

[13] K. Wakasugi, T. Nakano, and I. Morishima. Oxidized human neuroglobin acts as a heterotrimeric galpha protein guanine nucleotide dissociation inhibitor. *J. Biol. Chem.*, 278:36505–36512, 2003.

[14] C. Lechauve, H. Rezaei, C. Celier, L. Kiger, M. Corral-Debrinski, S. Noinville, C. Chauvierre, D. Hamdane, C. Pato, and M.C. Marden. Neuroglobin and prion cellular localization: investigation of a potential interaction. *J. Mol. Biol.*, 388:968–977, 2009.

[15] A. Fago, A.J Mathews, L. Moens, S. Dewilde, and T. Brittain. The reaction of neuroglobin with potential redox protein partners cytochrome b5 and cytochrome c. *FEBS Lett.*, 580:4884–4888, 2006.

[16] T.A.K. Freitas, S. Hou, E.M. Dioum, J.A. Saito, J. Newhouse, G. Gonzalez, M.A. Gilles-Gonzalez, and M. Alam. Ancestral hemoglobins in archaea. *Proc. Natl. Acad. Sci. USA*, 101:6675–6680, 2004.

[17] D.M. Minning, A.J. Gow, J. Bonaventura, R. Braun, M. Dewhirst, D.E. Goldberg, and J.S. Stamler. Ascaris haemoglobin is a nitric oxide-activated 'deoxygenase'. *Nature*, 401:497–502, 1999.

[18] R.K. Poole and M.N. Hughes. New functions for the ancient globin family: bacterial responses to nitric oxide and nitrosative stress. *Mol. Microbiol.*, 36:775–783, 2000.

[19] J.R. Pawloski, D.T. Hess, and J.S. Stamler. Export by red blood cells of nitric oxide bioactivity. *Nature*, 409:622–626, 2001.

[20] M. Brunori. Nitric oxide moves myoglobin centre stage. *Trends Biochem. Sci.*, 26:209–210, 2001.

[21] J.T. Trent and M.S. Hargrove. A ubiquitously expressed human hexacoordinate hemoglobin. *J. Biol. Chem.*, 277:19538–19545, 2002.

[22] T. Burmester, B. Ebner, B. Weich, and T. Hankeln. Cytoglobin: a novel globin type ubiquitously expressed in vertebrate tissues. *Mol. Biol. Evol.*, 19:416–421, 2002.

[23] T. Burmester, M. Haberkamp, S. Mitz, A. Roesner, M. Schmidt, B. Ebner, F. Gerlach, C. Fuchs, and T. Hankeln. Neuroglobin and cytoglobin: genes, proteins and evolution. *IUBMB Life*, 56:703–707, 2004.

[24] A. Pesce, S. Dewilde, M. Nardini, L. Moens, P. Ascenzi, T. Hankeln, T. Burmester, and M. Bolognesi. Human brain neuroglobin structure reveals a distinct mode of controlling oxygen affinity. *Structure*, 11:1087–1095, 2003.

[25] B. Vallone, K. Nienhaus, M. Brunori, and G.U. Nienhaus. The structure of murine neuroglobin: novel pathways for ligand migration and binding. *Proteins*, 56:85–92, 2004.

[26] M. Couture, T. Burmester, T. Hankeln, and D.L. Rousseau. The heme environment of mouse neuroglobin.

evidence for the presence of two conformations of the heme pocket. *J. Biol. Chem.*, 276:36377–36382, 2001.

[27] J.A. Hoy, S. Kundu, J.T. Trent, S. Ramaswamy, and M.S. Hargrove. The crystal structure of synechocystis hemoglobin with a covalent heme linkage. *J. Biol. Chem.*, 279:16535–16542, 2004.

[28] N.L. Scott, C.J. Falzone, D.A. Vuletich, J. Zhao, D.A. Bryant, and J.T.J. Lecomte. Truncated hemoglobin from the cyanobacterium synechococcus sp. pcc 7002: evidence for hexacoordination and covalent adduct formation in the ferric recombinant protein. *Biochemistry*, 41:6902–6910, 2002.

[29] M.S. Hargrove, E.A. Brucker, B. Stec, G. Sarath, R. Arredondo-Peter, R.V. Klucas, J.S. Olson, and G.N. Phillips. Crystal structure of a nonsymbiotic plant hemoglobin. *Structure*, 8:1005–1014, 2000.

[30] D. Hamdane, L. Kiger, S. Dewilde, B.N. Green, A. Pesce, J. Uzan, T. Burmester, T. Hankeln, M. Bolognesi, L. Moens, and M.C. Marden. The redox state of the cell regulates the ligand binding affinity of human neuroglobin and cytoglobin. *J. Biol. Chem.*, 278:51713–51721, 2003.

[31] A. Pesce, M. Bolognesi, A. Bocedi, P. Ascenzi, S. Dewilde, L. Moens, T. Hankeln, and T. Burmester. Neuroglobin and cytoglobin. fresh blood for the vertebrate globin family. *EMBO Rep.*, 3:1146–1151, 2002.

[32] B.J. Smagghe, G. Sarath, E. Ross, J.L. Hilbert, and M.S. Hargrove. Slow ligand binding kinetics dominate ferrous hexacoordinate hemoglobin reactivities and reveal differences between plants and other species. *Biochemistry*, 45:561–570, 2006.

[33] K. Nienhaus, J.M. Kriegl, and G.U. Nienhaus. Structural dynamics in the active site of murine neuroglobin and its effects on ligand binding. *J. Biol. Chem.*, 279:22944–22952, 2004.

[34] J.M. Kriegl, A.J. Bhattacharyya, K. Nienhaus, P. Deng, O. Minkow, and G.U. Nienhaus. Ligand binding and protein dynamics in neuroglobin. *Proc. Natl. Acad. Sci. USA*, 99:7992–7997, 2002.

[35] A. Pesce, D. De Sanctis, M. Nardini, S. Dewilde, L. Moens, T. Hankeln, T. Burmester, P. Ascenzi, and M. Bolognesi. Reversible hexa- to penta-coordination of the heme fe atom modulates ligand binding properties of neuroglobin and cytoglobin. *IUBMB Life*, 56:657–664, 2004.

[36] W. Du, R. Syvitski, S. Dewilde, L. Moens, and G.N. La Mar. Solution 1h nmr characterization of equilibrium heme orientational disorder with functional consequences in mouse neuroglobin. *J. Am. Chem. Soc.*, 125:8080–8081, 2003.

[37] A. Fago, C. Hundahl, S. Dewilde, K.Gilany, L. Moens, and R.E. Weber. Allosteric regulation and temperature dependence of oxygen binding in human neuroglobin and

cytoglobin. molecular mechanisms and physiological significance. *J. Biol. Chem.*, 279:44417–44426, 2004.

[38] F. Trandafir, D. Hoogewijs, F. Altieri, P. Rivetti di Val Cervo, K. Ramser, S. Van Doorslaer, J. R. Vanfleteren, L. Moens, and S. Dewilde. Neuroglobin and cytoglobin as potential enzyme or substrate. *Gene*, 398:103–113, 2007.

[39] S. Van Doorslaer, S. Dewilde, L. Kiger, S.V. Nistor, E. Goovaerts, M.C. Marden, and L. Moens. Nitric oxide binding properties of neuroglobin. a characterization by epr and flash photolysis. *J. Biol. Chem.*, 278:4919–4925, 2003.

[40] A.D. Nadra, M.A. Marti, A. Pesce, M. Bolognesi, and D.A. Estrin. Exploring the molecular basis of heme coordination in human neuroglobin. *Proteins*, 71:695–705, 2008.

[41] F.Q. Schafer and G.R. Buettner. Redox environment of the cell as viewed through the redox state of the glutathione disulfide/glutathione couple. *Free Radic. Biol. Med.*, 30:1191–1212, 2001.

[42] T.R. Weiland, S. Kundu, J.T. Trent, J.A. Hoy, and M.S. Hargrove. Bis-histidyl hexacoordination in hemoglobins facilitates heme reduction kinetics. *J. Am. Chem. Soc.*, 126:11930–11935, 2004.

[43] M. Brunori, A. Giuffre, K. Nienhaus, G.U. Nienhaus, F.M. Scandurra, and B. Vallone. Neuroglobin, nitric oxide, and oxygen: functional pathways and conformational changes. *Proc. Natl. Acad. Sci. USA*, 102:8483–8488, 2005.

[44] J.V. Esplugues. No as a signalling molecule in the nervous system. *Br. J. Pharmacol.*, 135:1079–1095, 2002.

[45] S. Herold, A. Fago, R.E. Weber, S. Dewilde, and L. Moens. Reactivity studies of the fe(iii) and fe(ii)no forms of human neuroglobin reveal a potential role against oxidative stress. *J. Biol. Chem.*, 279:22841–22847, 2004.

[46] P. Lipton. Ischemic cell death in brain neurons. *Physiol. Rev.*, 79:1431–1568, 1999.

[47] S.V. Lymar and J.K. Hurst. Rapid reaction between peroxonitrite ion and carbon dioxide: implications for biological activity. *J. Am. Chem. Soc.*, 117:8867–8868, 1995.

[48] S. Herold and A. Fago. Reactions of peroxynitrite with globin proteins and their possible physiological role. *Comp. Biochem. Physiol.*, 142:124–129, 2005.

[49] K. Jin, X.O. Maoa, L. Xiea, A.A. Khana, and D.A. Greenberg. Neuroglobin protects against nitric oxide toxicity. *Neurosci. Lett.*, 430:135–137, 2008.

[50] M.T. Wilson, C. Greenwood, M. Brunori, and E. Antonini. Kinetic studies on the reaction between cytochrome c oxidase and ferrocytochrome c. *Biochem. J.*, 147:145–153, 1975.

[51] A.G. Gilman. G proteins: transducers of receptor-generated signals. *Annu. Rev. Biochem.*, 56:615–649, 1987.

[52] S.R. Sprang. G protein mechanisms: insights from structural analysis. *Annu. Rev. Biochem.*, 66:639–678, 1997.

[53] C. Kitatsuji, M. Kurogochi, S.I. Nishimura, K. Ishimori, and K. Wakasugi. Molecular basis of guanine nucleotide dissociation inhibitor activity of human neuroglobin by chemical cross-linking and mass spectrometry. *J. Mol. Biol.*, 368:150–160, 2007.

[54] S. Watanabe and K. Wakasugi. Neuroprotective function of human neuroglobin is correlated with its guanine nucleotide dissociation inhibitor activity. *Biochem. Biophys. Res. Commun.*, 369(2):695–700, May 2008.

[55] B. Vallone, K. Nienhaus, A. Matthes, M. Brunori, and G.U. Nienhaus. The structure of carbonmonoxy neuroglobin reveals a heme-sliding mechanism for control of ligand affinity. *Proc. Natl. Acad. Sci. USA*, 101:17351–17356, 2004.

[56] R F. Tilton, I.D. Kuntz, and G.A. Petsko. Cavities in proteins: structure of a metmyoglobin-xenon complex solved to 1.9 a. *Biochemistry*, 23:2849–2857, 1984.

[57] G.N. La Mar, D.L. Budd, D.B Viscio, K.M. Smith, and K.C. Langry. Proton nuclear magnetic resonance characterization of heme disorder in hemoproteins. *Proc. Natl. Acad. Sci. USA*, 75:5755–5759, 1978.

[58] F.A. Walker. The heme environment of mouse neuroglobin: histidine imidazole plane orientations obtained from solution nmr and epr spectroscopy as compared with x-ray crystallography. *J. Biol. Inorg. Chem.*, 11:391–397, 2006.

[59] E. Vinck, S. Van Doorslaer, S. Dewilde, G. Mitrikas, A. Schweiger, and L. Moens. Analyzing heme proteins using epr techniques: the heme-pocket structure of ferric mouse neuroglobin. *J. Biol. Inorg. Chem.*, 11:467–475, 2006.

[60] M. Anselmi, M. Brunori, B. Vallone, and A. Di Nola. Molecular dynamics simulation of deoxy and carboxy murine neuroglobin in water. *Biophys. J.*, 93:434–441, 2007.

[61] P. D'Angelo, S. Della Longa, A. Arcovito, M. Anselmi, A. Di Nola, and G. Chillemi. Dynamic investigation of protein metal active sites: interplay of xanes and molecular dynamics simulations. *J. Am. Chem. Soc.*, 132:14901–14909, 2010.

[62] M. Brunori, B. Vallone, F. Cutruzzola, C. Travaglini-Allocatelli, J. Berendzen, K. Chu, R.M. Sweet, and I. Schlichting. The role of cavities in protein dynamics: crystal structure of a photolytic intermediate of a mutant myoglobin. *Proc. Natl. Acad. Sci. USA*, 97:2058–2063, 2000.

[63] A. Ostermann, R. Waschipky, F.G. Parak, and G.U. Nienhaus. Ligand binding and conformational motions in myoglobin. *Nature*, 404:205–208, 2000.

[64] I. Schlichting and K. Chu. Trapping intermediates in the crystal: ligand binding to myoglobin. *Curr. Opin. Struct. Biol.*, 10:744–752, 2000.

[65] M. Brunori and Q.H. Gibson. Cavities and packing defects in the structural dynamics of myoglobin. *EMBO Rep.*, 2:674–679, 2001.

[66] T. Moschetti, U. Mueller, J. Schulze, M. Brunori, and B. Vallone. The structure of neuroglobin at high xe and kr pressure reveals partial conservation of globin internal cavities. *Biophys. J.*, 97:1700–1708, 2009.

[67] M. Petrek, M. Otyepka, P. Banas, P. Kosinova, J. Koca, and J. Damborsky. Caver: a new tool to explore routes from protein clefts, pockets and cavities. *BMC Bioinformatics*, 7:316, 2006.

[68] D. de Sanctis, S. Dewilde, A. Pesce, L. Moens, P. Ascenzi, T. Hankeln, T. Burmester, and M. Bolognesi. Mapping protein matrix cavities in human cytoglobin through xe atom binding. *Biochem. Biophys. Res. Commun.*, 316:1217–1221, 2004.

[69] M. Lim, T.A. Jackson, and P.A. Anfinrud. Ultrafast rotation and trapping of carbon monoxide dissociated from myoglobin. *Nature Struct. Biol.*, 4:209–214, 1997.

[70] K. Nienhaus and G.U. Nienhaus. A spectroscopic study of structural heterogeneity and carbon monoxide binding in neuroglobin. *J.Biol. Phys.*, 31:417–432, 2005.

[71] R. Schmidt-Kastner, C. Schmitz, T. Hankeln, and T. Burmester. Neuroglobin mrna expression after transient global brain ischemia and prolonged hypoxia in cell culture. *Brain Res.*, 1103:173–180., 2006.

[72] E. Fordel, L. Thijs, L. Moens, and S. Dewilde. Neuroglobin and cytoglobin expression mice: evidence for a correlation with reactive oxygen species scavenging. *FEBS J.*, 274:1312–1317, 2007.

[73] T. Burmester, F. Gerlach, and T. Hankeln. Regulation and role of neuroglobin and cytoglobin under hypoxia. *Adv. Exp. Med. Biol.*, 618:169–180, 2007.

[74] C. Zhang, C. Wang, M. Deng, L. Li, H. Wang, M. Fan, W. Xu, F. Meng, L. Qian, and F. He. Full-length cdna cloning of human neuroglobin and tissue expression of rat neuroglobin. *Biochem. Biophys. Res. commun.*, 290:1411–1419, 2002.

[75] U.K. Genick, S.M. Solti, P. Kuhn, I.L. Canestrelli, and E.D. Getzoff. Structure at 0.85 a resolution of an early protein photocycle intermediate. *Nature*, 392:206–209, 1998.

[76] A. Royant, K. Edman, T. Ursby, E. Pebay-Peyroula, E. M. Landau, and R. Neutze. Helix deformation is coupled to

vectorial proton transport in the photocycle of bacteriorhodopsin. *Nature*, 406:645–648, 2000.

[77] D. Bourgeois, X. Vernede, V. Adam, E. Fioravanti, and T. Ursby. A microspectrophotometer for absorption and fluorescence studies of protein crystals. *J. Appl. Cryst.*, 35:319–326, 2002.

[78] Z. Otwinowski and W. Minor. Processing of x-ray diffraction data collected in oscillation mode. *Methods Enzymol.*, 276:307–326, 1997.

[79] A.G.W. Leslie. The integration of macromolecular diffraction data. *Acta Crystallogr. D Biol. Crystallogr.*, 62:48–57, 2006.

[80] Number 4 Collaborative Computational Project. The ccp4 suite: programs for protein crystallography. *Acta Crystallogr. D Biol. Crystallogr.*, 50:760–763, 1994.

[81] G.N. Murshudov, A.A. Vagin, and E.J. Dodson. Refinement of macromolecular structures by the maximum-likelihood method. *Acta Crystallogr. D Biol. Crystallogr.*, 53:240–255, 1997.

[82] M.D. Winn, M.N. Isupov, and G.N. Murshudov. Use of tls parameters to model anisotropic displacements in macromolecular refinement. *Acta Crystallogr. D Biol. Crystallogr.*, 57:122–133, 2001.

[83] P. Emsley and K. Cowtan. Coot: model-building tools for molecular graphics. *Acta Crystallogr. D Biol. Crystallogr.*, 60:2126–2132, 2004.

[84] R.A. Laskowski, M.W. MacArthur, D.S. Moss, and J.M. Thornton. Procheck: A program to check the stereochemical quality of protein structures. *J. Appl. Cryst.*, 26:283–291, 1993.

[85] M. Schiltz, T. Prange, and R. Fourme. On the preparation and x-ray data collection of isomorphous xenon derivatives. *J. Appl. Cryst.*, 27:950–960, 1994.

[86] M. Schiltz, R. Fourme, and T. Prange. Use of noble gases xenon and krypton as heavy atoms in protein structure determination. *Methods Enzymol.*, 374:83–119, 2003.

[87] A. Arcovito, T. Moschetti, P. D'Angelo, G. Mancini, B. Vallone, M. Brunori, and S. Della Longa. An x-ray diffraction and x-ray absorption spectroscopy joint study of neuroglobin. *Arch. Biochem. Biophys.*, 475:7–13, 2008.

[88] D.C. Koningsberger and R. Prins. X-ray absorption: Principles, applications, techniques of exafs, sexafs, and xanes. *Wiley, New York*, 1988.

[89] M.T. Green, J.H. Dawson, and H.B. Gray. Oxoiron(iv) in chloroperoxidase compound ii is basic: implications for p450 chemistry. *Science*, 304:1653–1656, 2004.

[90] P.A. Lee and J.B. Pendry. Theory of the extended x-ray absorption fine structure. *Phys. Rev. B*, 11:2795–2811, 1975.

[91] C.R. Natoli, M. Benfatto, S. Della Longa, and K. Hatada. X-ray absorption spectroscopy: state-of-the-art analysis. *J. Synchrotron. Radiat.*, 10:26–42, 2003.

[92] A. Filipponi, A. Di Cicco, and C.R. Natoli. X-ray-absorption spectroscopy and n-body distribution functions in condensed matter. i. theory. *Phys. Rev. B Condens. Matter*, 52:15122–15134, 1995.

[93] M. Benfatto and S. Della Longa. Geometrical fitting of experimental xanes spectra by a full multiple-scattering procedure. *J. Synchrotron Radiat.*, 8:1087–1094, 2001.

[94] A. Filipponi and A. Di Cicco. X-ray-absorption spectroscopy and n-body distribution functions in condensed matter. ii. data analysis and applications. *Phys. Rev. B Condens. Matter.*, 52:15135–15149, 1995.

[95] S. Della Longa and A. Arcovito. X-ray-induced lysis of the fe-co bond in carbonmonoxy-myoglobin. *Inorg. Chem.*, 49:9958–9961, 2010.

[96] A. Arcovito, D. C. Lamb, G.U. Nienhaus, J.L. Hazemann, M. Benfatto, and S. Della Longa. Light-induced relaxation of photolyzed carbonmonoxy myoglobin: a temperature-dependent x-ray absorption near-edge structure (xanes) study. *Biophys. J.*, 88:2954–2964, 2005.

[97] J. Yano and V.K. Yachandra. X-ray absorption spectroscopy. *Photosynth. Res.*, 102:241–254, 2009.

[98] G. Bricogne, S.C. Capelli, G. Evans, A. Mitschler, P. Pattison, P. Roversi, and M. Schiltz. X-ray absorption, refraction and resonant scattering tensors in selenated protein crystals: implications for data collection strategies in macromolecular crystallography. *J. Appl. Crystallogr.*, 38:168–72, 2004.

[99] A. Arcovito, M. Benfatto, M. Cianci, S.S. Hasnain, K. Nienhaus, G.U. Nienhaus, C. Savino, R.W. Strange, B. Vallone, and S. Della Longa. X-ray structure analysis of a metalloprotein with enhanced active-site resolution using in situ x-ray absorption near edge structure spectroscopy. *Proc. Natl. Acad. Sci. USA*, 104:6211–6216, 2007.

[100] A. Arcovito, A. Bonamore, J.L. Hazemann, A. Boffi, and P. D'Angelo. Unusual proximal heme pocket geometry in the deoxygenated thermobifida fusca: A combined spectroscopic investigation. *Biophys. Chem.*, 147:1–7, 2010.

[101] P. D'Angelo, A. Lapi, V. Migliorati, A. Arcovito, M. Benfatto, O.M. Roscioni, W . Meyer-Klaucke, and S. Della-Longa. X-ray absorption spectroscopy of hemes and hemeproteins in solution: multiple scattering analysis. *Inorg. Chem.*, 47:9905–9918, 2008.

[102] S. Della Longa, A. Arcovito, M. Girasole, J.L. Hazemann, and M. Benfatto. Quantitative analysis of x-ray

absorption near edge structure data by a full multiple scattering procedure: the fe-co geometry in photolyzed carbonmonoxy-myoglobin single crystal. *Phys. Rev. Lett.*, 87:155501, 2001.

[103] L. Hedin and B.I. Lundqvist. Explicit local exchange-correlation potentials. *J. Phys. C.*, 4:2064–75, 1971.

[104] M. Anselmi, M. Brunori, B. Vallone, and A. Di Nola. Molecular dynamics simulation of the neuroglobin crystal: comparison with the simulation in solution. *Biophys. J.*, 95:4157–4162, 2008.

[105] T.R. Schneider. Objective comparison of protein structures: error-scaled difference distance matrices. *Acta Crystallogr. D Biol. Crystallogr.*, 56:714–721, 2000.

[106] J. Wuerges, J.W. Lee, Y.I. Yim, H.S. Yim, S.O. Kang, and K.D. Carugo. Crystal structure of nickel-containing superoxide dismutase reveals another type of active site. *Proc. Natl. Acad. Sci. USA*, 101:8569–8574, 2004.

[107] J. Yano, J. Kern, K.D. Irrgang, M.J. Latimer, U. Bergmann, P. Glatzel, Y. Pushkar, J. Biesiadka, B. Loll, K. Sauer, J. Messinger, A. Zouni, and V.K. Yachandra. X-ray damage to the mn4ca complex in single crystals of photosystem ii: a case study for metalloprotein crystallography. *Proc. Natl. Acad. Sci. USA*, 102:12047–12052, 2005.

[108] T. Beitlich, K. Kuhnel, C. Schulze-Briese, R.L. Shoeman, and I. Schlichting. Cryoradiolytic reduction of crystalline heme proteins: analysis by uv-vis spectroscopy and x-ray crystallography. *J. Synchrotron Radiat.*, 14:11–23, 2007.

[109] W. A. Eaton and J. Hofrichter. Polarized absorption and linear dichroism spectroscopy of hemoglobin. *Methods Enzymol.*, 76:175–261, 1981.

[110] J. Murray and E. Garman. Investigation of possible free-radical scavengers and metrics for radiation damage in protein cryocrystallography. *J. Synchrotron Radiat.*, 9:347–354, 2002.

[111] T. De la Mora-Rey and C.M. Wilmot. Synergy within structural biology of single crystal optical spectroscopy and x-ray crystallography. *Curr. Opin. Struct. Biol.*, 17:580–586, 2007.

[112] J. McGeehan, R.B.G. Ravelli, J.W. Murray, R.L. Owen, F. Cipriani, S. McSweeney, M. Weik, and E.F. Garman. Colouring cryo-cooled crystals: online microspectrophotometry. *J. Synchrotron Radiat.*, 16:163–172, 2009.

[113] S. Macedo, M. Pechlaner, W. Schmid, M. Weik, K. Sato, C. Dennison, and K. Djinovic-Carugo. Can soaked-in scavengers protect metalloprotein active sites from reduction during data collection? *J. Synchrotron Radiat*, 16:191–204, 2009.

[114] E. Antonini and M. Brunori. *Hemoglobin and myoglobin in their reactions with ligands.*, volume 21 of *Frontiers of biology*. Amsterdam, North-Holland Pub. Co., 1971.

[115] C. Yu, I.C. Gunsalus, M. Katagiri, K. Suhara, and S. Takemori. Cytochrome p-450cam. i. crystallization and properties. *J. Biol. Chem.*, 249:94–101, 1974.

[116] I. Schlichting, J. Berendzen, G.N. Phillips, and R.M. Sweet. Crystal structure of photolysed carbonmonoxy-myoglobin. *Nature*, 371:808–812, 1994.

[117] A.P. Duff, D.M. Trambaiolo, A.E. Cohen, P.J. Ellis, G.A. Juda, E.M. Shepard, D.B. Langley, D.M. Dooley, H.C. Freeman, and J.M. Guss. Using xenon as a probe for dioxygen-binding sites in copper amine oxidases. *J. Mol. Biol.*, 344:599–607, 2004.

[118] I. Schlichting, J. Berendzen, K. Chu, A.M. Stock, S.A. Maves, D.E. Benson, R.M. Sweet, D. Ringe, G.A. Petsko, and S.G. Sligar. The catalytic pathway of cytochrome p450cam at atomic resolution. *Science*, 287:1615–1622, 2000.

Appendix

Appendix

Biochemical and Biophysical Research Communications 390 (2009) 121–124

Contents lists available at ScienceDirect

Biochemical and Biophysical Research Communications

journal homepage: www.elsevier.com/locate/ybbrc

Failure of apoptosis-inducing factor to act as neuroglobin reductase

Tommaso Moschetti [a], Alessandro Giuffrè [a], Chiara Ardiccioni [a], Beatrice Vallone [a], Nazanine Modjtahedi [b,c,d], Guido Kroemer [b,c,d], Maurizio Brunori [a,*]

[a] Department of Biochemical Sciences and CNR Institute of Molecular Biology and Pathology, Sapienza University of Rome, I-00185 Rome, Italy
[b] INSERM U848, Pavillon de Recherche 1, 94805 Villejuif, France
[c] Institut Gustave Roussy, Pavillon de Recherche 1, 94805 Villejuif, France
[d] Université Paris Sud-Paris 11, Pavillon de Recherche 1, 94805 Villejuif, France

ARTICLE INFO

Article history:
Received 15 September 2009
Available online 24 September 2009

Keywords:
Neuroprotection
Apoptosis
Hexacoordinate globins
Hypoxia
Enzymatic reduction
Electron transfer
Flavoproteins
Cytochrome *c*
Nitric oxide

ABSTRACT

Neuroglobin (Ngb) is a hexacoordinate globin expressed in the nervous system of vertebrates, where it protects neurons against hypoxia. Ferrous Ngb has been proposed to favor cell survival by scavenging NO and/or reducing cytochrome *c* released into the cytosol during hypoxic stress. Both catalytic functions require an as yet unidentified Ngb-reductase activity. Such an activity was detected both in tissue homogenates of human brain and liver and in *Escherichia coli* extracts. Since NADH:flavorubredoxin oxidoreductase from *E. coli*, that was shown to reduce ferric Ngb, shares sequence similarity with the human apoptosis-inducing factor (AIF), AIF has been proposed by us as a candidate Ngb reductase. In this study, we tested this hypothesis and show that the Ngb-reductase activity of recombinant human AIF is negligible and hence incompatible with such a physiological function.

Introduction

Neuroglobin (Ngb) is a member of the superfamily of vertebrate globins that is expressed at micromolar concentration in several areas of the CNS and even more abundantly in the retina [1,2]. Ngb has been suggested to participate in oxygen transport and/or sensing, as well as in the defence against radical species [3,4]. Ngb acts as a potent neuroprotectant, and its overexpression improves recovery after experimental stroke [5,6].

In vitro Ngb efficiently reduces cytochrome *c* (Cyt-c; [7]) and scavenges NO when Ngb is in its O_2-bound form [8]. Under hypoxic conditions, the increase in NO concentration has a number of detrimental consequences such as blockade of the respiratory chain, mitochondrial membrane depolarization and production of highly reactive species such as peroxynitrite, thereby eventually causing cell death [9]. Mitochondrial insults are associated with the release into the cytosol of Cyt-c, which, in its oxidized form, potently activates caspases and thus triggers apoptotic cell death [10]. Ngb could negatively regulate cell death by limiting the NO concentration and by reducing oxidized cytoplasmic Cyt-c. These catalytic activities may explain the neuroprotective action of Ngb under conditions of hypoxia and ischemia *in vivo* [4,11].

Both Cyt-c reduction and NO scavenging cause the oxidation of ferrous Ngb (Ngb(FeII)) to ferric Ngb (Ngb(FeIII)). Since only Ngb(FeII) is competent for O_2 binding and catalysis, Ngb can only act as a neuroprotectant if it is continuously reduced by a reductase that maintains redox cycling of the protein. Accordingly, an NAD(P)H-dependent Ngb-reductase activity has been detected in tissue homogenates of human brain and liver [12], but the enzyme(s) responsible for this activity has not been identified yet. *Escherichia coli* extracts also contain an Ngb-reducing system that has been identified as the NADH:flavorubredoxin oxidoreductase (FlRd-red) [13]. FlRd-red is the redox partner of flavorubredoxin, an enzyme implicated in the anaerobic detoxification of NO in *E. coli* [14,15]. Blast analysis of the sequence of *E. coli* FlRd-red against the human genome yielded, as the first hit, the FAD-binding domain of the mitochondrial apoptosis-inducing factor (AIF; 21% identical residues, 42% homologous residues and *E*-value = $2e^{-12}$; [13]), the main caspase-independent effector of cell death [16]. In healthy cells, AIF is

Abbreviations: Ngb, neuroglobin; Cyt-c, cytochrome *c*; Ngb(FeIII), ferric neuroglobin; Ngb(FeII), ferrous neuroglobin; FlRd-red, *Escherichia coli* NADH:flavorubredoxin oxidoreductase; AIF, apoptosis-inducing factor; NCtag-AIF, AIF carrying both N- and C-terminal histidine tags; Ctag-AIF, AIF carrying only a C-terminal histidine tag.

* Corresponding author. Address: Dipartimento di Scienze Biochimiche 'A. Rossi Fanelli', Sapienza Università di Roma, Piazzale Aldo Moro 5, I-00185 Roma, Italy. Fax: +39 06 4440062.
E-mail address: maurizio.brunori@uniroma1.it (M. Brunori).

0006-291X/$ - see front matter © 2009 Elsevier Inc. All rights reserved.
doi:10.1016/j.bbrc.2009.09.078

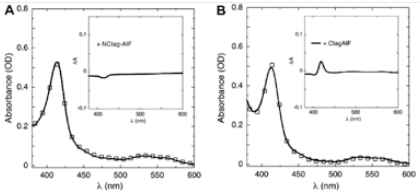

Fig. 1. Ngb reduction assay in the presence of catalytic amounts of AIF. In the presence of 100 μM NADH, no significant reduction of ferric Ngb (4.6 μM) was observed after incubation with 350 nM NCtag-AIF (A) or Ctag-AIF (B). Ngb spectra collected after 30 min of anaerobic incubation (squares) are compared with the spectrum of ferric Ngb (solid line). Insets: difference of the spectra depicted in the main panels.

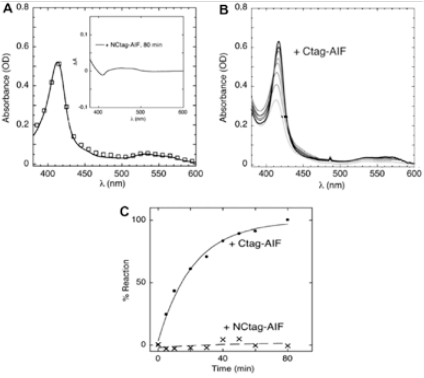

Fig. 2. Ngb reduction assay using reduced AIF in excess. Ferric Ngb, 5 μM (A) or 3 μM (B), was anaerobically incubated with 18 μM NCtag-AIF (A) or Ctag-AIF (B), pre-reduced by NADH, under CO atmosphere. After 80 min incubation, Ngb was not significantly reduced by NCtag-AIF, whereas a slow reduction occurred in the presence of Ctag-AIF. Inset: absorption changes after 80 min incubation. (C) Ngb reduction time courses, as monitored at 418 nm.

localized in the mitochondrial intermembrane space. Upon permeabilization of the outer mitochondrial membrane, AIF translocates first to the cytosol and then to the nucleus where it participates in chromatin condensation and DNA degradation [16]. However, AIF has also neuroprotective functions, and mice lacking AIF expression due to a hypomorphic mutation exhibit in the brain an increased level of cell death that causes neurodegeneration [17]. Based on its sequence similarity with FlRd-red, we hypothesized that cytoplasmic AIF might be able to reduce Ngb [13] and thereby maintain Ngb redox cycling, favoring neuron survival under hypoxia. Here, we show that *in vitro* AIF fails to efficiently reduce Ngb(FeIII) and therefore conclude that the hypothesis outlined above is untenable.

Appendix

Materials and methods

Protein expression and purification. Mouse Ngb was purified as previously described [13]. Human Δ1–120 AIF was cloned into the expression vector pET28-b and expressed in *E. coli* strain Rosetta BL21(DE3) pLysS. The protein with histidine tags at both the N- and C-terminus (NCtag-AIF) was purified according to [18]. When specified, the N-terminal histidine tag was cleaved off by treatment with bovine thrombin. In this case, we will refer to the protein as Ctag-AIF (AIF carrying only a C-terminal histidine tag).

Neuroglobin reduction assay. Ngb reduction assays were carried out in 0.1 M K/phosphate buffer, pH 7.0, 20 μM EDTA, in the presence of 100–200 μM NADH; anaerobic conditions were obtained by extensively purging the buffer with N_2 gas. An aliquot of 1.5 ml reaction mixture, containing NADH, AIF and Ngb, was placed into a gas-tight cuvette and the process followed with an HP8453 UV–Vis spectrophotometer, collecting spectra in the UV–Vis range (200–650 nm) every 20 s for the first 3 min, then every 5 min.

NADH-oxidase activity of AIF. The NADH-oxidase activity of NCtag-AIF was measured spectrophotometrically. The assay was carried out at 25 °C in a total volume of 1.0 ml air-equilibrated buffer (50 mM Tris–HCl, pH 8) containing 200 μM NADH. The reaction was initiated by addition of AIF at a final concentration of 2 μM and, then, followed by monitoring the absorption decrease at 340 nm for 25 min.

Results and discussion

Upon induction of an apoptotic stimulus, AIF migrates from mitochondria to the nucleus and induces chromatin condensation [18]. We proposed that AIF present in the cytosol might intercept and reduce ferric Ngb [13]. Therefore, we tested if Ngb(FeIII) is reduced by recombinant AIF *in vitro*. Initially, we performed the Ngb(FeIII) reduction experiments following the same protocol successfully used with *E. coli* FlRd-red [13]. When catalytic amounts of recombinant AIF protein were added to a reaction mixture containing Ngb(FeIII) and 100 μM NADH under anaerobic conditions, no significant spectral changes occurred within 30 min (Fig. 1A). Since Churbanova and Sevrioukova [19] demonstrated that the redox properties of AIF are affected by the presence of N- or C-terminal His-tags, we compared two different preparations of recombinant AIF that were purified based on the presence of N-terminal and/or C-terminal His-tags. Both these AIF constructs were similarly deficient in their capacity to reduce Ngb(FeIII) *in vitro* (Fig. 1B).

Next, the putative existence of electron transfer was evaluated under anaerobic conditions, by mixing ferric Ngb with an excess of AIF that had been pre-reduced with NADH. Small amounts of contaminant O_2 might interfere with the apparent reduction time course, because O_2 binds to Ngb(FeII) and causes rapid protein autoxidation [20]. Therefore, in the experiment reported in Fig. 2, the sample was pre-equilibrated with 1 atm CO (≅1 mM), which binds with high affinity to Ngb(FeII) and thus competes with O_2 binding and re-oxidation of Ngb. When pre-reduced NCtag-AIF (which possesses two His-tags at both the C- and N-terminus) was employed, no detectable reduction of Ngb was observed (Fig. 2A); when an excess of pre-reduced Ctag-AIF (which lacks the N-terminal His-tag) was employed, a change in the Soret maximum from 413 nm (Ngb(FeIII)) to 417 nm (Ngb(FeII–CO)) was detected (Fig. 2B), although the process was too slow ($t_{1/2} \sim 15$ min, Fig. 2C) to be physiologically meaningful.

Since NCtag-AIF was totally ineffective in the aforementioned reaction, we verified its NADH-oxidase activity (see Materials and methods). The resulting k_{cat} for NADH was 0.025 min^{-1}, showing that NCtag-AIF was redox active towards NADH and O_2, though ~6–10 times less than the preparation employed by Miramar et al. [21]. It should be noticed that the experiment in Fig. 2 was carried out using pre-reduced AIF in excess over Ngb (4- to 6-fold), and therefore Ngb reduction could not be rate-limited by electron transfer from NADH to AIF.

From these results, we conclude that AIF can reduce Ngb(FeIII) in the presence of NADH but only at a very low rate, indicating that AIF is not the redox-active enzyme that recycles oxidized Ngb to Ngb(FeII) (Fig. 2). Thus, in spite of the intriguing sequence similarity between human AIF and *E. coli* FlRd-red, it appears that the Ngb-reductase activity detected in liver and brain homogenates cannot be attributed to AIF, at least based on the results obtained with the protein constructs herein tested. In conclusions, the hypothesis that we previously proposed [13] is falsified by the present data. Future studies will hopefully discover the molecular identity of the physiologically relevant Ngb(FeIII) reductase.

Acknowledgments

This work has been partially supported by grants from the European Union (Apo-Sys) to G.K., and by MiUR of Italy (FIRB RBRN07BMCT "Italian Human Proteome Network") to M.B. T.M. was recipient of a fellowship supported by MiUR of Italy (FIRB RBIN04PWNC).

We thank Gerry Melino (Rome, Italy) for helpful discussions and critical reading of the manuscript.

References

[1] T. Burmester, B. Weich, S. Reinhardt, T. Hankeln, A vertebrate globin expressed in the brain, Nature 407 (2000) 520–523.
[2] M. Schmidt, A. Gerlol, T. Laufs, T. Hankeln, U. Wolfrum, T. Burmester, How does the eye breathe? Evidence for neuroglobin-mediated oxygen supply in the mammalian retina, J. Biol. Chem. 278 (2003) 1932–1935.
[3] T. Hankeln, B. Ebner, C. Fuchs, F. Gerlach, M. Haberkamp, T.L. Laufs, A. Roesner, M. Schmidt, B. Weich, S. Wystub, S. Saaler-Reinhardt, S. Reuss, M. Bolognesi, D. De Sanctis, M.C. Marden, L. Kiger, L. Moens, S. Dewilde, E. Nevo, A. Avivi, R.E. Weber, A. Fago, T. Burmester, Neuroglobin and cytoglobin in search of their role in the vertebrate globin family, J. Inorg. Biochem. 99 (2005) 110–119.
[4] M. Brunori, B. Vallone, A globin for the brain, FASEB J. 20 (2006) 2192–2197.
[5] Y. Sun, K. Jin, A. Peel, X.O. Mao, L. Xie, D.A. Greenberg, Neuroglobin protects the brain from experimental stroke *in vivo*, Proc. Natl. Acad. Sci. USA 100 (2003) 3497–3500.
[6] A.A. Khan, X.O. Mao, S. Banwait, C.M. DerMardirossian, G.M. Bokoch, K. Jin, D.A. Greenberg, Regulation of hypoxic neuronal death signaling by neuroglobin, FASEB J. 22 (2008) 1737–1747.
[7] A. Fago, A.J. Mathews, L. Moens, S. Dewilde, T. Brittain, The reaction of neuroglobin with potential redox protein partners cytochrome b_5 and cytochrome *c*, FEBS Lett. 580 (2006) 4884–4888.
[8] M. Brunori, A. Giuffrè, K. Nienhaus, G.U. Nienhaus, F.M. Scandurra, B. Vallone, Neuroglobin, nitric oxide, and oxygen: functional pathways and conformational changes, Proc. Natl. Acad. Sci. USA 102 (2005) 8483–8488.
[9] B. Brune, A. von Knethen, K.B. Sandau, Nitric oxide (NO): an effector of apoptosis, Cell Death Differ. 6 (1999) 969–975.
[10] M.O. Hengartner, The biochemistry of apoptosis, Nature 407 (2000) 770–776.
[11] A. Fago, A.J. Mathews, T. Brittain, A role for neuroglobin: resetting the trigger level for apoptosis in neuronal and retinal cells, IUBMB Life 60 (2008) 398–401.
[12] F. Trandafir, D. Hoogewijs, F. Altieri, P. Rivetti di Val Cervo, K. Ramser, S. Van Doorslaer, J.R. Vanfleteren, L. Moens, S. Dewilde, Neuroglobin and cytoglobin as potential enzyme or substrate, Gene 398 (2007) 103–113.
[13] A. Giuffrè, T. Moschetti, B. Vallone, M. Brunori, Neuroglobin: enzymatic reduction and oxygen affinity, Biochem. Biophys. Res. Commun. 367 (2008) 893–898.
[14] A.M. Gardner, R.A. Helmick, P.R. Gardner, Flavorubredoxin, an inducible catalyst for nitric oxide reduction and detoxification in *Escherichia coli*, J. Biol. Chem. 277 (2002) 8172–8177.
[15] C.M. Gomes, A. Giuffrè, E. Forte, J.B. Vicente, L.M. Saraiva, M. Brunori, M. Teixeira, A novel type of nitric-oxide reductase. *Escherichia coli* flavorubredoxin, J. Biol. Chem. 277 (2002) 25273–25276.
[16] N. Modjtahedi, F. Giordanetto, F. Madeo, G. Kroemer, Apoptosis-inducing factor: vital and lethal, Trends Cell Biol. 16 (2006) 264–272.
[17] J.A. Klein, C.M. Longo-Guess, M.P. Rossmann, K.L. Seburn, R.E. Hurd, W.N. Frankel, R.T. Bronson, S.L. Ackerman, The harlequin mouse mutation downregulates apoptosis-inducing factor, Nature 419 (2002) 367–374.
[18] H. Ye, C. Cande, N.C. Stephanou, S. Jiang, S. Gurbuxani, N. Larochette, E. Daugas, C. Garrido, G. Kroemer, H. Wu, DNA binding is required for the apoptogenic action of apoptosis inducing factor, Nat. Struct. Biol. 9 (2002) 680–684.

[19] I.Y. Churbanova, I.F. Sevrioukova, Redox-dependent changes in molecular properties of mitochondrial apoptosis-inducing factor, J. Biol. Chem. 283 (2008) 5622–5631.
[20] S. Dewilde, L. Kiger, T. Burmester, T. Hankeln, V. Baudin-Creuza, T. Aerts, M.C. Marden, R. Caubergs, L. Moens, Biochemical characterization and ligand binding properties of neuroglobin, a novel member of the globin family, J. Biol. Chem. 276 (2001) 38949–38955.
[21] M.D. Miramar, P. Costantini, L. Ravagnan, L.M. Saraiva, D. Haouzi, G. Brothers, J.M. Penninger, M.L. Peleato, G. Kroemer, S.A. Susin, NADH oxidase activity of mitochondrial apoptosis-inducing factor, J. Biol. Chem. 276 (2001) 16391–16398.

Appendix

J. Phys. Chem. B **2010,** *114,* 13223–13231

Polarized X-ray Absorption Near-Edge Structure Spectroscopy of Neuroglobin and Myoglobin Single Crystals

Alessandro Arcovito,*,† Chiara Ardiccioni,‡ Michele Cianci,§ Paola D'Angelo,‖ Beatrice Vallone,‡ and Stefano Della Longa*,⊥

Istituto di Biochimica e Biochimica Clinica, Università Cattolica del Sacro Cuore, L. go F. Vito 1, 00168 Rome, Italy, Dipartimento di Scienze Biochimiche "A. Rossi-Fanelli", Sapienza Università di Roma, Piazzale A. Moro 5, 00185 Rome, Italy, European Molecular Biology Laboratory, Hamburg Outstation, Notkestrasse 85, 22603, Hamburg, Germany, Dipartimento di Chimica, Sapienza Università di Roma, Piazzale A. Moro 5, 00185 Rome, Italy, and Dipartimento di Medicina Sperimentale, Università "L'Aquila", Via Vetoio, 67100 L'Aquila, Italy

Received: May 14, 2010; Revised Manuscript Received: September 6, 2010

Polarized Fe K-edge X-ray absorption near-edge structure (XANES) spectra of murine carbonmonoxy−neuroglobin (NgbCO) single crystals have been collected and compared with a number of derivatives of sperm whale myoglobin (Mb), that is, the nitrosyl (MbNO) and deoxy (Mb) derivatives, the previously reported cyanomet (MbCN) and carbonmonoxy (MbCO) derivatives, and the cryogenic photoproduct of MbCO (Mb·CO). The single crystals under study exhibit a strong XANES angular dichroism which allows the heme geometry of each sample to be analyzed with extremely high accuracy via the full multiple scattering (MS) approach. The results of two alternative methods to undergo the MS analysis have been compared with high resolution X-ray diffraction (XRD) data and with X-ray absorption spectroscopy (XAS) data in solution. As a result of the present analysis, the Fe-heme structure in solution and in the cryo-trapped NgbCO single crystal (which cracks at room temperature) are the same. Accordingly, the residual energy involved in the protein relaxation responsible of crystal cracking at room temperature after CO binding does not reside in the heme pocket. A combined approach (polarized XANES and XRD) is suggested to be applied on the same single crystals of metalloproteins at opportunely equipped synchrotron beamlines.

Introduction

Biochemical reactions taking place in the living cell demand these reactions to be highly specific. Proteins achieve such specificity through geometrical and chemical precision in molecular interactions. As a consequence, a detailed determination of protein structure, especially at the level of the active site, is a critical step in structural biology research.[1]

X-ray absorption spectroscopy (XAS) is a powerful technique able to investigate both local structure and dynamics of protein metal centers[2,3] and especially on a wide class of them such as hemeproteins.[4−9] In fact, XAS can reveal structural parameters around metal centers with very high accuracy, comparable to that of small-molecule crystallography, typically around 1 Å resolution. Such detailed structural data can be essential for elucidating the function of the hemeprotein under study,[9] as structural changes to the metal coordination during redox or substrate-binding reactions are generally <0.1 Å and hence remain unnoticed in standard protein crystallography at lower resolution.

Moreover, even when the X-ray structure of a protein expressed in the cell during a relevant physiological process is known, this knowledge is sometimes not enough to unravel its function. For instance, Figure 1 shows the noticeable superimposition of the three-dimensional structure of two hemeproteins belonging to globin family, myoglobin (MbCO; PDB code: 1A6G) and neuroglobin (NgbCO; PDB code: 1W92); the former one is abundant in the muscles, while the latter is found in the nervous system of vertebrates. Both of these proteins can bind

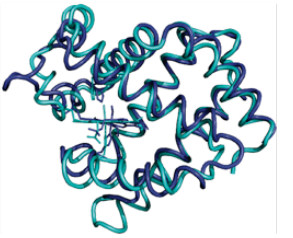

Figure 1. Structural superimposition of murine NgbCO (blue) and sperm whale MbCO (light blue), based on the position of the backbone Cα atoms.

* Corresponding authors. E-mail: alessandro.arcovito@rm.unicatt.it; tel.: +39 06 30156706; fax: +39 06 30156783 (A.A.). E-mail: dlonga@caspur.it; tel.: +39 0862 433568; fax: +39 0862 433523 (S.D.L.).
† Università Cattolica del Sacro Cuore.
‡ Dipartimento di Scienze Biochimiche "A. Rossi-Fanelli", Sapienza Università di Roma.
§ European Molecular Biology Laboratory.
‖ Dipartimento di Chimica, Sapienza Università di Roma.
⊥ Università "L'Aquila".

10.1021/jp104395g
Published on Web 09/29/2010

Appendix

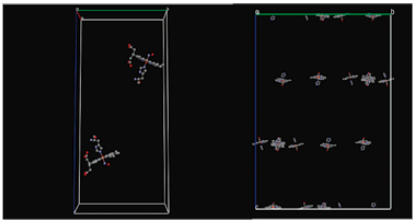

Figure 2. Sketches of the 2 oriented hemes of MbNO (on the left, $P2_1$ space group) and the 18 hemes of murine NgbCO (on the right, $R32$ space group) in their crystal unit cells.

oxygen and diatomic gases reversibly and have strong similarities in the fold, but the Fe-heme properties are quite different: the 5-coordinate species in Ngb is only a transient state, and its sixth ligand position in the absence of an exogenous ligand is always occupied by an endogenous histidine. Whereas Mb is a well-known protein involved in oxygen storage and delivery in muscles as well as in the cell detoxification process,[10] this function in Ngb is ruled out, and its role in the cell is still under debate.[11,12]

X-ray absorption near-edge structure (XANES) fingerprints are usually interpreted to elucidate the oxidation state and the overall symmetry of the metal site by direct comparison with model standards.[13] Furthermore, in many cases, for hemeproteins, the XANES dichroism of the heme can be exploited. In the general case, assuming that the incident beam is linearly polarized along a direction denoted by the vector $\boldsymbol{\varepsilon}$, each spectrum j (i.e., each crystal orientation) samples a particular direction $\boldsymbol{\varepsilon}_j$. The fluorescence intensity emitted as a function of the energy E from a small crystal is proportional, within the dipole approximation of the photoelectron absorption cross section, to the quadratic form σ_j

$$\sigma_j(E) = \boldsymbol{\varepsilon}_j^T \boldsymbol{\sigma}(E) \boldsymbol{\varepsilon}_j \tag{1}$$

where $\boldsymbol{\sigma}(E)$ denotes the absorption tensor, the superscript T indicates the transpose, and $\sigma_j(E)$ denotes the effective scalar linear absorption coefficient along the direction $\boldsymbol{\varepsilon}_j$. According to the crystal symmetry, the absorption tensor is provided by a certain number of orientation-dependent spectra, and the "solution equivalent spectrum", comparable with the solution spectrum, is obtained by the trace of the tensor, divided by three.[14]

When the local structure around a metal center has a C4 symmetry (approximately the one of the Fe-heme site), a simplified approach can be adopted. First, it is advantageous to consider the XAS components linearly polarized along its symmetry axis (the heme normal), I_{normal}, and along a direction in the C4 plane (the heme plane), I_{heme}. Assuming perfect C4 symmetry, for a certain angle ϑ between the polarization vector $\boldsymbol{\varepsilon}$ and the heme normal, the polarized spectrum is given, as a function of I_{heme} and I_{normal}, simply by

$$I_\vartheta = I_{normal} \cos^2 \vartheta + I_{heme} \sin^2 \vartheta \tag{2}$$

that means that the X-ray absorption cross section of the heme is approximately dichroic; in the presence of m symmetry related hemes in the unit cell of the crystal it is possible to write:

$$\begin{aligned} I_\vartheta &= \frac{1}{m} \sum_1^m (I_{normal} \cos^2 n_i\vartheta + I_{heme} \sin^2 n_i\vartheta) \\ &= \frac{1}{m}[I_{normal} \sum_1^m (\cos^2 n_i\vartheta) + I_{heme} \sum_1^m (1 - \cos^2 n_i\vartheta)] \\ &= a_\vartheta I_{normal} + b_\vartheta I_{heme} \end{aligned} \tag{3}$$

where $a_\vartheta = (1/m)\sum_1^m(\cos^2 n_i\vartheta)$; $b_\vartheta = 1 - a_\vartheta$; ϑ is now a rotational angle of an oriented crystal in the laboratory system, and $n_i\vartheta$ are the angles between each heme normal n_i and the X-ray polarization vector $\boldsymbol{\varepsilon}$ that correspond to ϑ. By increasing the m value, and if the directions of the several heme normal vectors are homogeneously scattered on the rotational sphere, the collected XAS signal approaches the average solution signal. The value $a_\vartheta = 0.33$ (corresponding for a single heme normal to the "magic angle" $n_i\vartheta = 54.7°$) gives the 1:2 ratio between I_{normal} and I_{heme}. In these conditions, and under the approximations stated above, the polarized XAS spectrum collected on the single crystal is directly superimposable to the XAS spectrum collected in solution, residual small differences depending on experimental conditions and on the degree of departure from a perfect C4 symmetry. On the contrary, the more the m symmetry-related heme planes are oriented parallel (or antiparallel) in the unit cell, the more the XAS dichroism is maintained in the single crystal; in all of these cases, the XAS angular dependence can provide an enhanced resolution of the heme site with respect to both X-ray crystallography and solution XAS.

One example of strong dichroism is the $P2_1$ space group of sperm whale myoglobin having two hemes in the unit cell oriented almost (anti)parallel at 23° from the heme normals. Figure 2, left frame, shows the two hemes on projections along the crystal axes, in the case of carbonmonoxy-derivative (Protein Data Bank, PDB, code 1A6G). It is possible to calculate the a_ϑ coefficient for any chosen orientation from the PDB data entry. For example, by rotating the crystal around the **b**-axis, kept perpendicular to the X-ray polarization vector $\boldsymbol{\varepsilon}$ (in a synchrotron radiation experiment the $\boldsymbol{\varepsilon}$ vector is in the plane of the electron

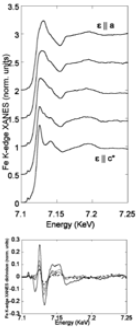

Figure 3. Angular dependence of the Fe K-edge polarized XANES spectra of MbCN. By rotating the crystal around the **b** crystal axis, from bottom (ε‖**c***) to top (ε‖**a**), the angle between each heme normal and the ε vector is 23°, 45°, 56°, 65°, and 90°, respectively. The dichroism of the XANES signal is revealed by observing the same difference XANES spectrum with increasing intensity as increases the angular variation (lower frame). The major difference (solid line) corresponds to the two extreme orientations (ε‖**a**) and (ε‖**c***).

synchrotron orbit, thus it corresponds to a vertical orientation of the **b**-axis), the a_β coefficient varies between 0 and 0.85, values that correspond to two experimental signals I_a and I_{c^*} containing only I_{heme} when ε‖**a** or $(0.85I_{normal} + 0.15I_{heme})$ when ε‖**c***, respectively. The pure I_{normal} component is then recovered as $I_{normal} = (I_{c^*} - 0.15I_a)/0.85$; the I_{normal} component is extremely sensitive to the type and binding geometry of the heme axial ligand, providing the fine structural details of the coordination of various molecules to the Fe-heme, like proximal histidine, CN, CO, NO, and H_2O.

In Figure 3, upper frame, XANES spectra collected at conveniently chosen angles in the plane of the **ac*** crystal axes of a MbCN protein crystal are shown. In the lower frame, their differential spectra display the same shape with different intensity, according to the above-mentioned XANES dichroism. The two components I_{heme} and I_{normal} of the dichroic signal are derived from these angular-dependent spectra.[15]

Treatment of XANES spectra has been performed using the MXAN procedure.[16] It works in the standard multiple scattering (MS) theoretical environment using the muffin-tin (MT) approximation for the shape of the potential and the so-called "extended continuum" scheme to calculate both the bound states and the continuum part of the XAS spectrum. The overcoming of the MT approximation[17,18] and the use of a self-consistent (SCF) procedure[19] for the whole cluster to generate the potential is the way to remove the use of arbitrary parameters of the MT approximation and the systematic error linked to them. However, their full use in a fitting procedure is still too complex and prohibitively time-consuming. Moreover, during a fitting procedure, the calculation of a SCF charge density for a geometry far from the "true one" could be even harmful, as it could select wrong excited electron configurations. For these reasons, in a number of previous publications on heme-proteins[5,8,15] we have calculated the SCF MT potential related to the starting structure, chosen on the basis of the information derived by high resolution diffraction data available in the protein data bank, but we were unable to recalculate the potential when distorting the starting structure, at each step of structural optimization. The inability to recalculate the potential was a source of a systematic error in the fitting procedure: the more the starting structure is far from the "true" one, the more this error affects the results. More recently, we have tested a different strategy, that is, the possibility to "mimic" SCF by refining some MT parameter linked to the potential calculation during the MXAN structural optimization.[20] The potential in this way can be quickly recalculated, but another source of systematic error is introduced if a relevant statistical correlation exists between the refined potential parameters and some structural parameters. By using the latter procedure, the MXAN analysis has been compared with extended X-ray absorption fine structure (EXAFS) when applied to several model systems, from hydrated ions to crystals,[21−24] and the numerical results were in fine agreement; heme models and hemeproteins are more challenging to the MT theory due to the strong asymmetry of their structure around the Fe ion. However, we showed[20] that the overall accuracy of MXAN in solution, including the related systematic errors, is approximately comparable to that of 1.4 Å resolution X-ray diffraction (XRD) on crystals.

The second example is that of murine neuroglobin.[25,26] This monomeric protein is arranged in the orthorhombic I222 space group. The unit cell contains 18 protein monomers, and the corresponding heme groups are shown in Figure 2 right frame, in the case of the carbonmonoxy-derivative (PDB code 1W92). The molecules of the prosthetic group are still oriented approximately parallel or antiparallel to each other, and the heme normals are very close to the **c**-axis: $a_{\beta eq} = 0.95$ along this direction. By rotating the crystal around the **a**-axis or the **b**-axis it corresponds to a variation of a_β between 0.024 and 0.95, so that the extraction of the pure I_{normal} component is more favorable than in the $P2_1$ crystal of myoglobin, in a beamline equipped for orienting the crystal along a specific crystal axis.

The feasibility of a structural study combining polarized XAS and XRD studies on the same protein crystals has already been demonstrated.[27] Polarized XANES on single crystals have been proved to be a valuable tool to elucidate at atomic resolution the local structure of the metal site under investigation.[15,28] Polarized spectra can directly provide the axial ligand coordination by suppressing the I_{heme} contribution, whose major intensity is predominant in solution.[4,20] Working at a MAD beamline equipped for this specific purpose, namely, beamline 10.1 at SRS (Daresbury, UK),[29] it has been possible to determine both the 1.4 Å X-ray structure of the ferric cyanomet derivative of sperm whale Mb (MbCN) and, by XANES, the local structure around the Fe ion with enhanced resolution,[15] comparable to that of atomic resolution XRD.

Applications of the XANES spectroscopy to single crystals of sperm whale Mb derivatives, and NgbCO, are reported and compared with results of XRD determinations. In the case of NgbCO, the parallel determination by XAS in solution is also reported. The potentials and limitations of XANES spectroscopy and the MXAN method on the subject of pursuing a XRD/XAS joint analysis are discussed.

Appendix

TABLE 1: XANES Structural Determinations from Single Crystals[a]

sample	data analysis technique	Fe−Np (Å)	Fe−His (Å)	Fe−XY (Å)	tilting (deg)	bend (deg)	X−Y (Å)
MbCN	XANES (SCF-fixed)	2.01(2)	2.07(2)	1.87(2)	-	10(7)	1.10(2)
	XANES (optim)	1.98(3)	2.13(3)	1.92(*3*)	4(4)	4(3)	1.21(1)
	average	1.99(2)	2.10(2)	1.89(2)	-	7(4)	1.15(5)
	XRD 1.4 Å[15]	2.04	2.08	1.92	7	13	1.11
MbCO	XANES (SCF-fixed)	2.00(2)	2.06(3)	1.83(2)	-	14(4)	1.07
	XANES (optim)	1.97(2)	2.07(3)	1.90(2)	3	15	1.20(2)
	average	1.98(1)	2.06(2)	1.86(*3*)		16(2)	1.13(7)
	XRD 1.1 Å[38]	1.98	2.06	1.73	4	7	1.12
		1.98	2.06	1.82	9	9	1.09
	XRD 1.1 Å[37]	2.02	2.08	1.90−1.84	4; 5	13; 15	1.15; 1.17
	XRD 1.21 Å[41,b]						
MbNO	XANES (SCF-fixed)	2.02(2)	2.11(2)	1.92(2)	-	88(3)	1.10(3)
	XANES (optim)	2.00(2)	2.16(2)	1.94(2)	-	36(5)	1.17(4)
	average	2.01(3)	2.13(3)	1.93(2)	-	61(27)	1.13(4)
	XRD 1.7 Å[42]	2.08	2.18	1.89	-	68	1.15
	XRD 1.3 Å[43]	2.05	2.08	1.87	-	36	1.20
Mb•CO	XANES (SCF-fixed)	2.03(2)	2.05(2)	3.08(7)[c]	37(7)	31(5)	1.24
	XANES (optim)	2.00(2)	2.00(2)	3.23(4)	19(7)	37(17)	1.13
	average	2.01(1)	2.02(*3*)	3.15(8)	28(9)	35(5)	1.18(6)
	XRD 1.7 Å[49]	2.00	2.11	2.84	23	45	1.21
	XRD 1.5 Å[50]	1.97	2.25	3.60	27	54	1.12
deoxy-Mb	XANES (SCF-fixed)	2.05(3)	2.16(2)	3.5(1)[c]			
	XANES (optim)	2.04(6)	2.06(3)	3.2(1)			
	average	2.04(3)	2.08(2)	3.3(2)			
	XRD 1.15 Å[37]	2.07	2.14	3.5			

[a] The d(Fe−Np) distance is derived from the I_{bonc} spectrum. All of the other parameters are derived from the I_{normal} spectrum. Numbers in parentheses represent the statistical error or the maximum semidispersion error (italic) on the last digit. In some cases the parameter of tilting and X−Y distance has been refined in the first optimization cycle and then kept constant before the last loop of minimization and error analysis. [b] Two conformers were found for the CO binding geometry. [c] In the Mb•CO adduct, the CO molecule is present in the first docking site, while a water molecule at about 3 Å is fitted for the deoxy-Mb species.

Materials and Methods

Protein Purification and Crystallization. The synthetic gene coding for murine Ngb (mutant C55S/C120S) was cloned in the pet14b vector and expressed as N-terminal His6-tagged protein in *Escherichia coli* strain BL21(DE3)pLysS. Protein expression and purification has been detailed elsewhere,[30] and for the aim of this paper we report only the details of the crystallization procedure. Crystals grew in a 1:1 mixture of protein (10 mg/mL) and reservoir solution (1.6 M ammonium sulfate, 0.1 M MES, pH 6.5, 10% v/v dioxane), at 20 °C in the hanging-drop method, and their size was about 100 × 100 × 150 μm. To prepare ferrous CO bound form, crystals were transferred into a suitable glass slide filled with mother liquor saturated with CO which contained 25% glycerol (as cryoprotectant) and 4 mM sodium dithionite. Reduced CO bound crystals were frozen in liquid nitrogen and stored in a dewar.

Data Collection. The polarized XANES spectra (in fluorescence mode) and the XRD data (at 1.7 Å resolution) of protein single crystals, collected at 100 K, have been measured at Daresbury, CCLRC 10.1 beamline[29] and at the European Synchrotron Radiation Facility in Grenoble, ESRF-BM30-B Fame beamline[31] at 15 K.

Details on crystal orientation and X-ray structure determination have been previously reported (MbCO by Della Longa et al.;[32] MbCN by Arcovito et al.;[15] NgbCO by Vallone et al.[25]). The same single crystals were used when acquiring XANES spectra at different orientations.

X-ray doses absorbed by the crystals depend on the experimental conditions which were very different at the Daresbury and ESRF facilities, the latter emitting a much higher X-ray flux. At ESRF, according to the measured flux (10^{11} photons/s at 7100 eV) and spot size (3×10^4 micron^2), the X-ray dose absorbed by our protein crystals is approximately 600 Gy/s, and a dose of 9 MGy is absorbed in 4 h, the time needed for a complete XRD + XANES experiment assuming to work with a fixed spot on the sample. The spot position actually changes during the experiment; however, this value is still below the maximum recommended dose to a protein crystal, that is 30 MGy.[33]

Cryoradiolytic effects at the level of the Fe-heme site are probed by XANES, which is highly sensitive to iron net charge and coordination symmetry. We have previously reported the water dissociation in ferric myoglobin[7] and CO dissociation in NgbCO at very low temperatures[30] as due to heavy X-ray irradiation. The experiments reported in the present paper have been done at the best experimental conditions with minimal X-ray effects, assuring a full integrity at the heme site level and reproducibility of the XANES spectra within the beam time available to users. Further detailed studies as a function of the X-ray dose deserve to be undertaken.

Data Analysis. XAS data have been analyzed by means of the MXAN software package[16] for the low energy range (XANES) and by GNXAS[34,35] for the solution spectrum of Ngb in the high energy range (EXAFS).

GNXAS is a well-established method for the EXAFS analysis of materials, liquids, and biological matter. In the XANES regime, two methods have been systematically applied within the MXAN package and compared for the calculation of the MT potential (namely, "SCF-fixed" and "optim.") showing the effect on the choice of potential parameters with respect to the final results. In fact, up to date, in spite of the occasional differences found in the final values of the structural parameters, we did not find relevant differences in the residual square function of the best fits, justifying a choice between them. Therefore, we have considered these procedures as two independent methods whose accuracy is affected by its own

TABLE 2: NgbCO Structural Determination[a]

experiment	Fe−Np (Å)	Fe−His (Å)	Fe−CO (Å)	tilt (deg)	bend (deg)	C−O (Å)
XRD 1.7 Å[25,b]	2.00(15)	2.11(18)	1.81(14)	-	22	1.03(15)
XANES (SCF-fixed)	2.05(7)	2.07(3)	1.85(3)	14(17)	10(10)	1.12(3)
XANES (optim)	1.97(2)	2.06(2)	1.86(2)	10(3)	19(5)	1.23(2)
average	2.01(3)	2.06(2)	1.85(2)	12(9)	15(6)	1.17(6)
EXAFS (solution)	1.99 (1)	2.10(4)	1.81(2)	-	7(7)	1.08 (2)
XANES (solution)	2.02(2)	1.96(7)	1.86(5)	-	8(8)	1.10

[a] Numbers in parentheses represent the statistical error of the last digits. [b] Estimated standard uncertainties are calculated by using DPI$_{Rfree}$.[51] The standard uncertainty on the Fe−C−O angle is not quoted as it has been refined automatically based on the restraint listed in the CCP4 library.

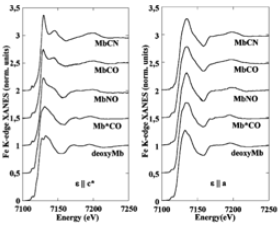

Figure 4. Polarized XANES spectra of different derivatives of Mb as indicated in the figure. Left frame: (*ε*∥**c***) polarization; right frame: (*ε*∥**a**) polarization. XANES fingerprints vary according to the type and binding geometry of axial ligands to the heme iron. I_{normal} and I_{heme} are obtained by linear combining the (*ε*∥**a**) and (*ε*∥**c***) polarized spectra of the $P2_1$ crystals as described in the Introduction.

systematic errors. Values of distances and angles in Tables 1 and 2 are averaged as a last step, and their respective error is obtained from uncertainty propagation theory. Both the "SCF-fixed" procedure[8,15] and the "optim." procedure[20] for the MT potential calculation have been described in our previous works.

The real part of the exchange term was calculated using the Hedin−Lundqvist energy-dependent potential,[36] while all of the inelastic losses were taken into account by convolution with a phenomenological broadening function $\Gamma = \Gamma_c + \Gamma(E)$. The constant part Γ_c includes contributions from the core-hole lifetime, while the energy-dependent term $\Gamma(E)$ represents the inelastic processes. The experimental resolution was taken into account by a Gaussian convolution (0.6−0.8 eV) of the theoretical spectrum. The method introduces two free parameters linked to the potential, and two parameters linked to $\Gamma(E)$, that are derived during the fit.[20]

The Fe-porphyrin macrocycle, and the ligand molecules, were included in the atomic cluster used for XANES analysis. The cluster size and the l_{max} value (i.e., the maximum l value of the spherical harmonic expansion of the scattering path operators) were chosen on the basis of a convergence criterion.

Results and Discussion

Polarized XANES of Hemeproteins. The polarized XANES values of hemeproteins strongly depend on the presence and the type of the sixth ligand coordination. Figure 4, left frame, clearly shows the changes of (*ε*∥**c***) polarized XANES spectra (mainly contributed by the I_{normal} component) displayed along various crystals of sperm whale Mb (CN, CO, NO, low temperature CO photoproduct, deoxy) having all $P2_1$ symmetry. Spectra are sensitive to the iron sixth ligand atom (e.g., CO vs NO) and even to the more distant atom of small molecules (e.g., CO vs CN); in a previous work[23] on hexacyanoferrat(II) and (III) in solution we showed that, contrary to EXAFS, the XANES signal can directly probe the chemical nature of the metal ligands, and not only their binding geometry.

Weaker modifications affect the (*ε*∥**a**) polarized spectra (I_{heme} component, right panel of Figure 4) as, in spite of their large number, heme-plane structural parameters are highly restrained due to the rigidity of the porphyrin ring. Indeed, this is the reason why even solution spectra are diagnostic of the axial coordination in hemeproteins, as in these systems the I_{heme} contribution can be considered a rather constant "background signal".

Whereas the XANES fingerprints probe the axial coordination, their fine structure provides the metrics via the full MS analysis. Figure 5 shows how the MXAN procedure (see Methods) can be applied to interpret the Fe K-edge XAS spectrum, extract the ligand binding geometry, and provide heme structural parameters. XANES features emerge as single scattering (SS) or MS contributions from a cluster of about 32 atoms around the Fe atom. It is possible to calculate the theoretical I_{normal} and I_{heme} spectra of MbCO as a function of the cluster size (panel A and B of Figure 5, respectively; here the "optim." procedure to build the MT potential is used). It is necessary to include all of the porphyrin macrocycle, the proximal histidine, and the sixth ligand to reproduce the experimental spectra of MbCO single crystal. As stated in the Materials and Methods Section, the comparison between theory and experiment is done after convoluting the theoretical spectra with an energy-dependent broadening function. In panel C and D the theoretical I_{normal} and I_{heme} spectra are still reported before convolution (dotted spectra) and after convolution (solid line). The resulting spectra fit the experimental ones of the MbCO crystal (circles), after optimization of the structural parameters of the atomic cluster. It is evident from inspection of the spectra in panel C and D, that all of the features from the rising edge up to about 200 eV above the edge are well reproduced by the one-electron MS theory using a MT potential (features 1−6 of the I_{normal} spectrum and features 1−7 of the I_{heme} spectrum). In particular, we note that peaks 1−3 of the I_{normal} spectrum emerge beyond the first shell calculation as MS features of the axial pathways including the second and third shell and are strongly sensitive to the ligand binding geometry, whereas features 2 and 3 of the I_{heme} spectrum emerge as 3-shell contributions and are sensitive to the overall structure and distortions of the porphyrin macrocycle.

In Figure 6 the MXAN fits (solid lines) carried out on the I_{normal} spectra of MbCN, MbCO, MbNO, Mb·CO, and deoxy-Mb (circles) are displayed. The one-electron MS analysis, in

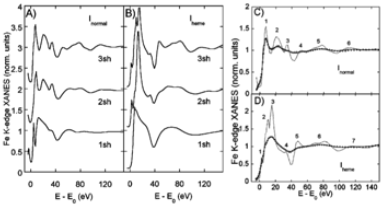

Figure 5. (A and B) XANES calculation (without broadening factors) of the I_{normal} and I_{heme} components of MbCO as a function of the cluster size. A final size of 32 atoms including the whole porphyrin ring, the CO molecule, and the proximal histidine residue are necessary to reproduce the experimental spectra. (C and D) MXAN fits (solid line: with broadening; dotted line: without broadening) of the experimentally determined I_{normal} and I_{heme} components (circles).

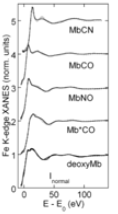

Figure 6. MXAN fits (solid line) of the I_{normal} component (dots) of the Mb derivatives of Figure 4. The MXAN fits shown here have been performed by using the "optim" method. The "SCF-fixed" method produces very similar results, undistinguishable by visual inspection.

the frame of the MT approximation, provides a good simulation of both hexa-coordinate and five-coordinate derivatives of myoglobin. The structural results obtained by the fitting procedure applied to I_{normal} (for the axial parameters) and I_{heme} (for the Fe−N_p distance) are summarized in Table 1 and compared with structural parameters from XRD. Both of the results obtained by using the "SCF-fixed" and the "optim" methods to calculate the potential are reported.

As far as it concerns the first shell distances, the two methods ("optim" and "SCF-fixed") provide values in very good agreement with each other (the maximum discrepancy being 0.03 Å out of errors). Relative to the XRD determinations, our results are consistent with high (1.1 Å) resolution crystal structures, that is, MbCO and deoxyMb. In the case of MbCO, as previously reported,[8] our data support the results by Vojtechovsky et al.[37] rather then those by Kachalova et al.[38] This last determination is more consistent with heme model systems[39] and related DFT calculations,[40] including a ∼0.1 Å decrease of the Fe−C distance; however, a recent XRD study on MbCO at 1.21 Å resolution (PDB code 3E4N)[41] still confirms the structure with a longer Fe−C distance (in both of the two conformers found), in agreement with our data. In the other cases, the XRD resolution is lower as well as the accuracy on these parameters, and the XAS values become important restraining factors to enhance resolution at the metal site, as we demonstrated for MbCN.[15]

The determination of the bending angle of the ligands, CO, CN, and NO, depends on weaker signals associated to second and third shell MS pathways and is very accurate in the case of MbCO and MbCN but becomes less accurate in the case of MbNO; actually, the higher the intensity and phasing ("focusing effect") of the signals related to the Fe−X−Y geometry, the higher the accuracy is in its determination by XAS.

In spite of their relatively small statistical errors, discrepant values of the C−O and C−N distances (0.1 Å out of errors), and of the Fe−N−O bending angle (40° out of errors), occur by using the two different methods to calculate the MT potential. This fact highlights the existence of systematic errors related to the MT potential calculation that cannot be neglected. As explained in the Material and Methods Section, we have reported in Table 1 results from the two procedures as independent measuring methods whose accuracy is affected by its own systematic errors; therefore, the average of the two determinations (distances and angles) is displayed in the same table, its error being obtained from uncertainty propagation theory. Following this assumption, the agreement between XAS and high resolution XRD is extended to all of the structural parameters of the metal site, including the bond length of the bound diatomic molecules. Moreover, a more reliable evaluation of parameters like the bending angle in MbNO (61 ± 27)° is obtained using the maximum semidispersion error, for X-ray structures known at lower resolution. Our results on MbNO confirm the XRD determination reported in literature[42,43] that are known to be in contrast with solution EXAFS measurements.[44] However, many environmental parameters (preparative method, pH, temperature) have been suggested to affect the chemical and structural state of this derivative at the level of the iron site[41] and can be responsible of this discrepancy. This topic is currently part of our work-in-progress activity and will be specifically addressed, using the protocol described in Scheme 1, in future studies.

In Figure 7 the XRD map (lower frame) and the Fe K-edge XAS analysis (upper frame) of murine NgbCO are displayed. According to Scheme 1, the XAS measurements have been carried out on both the *R*32 single crystal opportunely oriented

Appendix

SCHEME 1: Proposed Method To Determine Metal Site Structure in Proteins[a]

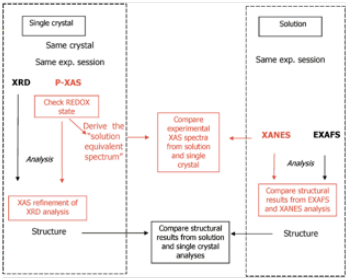

[a] Experimental design of a combined XRD-XAS measurement. XANES can improve the reliability of both XRD (single crystal) and EXAFS (solution) analyses, providing a validation of the results and a cross-check for the comparison of the two techniques when both data are available on a given metal site.

and in solution. As mentioned in the Methods Section, the *R*32 crystal of NgbCO shows a very strong XAS angular dichroism, making easy to extract the I_{heme} and I_{normal} components from the experimental XANES spectra collected at various angles. The two components are depicted in panels A and B of Figure 7, upper frame (panel A is a blow-up of the pre-edge region). The 2:1 weighted average of the two components and the solution XANES spectrum are also displayed for visual comparison. The comparison was required since at room temperature crystals of reduced Ngb tend to crack following CO soaking, and the X-ray structure of NgbCO (PDB code 1W92), obtained by flash freezing the soaked crystal, was found to undergo a substantial conformational change compared to the one of the ferric form (PDB code 1Q1F), involving a sliding motion of the heme falling into the proximal cavity. Thus, since cracking upon CO binding at room temperature suggests a further relaxation, a crystal packing constraint at the Fe-heme site level could not be excluded. Independently from the systematic errors linked to the XAS analysis, the high similarity between the two experimental XANES spectra (crystal and solution) gives the best direct evidence that the crystal preparation protocol does not induce relevant costraints at least at the level of the Fe-heme structure of NgbCO.

In Figure 7, upper frame panels C and D, the I_{heme} and I_{normal} XANES spectra collected onto the *R*32 crystal of NgbCO are reported (open circles), together with the best fitting spectra (solid line) found using the MXAN package. Finally, in panel E, the Fourier transform of the EXAFS solution spectrum of NgbCO (dots) and the best fit obtained via the GNXAS package (solid line) are reported. The XAS analysis in solution (both EXAFS and XANES) has been previously carried out,[20] and the EXAFS analysis is shown in the figure only to completely address the protocol reported in Scheme 1. The relevant structural parameters obtained by the combination of all of these measurements are displayed in Table 2 and compared with results from 1.7 Å resolution XRD. As well as for myoglobin, only the Fe−N_δ distance is obtained from the analysis of I_{heme}, whereas the axial parameters are derived from I_{normal}. As the experimental I_{heme} spectrum of NgbCO is available only up to 120 eV beyond the edge, the MXAN analysis of this spectrum is carried out on a shorter energy range as compared to all of the other experimental spectra, that are analyzed up to about 200 eV beyond the edge. As a consequence, a lower accuracy on the Fe−N_δ distance is obtained: 2.05(7) Å by using the "SCF-fixed" method, and 1.97(2) Å by using the "optim" one. The average of the results from the two methods gives a better agreement with the independent determinations by XRD and EXAFS in solutio; however, the importance of choosing a large energy interval for the XANES analysis via the MXAN package is confirmed.

The numerical results obtained from the MXAN analysis for the axial parameters of NgbCO and MbCO are almost identical, due to the similarity between the two experimental I_{normal} spectra (see Figures 6 and 7c). Residual differences are observable (e.g., the intensity of the main peak of the I_{normal} component is enhanced in NgbCO with respect to MbCO); however, they are accounted for by MXAN package using different broadening parameters within a very similar structure. As explained above, the broadening function used here is phenomenological and cannot give reliable clues on the physical origin of such spectral changes. Electronic damping and conformational disorder can affect the low photoelectron energies,[45] but none of them is treated here quantitatively. Theoretical improvements of the imaginary part of the complex potential used,[45] and molecular dynamics[20] should be implemented in the MXAN code to give a more exhaustive approach to this problem.

Last, it is worth noting that, given an exact orientation of the crystal and the crystallographic structure, the XANES spectrum can be calculated independently from C4 symmetry approximation. For this purpose, the a_δ and b_δ values from eq 3 are not used, and the calculation has to be repeated for any asymmetric unit and finally averaged. This analysis becomes heavily time-consuming; for instance, in the fitting procedure of NgbCO,

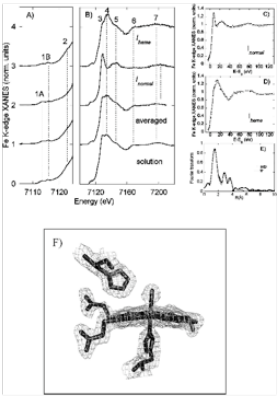

Figure 7. Panels A and B: pre-edge and Fe K-edge XANES spectra of murine NgbCO. From top to bottom: I_{heme} and I_{normal}; their weighted average giving the "solution equivalent" spectrum and the experimental solution XANES spectrum. Eight labeled features (1A, 1B, 2−7) are discernible in all spectra. Panels C and D: MXAN best fits (solid lines) of I_{normal} and I_{heme} (open circles). Panel E: Fourier transform of the EXAFS spectrum in solution (dots) and best fit obtained by the GNXAS procedure (solid line). Panel F: blow-up of the electron density map of the active site of NgbCO, including the proximal (H96) and distal (H64) histidines; the density is contoured at 1σ.

the spectrum has to be calculated 18 times at each optimization step, and the overall fitting procedure becomes 18 times longer.

To assess the adequacy of the C4 approximation, the extraction of the absorption tensor described in eq 1 from the experimental data is required. This procedure has been performed on a $P2_1$ Mb sample (data not shown). For this space group, the absorption tensor contains four independent elements, σ_x, σ_y, σ_z, and σ_{xz} which are functions of X-ray energy at the Fe K edge. Under the C4 symmetry, $\sigma_x = \sigma_y$ and $\sigma_{xz} = 0$. According to the extracted values of the tensor, both $(\sigma_x - \sigma_y)$ and σ_{xz} functions are negligible, that is, their related signal is within 1% of the absorption jump, with only a 3% bump at 7120 eV.

Ngb Analysis. In the case of Ngb the combination of XANES and XRD gives new insights of the functional transition of the protein upon ligand binding. According to MD simulations, the heme sliding distributions along its first essential eigenvector in the crystal and in solution[66,67] are different at room temperature for NgbCO. In solution, the conformational distribution is peaked around a position close to the crystallographic structure of deoxy-Ngb (i.e., with no heme sliding and a major steric hindrance between CO and distal histidine). In the crystal the MD simulation at room temperature shows a double-peaked distribution. A first, higher maximum is around a position close to the crystallographic structure of NgbCO, with sliding of the heme and no steric hindrance between the CO molecule and the distal histidine. A second, lower one, is located near that of deoxy-Ngb. However, in the cryo-trapped crystal, only the first conformation is observed by XRD as significantly populated. Accordingly, in our XAS experiments in solution, at cryogenic temperature, the entire conformational ensemble, centered around the deoxy-like one (with no heme sliding), should be probed. Conversely in the crystal, only the more populated conformation, visualized by XRD (with sliding of the heme) should contribute to the measured XAS spectra. In spite of the large rearrangement of the protein environment and of the heme location predicted by MD, the local structure around the Fe ion in NgbCO determined by XAS seems unaltered between the crystal and the solution sample. As a consequence, no residual energy should be stored here as due to crystal packing, to be delivered with cracking at room temperature. This result reinforces the model proposed to explain the functional transition of the protein when an exogenous ligand replaces the distal histidine in the sixth position. The residual energy involved in the protein relaxation responsible of cracking the crystal does not reside in the heme pocket but is rapidly transferred at peripheral sites of the protein (more likely the CD corner) so that the final tertiary rearrangement of the protein in solution can be reached.

Instrumentation Development. The presence of beamlines at synchrotron facilities, where the combination of experiments in crystal and solution using XAS and XRD is available, could be a valuable tool to deeply investigate a large class of proteins such as those containing metal centers. As stated above, the structural resolution obtained by XANES data in solution is comparable with 1.4 Å resolved X-ray data and converges in single crystals to a higher resolution level[15] as a function of the relative orientation of the symmetry-related molecules. A diagram showing the rationale of applying XAS to both single crystal and solution samples of metalloproteins is sketched (Scheme 1). The potential advances in knowledge derived from such an approach are depicted in red: XAS of polarized spectra can be used to probe the redox state and to refine the active site structure determined by XRD.[15,28] Similarly, the XANES and EXAFS analyses can be jointly performed in solution and their results compared to each other.[20,30] Lastly and more importantly, the "solution equivalent spectrum" can be obtained by a weighted sum of polarized spectra of the crystal, so that the single crystal and solution states can be directly compared to test if the crystallization procedure has selected a particular protein substate.[7] In this framework, hemeproteins constitute a special case giving a further advantage: in fact, for these proteins the X-ray structure can be collected together with angular-dependent XAS spectra in the same crystal; moreover, XAS spectra in solution can be also acquired, and a direct and precise comparison with the crystal state is possible.

Conclusions

The possibility to derive the widest possible number of information from the same sample is always an aim for any experimentalist. This fact is even more evident when the sample is a protein crystal. In this case the bottleneck of the structural investigation is often the crystallization production.[68] Moreover, these crystals are often poorly or anisotropically diffracting, leading to low resolution data. Thus, it is mandatory to obtain as much as possible from each protein crystal. Therefore, combining experimental data using XRD and XANES on protein

Appendix

crystal allows us to obtain the local structure around the metal center with an increased resolution, which can provide the structural determinants associated with the affinity of an exogenous ligand such as the small diatomic gaseous molecules CO, CN, and NO. Moreover, XANES spectra can be also acquired in solution; thus, any crystal constrain onto the local structure around the metal can be tested. Finally, the intrinsic dichroism of the heme, when irradiated by the polarized synchrotron X-rays, is a property that allows increasing the structural resolution obtained applying the MXAN package to polarized XANES spectra from the crystal, with respect to the same analysis onto the solution spectrum of the protein.

Acknowledgment. Thanks are due to the European Synchrotron Radiation Facility and to STFC Daresbury Laboratory for provision of synchrotron radiation facilities and to CASPUR, with the standard HPC grant 2009 entitled "A Combined X-ray Absorption Spectroscopy, Molecular Dynamics Simulation and Quantum Mechanics Calculation procedure for the structural characterization of ill-defined systems". A.A. is grateful for the financial support by the Italian Ministry of University and Research (MiUR) [Linea D1 "ex-60%" 2007-2008, "Emoproteine di interesse Biomedico", Università Cattolica Sacro Cuore], and B.V. is grateful for the financial support by MiUR of Italy grants FIRB RBLA03B3KC_004 and PRIN 20074TJ3ZB_005. M.C. is especially grateful to European Molecular Biology Laboratory (EMBL) for the financial support.

References and Notes

(1) Weigelt, J. *Exp. Cell. Res.* **2010**, *316*, 1332–1338.
(2) Cook, J. D.; Penner-Hahn, J. E.; Stemmler, T. L. *Methods Cell Biol.* **2008**, *90*, 199–216.
(3) Strange, R. W.; Feiters, M. C. *Curr. Opin. Struct. Biol.* **2008**, *18*, 609–16.
(4) Arcovito, A.; Bonamore, A.; Hazemann, J. L.; Boffi, A.; D'Angelo, P. *Biophys. Chem.* **2009**, *147*, 1–7.
(5) Arcovito, A.; Lamb, D. C.; Nienhaus, G. U.; Hazemann, J. L.; Benfatto, M.; Della Longa, S. *Biophys. J.* **2005**, *88*, 2954–64.
(6) D'Angelo, P.; Lucarelli, D.; della Longa, S.; Benfatto, M.; Hazemann, J. L.; Feis, A.; Smulevich, G.; Ilari, A.; Bonamore, A.; Boffi, A. *Biophys. J.* **2004**, *86*, 3882–92.
(7) Della Longa, S.; Arcovito, A.; Benfatto, M.; Congiu-Castellano, A.; Girasole, M.; Hazemann, J. L.; Lo Bosco, A. *Biophys. J.* **2003**, *85*, 549–58.
(8) Della Longa, S.; Arcovito, A.; Girasole, M.; Hazemann, J. L.; Benfatto, M. *Phys. Rev. Lett.* **2001**, *87*, 155501.
(9) Green, M. T.; Dawson, J. H.; Gray, H. B. *Science* **2004**, *304*, 1653–6.
(10) Brunori, M. *Protein Sci.* **2009**, *19*, 195–201.
(11) Burmester, T.; Weich, B.; Reinhardt, S.; Hankeln, T. *Nature* **2000**, *407*, 520–3.
(12) Sun, Y.; Jin, K.; Mao, X. O.; Zhu, Y.; Greenberg, D. A. *Proc. Natl. Acad. Sci. U.S.A.* **2001**, *98*, 15306–11.
(13) Yano, J.; Yachandra, V. K. *Photosynth. Res.* **2009**, *102*, 241−254.
(14) Bricogne, G.; Capelli, S. C.; Evans, G.; Mitschler, A.; Pattison, P.; Roversi, P.; Schiltz, M. *J. Appl. Crystallogr.* **2004**, *38*, 168–72.
(15) Arcovito, A.; Benfatto, M.; Cianci, M.; Hasnain, S. S.; Nienhaus, K.; Nienhaus, G. U.; Savino, C.; Strange, R. W.; Vallone, B.; Della Longa, S. *Proc. Natl. Acad. Sci. U.S.A.* **2007**, *104*, 6211–6.
(16) Benfatto, M.; Della Longa, S. *J. Synchrotron Radiat.* **2001**, *8*, 1087–94.
(17) Cabaret, D.; Joly, Y.; Renevier, H.; Natoli, C. R. *J. Synchrotron Radiat.* **1999**, *6*, 258–60.
(18) Joly, Y. *Phys. Rev. B* **2001**, *63*, 125120–9.
(19) Ankudinov, A. L.; Ravel, B.; Rehr, J. J.; Conradson, S. D. *Phys. Rev. B* **1998**, *58*, 7565–76.
(20) D'Angelo, P.; Lapi, A.; Migliorati, V.; Arcovito, A.; Benfatto, M.; Roscioni, O. M.; Meyer-Klaucke, W.; Della-Longa, S. *Inorg. Chem.* **2008**, *47*, 9905–18.
(21) Benfatto, M.; D'Angelo, P.; Della Longa, S.; Pavel, N. V. *Phys. Rev. B* **2002**, *65* (174205), 1–5.
(22) D'Angelo, P.; Benfatto, M.; Della Longa, S.; Pavel, N. V. *Phys. Rev. B* **2002**, *66* (064209), 1–7.
(23) Hayakawa, K.; Hatada, K.; D'Angelo, P.; Della Longa, S.; Natoli, C. R.; Benfatto, M. *J. Am. Chem. Soc.* **2004**, *126*, 15618–23.
(24) Giorgetti, M.; Della Longa, S.; Benfatto, M. *J. Phys.: Conf. Ser.* **2009**, *190*, 012145−1/6.
(25) Vallone, B.; Nienhaus, K.; Matthes, A.; Brunori, M.; Nienhaus, G. U. *Proc. Natl. Acad. Sci. U.S.A.* **2004**, *101*, 17351–6.
(26) Vallone, B.; Nienhaus, K.; Brunori, M.; Nienhaus, G. U. *Proteins* **2004**, *56*, 85–92.
(27) Strange, R. W.; Hasnain, S. S. Combined Use of XAFS and Crystallography for Studying Protein-Ligand Interactions in Metalloproteins. In *Protein-Ligand Interactions: Methods and Applications*; Nienhaus, G. U., Ed.; Humana Press Inc.: Totowa, NJ, 2005; Vol. 305, pp 167−96.
(28) Yano, J.; Kern, J.; Sauer, K.; Latimer, M. J.; Pushkar, Y.; Biesiadka, J.; Loll, B.; Saenger, W.; Messinger, J.; Zouni, A.; Yachandra, V. K. *Science* **2006**, *314*, 821–5.
(29) Cianci, M.; Antonyuk, S.; Bliss, N.; Bailey, M. W.; Buffey, S. G.; Cheung, K. C.; Clarke, J. A.; Derbyshire, G. E.; Ellis, M. J.; Enderby, M. J.; Grant, A. F.; Holbourn, M. P.; Laundy, D.; Nave, C.; Ryder, R.; Stephenson, P.; Helliwell, J. R.; Hasnain, S. S. *J. Synchrotron Radiat.* **2005**, *12*, 455–66.
(30) Arcovito, A.; Moschetti, T.; D'Angelo, P.; Mancini, G.; Vallone, B.; Brunori, M.; Della Longa, S. *Arch. Biochem. Biophys.* **2008**, *475*, 7–13.
(31) Proux, O.; Biquard, X.; Lahera, E.; Menthonnex, J. J.; Prat, A.; Ulrich, O.; Soldo, Y.; Trévisson, P.; Kapoujyan, G.; Perroux, G.; Taunier, P.; Grand, D.; Jeantet, P.; Deleglise, M.; Roux, J. P.; Hazemann, J. L. *Phys. Scr.* **2005**, *115*, 970–3.
(32) Della Longa, S.; Arcovito, A.; Vallone, B.; Castellano, A. C.; Kahn, R.; Vicat, J.; Soldo, Y.; Hazemann, J. L. *J. Synchrotron Radiat.* **1999**, *6*, 1138–47.
(33) Owen, R. L.; Rudino-Pinera, E.; Garman, E. F. *Proc. Natl. Acad. Sci. U.S.A.* **2006**, *103*, 4912–7.
(34) Filipponi, A.; Di Cicco, A. *Phys. Rev. B: Condens. Matter* **1995**, *52*, 15135–49.
(35) Filipponi, A.; Di Cicco, A.; Natoli, C. R. *Phys. Rev. B: Condens. Matter* **1995**, *52*, 15122–34.
(36) Hedin, L.; Lundqvist, B. I. *J. Phys. C* **1971**, *4*, 2064–75.
(37) Vojtechovsky, J.; Chu, K.; Berendzen, J.; Sweet, R. M.; Schlichting, I. *Biophys. J.* **1999**, *77*, 2153–74.
(38) Kachalova, G. S.; Popov, A. N.; Bartunik, H. D. *Science* **1999**, *284*, 473–6.
(39) Kim, K.; Fettinger, J.; Sessler, J. L.; Cyr, M.; Hugdahl, J.; Collman, J. P.; Ibers, J. A. *J. Am. Chem. Soc.* **1989**, *111*, 403–5.
(40) Rovira, C.; Kunc, K.; Hutter, J.; Ballone, P.; Parrinello, M. *J. Phys. Chem. A* **1997**, *101*, 8914–25.
(41) Tomita, A.; Sato, T.; Ichiyanagi, K.; Nozawa, S.; Ichikawa, H.; Chollet, M.; Kawai, F.; Park, S. Y.; Tsuduki, T.; Yamato, T.; Koshihara, S. Y.; Adachi, S. *Proc. Natl. Acad. Sci. U.S.A.* **2009**, *106*, 2612–6.
(42) Brucker, E. A.; Olson, J. S.; Ikeda-Saito, M.; Phillips, G. N., Jr. *Proteins* **1998**, *30*, 352–6.
(43) Copeland, D. M.; Soares, A. S.; West, A. H.; Richter-Addo, G. B. *J. Inorg. Biochem.* **2006**, *100*, 1413–25.
(44) Rich, A. M.; Ellis, P. J.; Tennant, L.; Wright, P. E.; Armstrong, R. S.; Lay, P. A. *Biochemistry* **1999**, *38*, 16491–9.
(45) Natoli, C. R.; Benfatto, M.; Della Longa, S.; Hatada, K. *J. Synchrotron Radiat.* **2003**, *10*, 26–42.
(46) Anselmi, M.; Brunori, M.; Vallone, B.; Di Nola, A. *Biophys. J.* **2007**, *93*, 434–41.
(47) Anselmi, M.; Brunori, M.; Vallone, B.; Di Nola, A. *Biophys. J.* **2008**, *95*, 4157–62.
(48) Chayen, N. E.; Saridakis, E. *Nat. Methods* **2008**, *5*, 147–53.
(49) Schlichting, I.; Berendzen, J.; Phillips, G. N. J.; Sweet, R. M. *Nature* **1994**, *371*, 808–12.
(50) Teng, T. Y.; Srajer, V.; Moffat, K. *Nat. Struct. Biol.* **1994**, *1*, 701–5.
(51) Cruickshank, D. W. J. *Acta Crystallogr. D* **1999**, *55*, 583–601.

JP104395G